Study on Synthesis of Metal Oxide/Hydroxide-Conductive Polymer Hybrid Film and Its Electrochemical Properties

金属酸化物/水酸化物-導電性高分子複合膜の作製とその電気化学特性に関する研究

山梨大学大学院
医工農学総合教育部
博士課程学位論文

September 2019
YANG Guoshen
（杨国深）

CONTENTS

List of Figures and Tables

Chapter 1 Introduction

1.1 General Introduction

With the rapid development of the global economy, the depletion of fossil fuels, and increasing environmental pollution, there is an urgent need for efficient, clean, and sustainable sources of energy. However, the overall share of renewable energy in total final energy consumption has increased only modestly in recent years, despite tremendous growth in some renewable sectors, as shown in Figure 1.1. To further increase the utilization of renewable energy, one of the most urgent need is the development of high-performance energy storage devices.

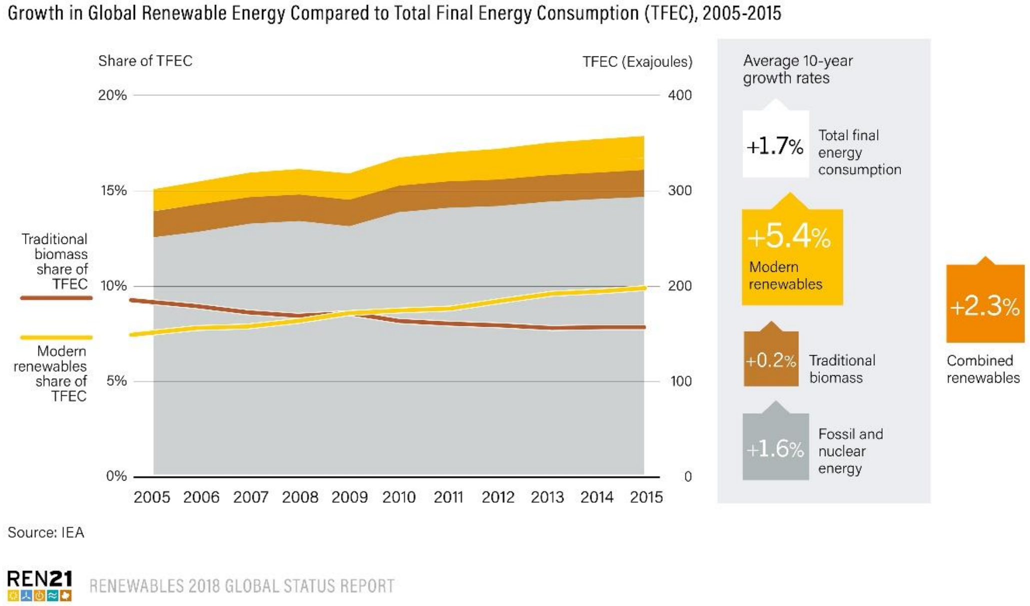

Figure 1.1. Growth in global renewable energy compared to total final energy consumption, 2005-2015. Reproduced with permission (Source: REN21) [1].

At the present stage, some of the most effective and practical technologies for electrochemical energy conversion and storage are capacitors, supercapacitors, batteries, and fuel cells. Figure 1.2 shows the energy and power densities of different electrical energy storage devices in the Ragone plot. In recent years, supercapacitors, as an energy storage device, have attracted significant attention due to their high power density, fast charge-discharge capability, long cycle life, and bridging function for the power/energy gap between batteries/fuel cells with high energy storage and traditional dielectric capacitors with high power output [2-4]. The unique electrochemical performances of supercapacitors have a wide range of applications.

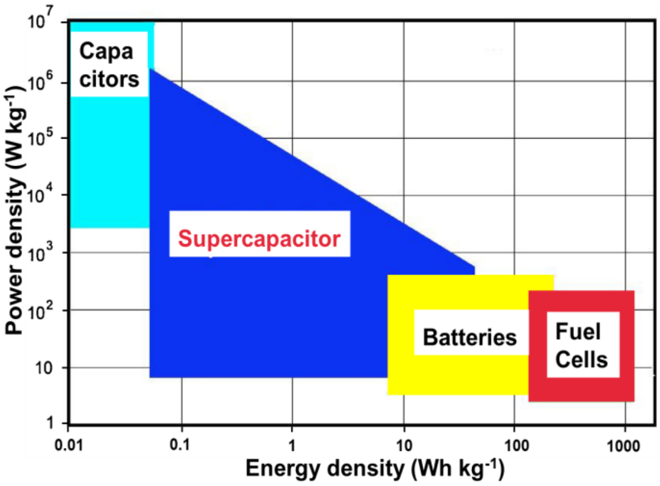

Figure 1.2. Ragone plot of power density and energy density of various energy storage devices [5].

1.2 Energy Storage Mechanisms for Supercapacitors

Based on their energy storage mechanisms, supercapacitors can be classified into electrical double layer capacitors (EDLCs) and pseudocapacitors (or faradaic capacitors), and their charge storage is based on the surface reactions of electrode materials, without ion diffusion within the bulk of the materials [6-7]. EDLCs physically store charges in the double layer that forms at the electrode-electrolyte interface via reversible ion adsorption. Pseudocapacitors chemically store their charges via redox reaction at the surface or near-surface of electrode materials [8]. These two mechanisms can function simultaneously depending on the nature of the electrode materials. Generally, electrode materials for EDLCs are composed of carbon-based materials, while that for pseudocapacitors are transition metal oxides and conducting polymers.

1.2.1 Electrical Double Layer Capacitors

One is the EDLCs, where the capacitance comes from the pure physical charge accumulated at the electrode-electrolyte interface, and there are no redox reactions on the electrode material during the charging/discharging processes. The electrical charge is only physically stored in the double layer, naturally formed at the electrode-electrolyte interface under voltage, as shown in Figure 1.3a [9]. During charging, the electrons travel through an external load from the negative electrode to the positive electrode. At the same time, anions move towards the positive electrode in the electrolyte while cations move towards the negative electrode. During discharge, the reverse processes take place. During charge and discharge process, there are no chemical reactions happen and active material transformations. This implies that the EDLCs devices are highly reversible and have a longer cycle life. Compare with conventional capacitors, the EDLCs have a significant increase in capacitance and internal resistance due to the use of the double layer charge storage at both electrodes. And their electrode materials usually using high-surface-area materials such as activated carbons, with a much higher surface area (in the order of hundreds of m^2/g) and much smaller thickness of double layers (in the range of 10^{-10} m) [10].

1.2.2 Pseudocapacitors

The other type is the pseudocapacitors or faradaic supercapacitors, in which fast and reversible faradic processes take place due to the electrode materials are electrochemically active. Pseudocapacitors are different from EDLCs. For pseudocapacitors, rapid and reversible redox reactions take place on the electrode materials through an external load and involve the passage of charge across the double layer, resulting in faradaic current passing through the supercapacitor device, as shown in Figure 1.3b. In fact, only part of the charge storage is assured by the double layer between electrode and electrolyte, while a greater amount of charge transfer and storage is due to faradic mechanisms (electrosorption, redox reactions, and intercalation). Since the electrochemical processes occur both on the surface and in the bulk near the surface of the solid electrode, pseudocapacitors exhibit far larger capacitance values and energy density than EDLCs [4]. However, pseudocapacitors usually suffers from relatively lower power density than EDLCs because faradaic processes are generally slower than non-faradaic processes [11]. Moreover, because redox reactions occur at the electrode surface, pseudocapacitors often lack stability during long-term cycling, similar to batteries.

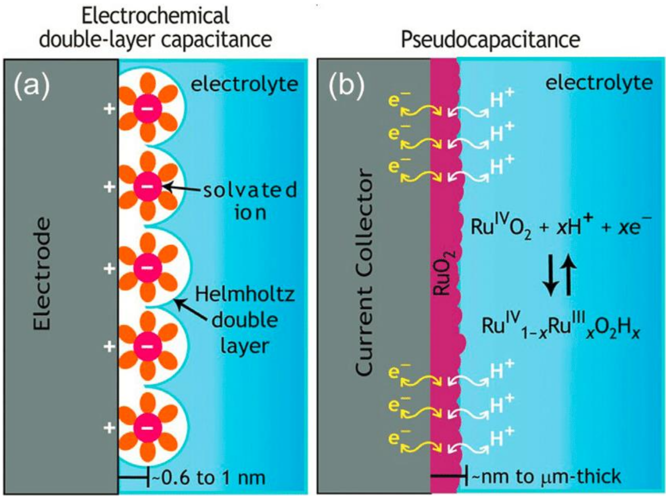

Figure 1.3. Schematic of two different charge storage mechanisms (a) electrochemical double layer capacitance and (b) pseudocapacitance. Reproduced with permission [9].

1.3 Electrode Materials for Supercapacitors

As mention above, supercapacitors are promising alternative or complement to batteries/fuel cells with high energy storage and traditional dielectric capacitors with high power output. However, due to the charge storage to the surface (or near the surface) of electrode materials, the energy density of supercapacitors is much lower than that of batteries. The main challenge for supercapacitors is to develop them with a high energy density that is close to that of current rechargeable batteries, while maintaining their inherent characteristics of high power and long cycling life. As a result, many efforts have been made to enhance their energy density. It is well known that the electrode material is the most critical part of the supercapacitor, and it is also a key factor in determining its performance. To overcome the obstacle of low energy density, one of the most intensive approaches is the development of new materials for supercapacitor electrodes [12].

In general, the electrode materials of supercapacitors can be categorized into three types [13-14]: carbon-based materials, transition metal oxides/hydroxides, conducting polymers.

1.3.1 Carbon-based materials

Carbon materials are considered the most widely used electrode materials due to their desirable physical and chemical properties. These properties include lower cost, non-toxicity, easy processing, higher specific surface area, high chemical stability, good electronic conductivity, and wide operating temperature range [15]. Typically, carbon materials store charges mainly in an electrochemical double layer formed at the interface between the electrode and the electrolyte, rather than storing them in the bulk of the capacitive material. Accordingly, the capacitance predominantly depends on the surface area of the electrode materials that is accessible to the electrolyte ions. Many factors are influencing the electrochemical performance of carbon-based materials, such as specific surface area, pore-size distribution, pore shape and structure, surface functionality, and electrical conductivity. Among these, proper control over the specific surface area and the pore size adapted to an appropriate type of electrolyte solution are significant to obtain high performance of carbon-based electrode materials.

1.3.1.1 Activated carbons (AC)

In the carbon-based materials, activated carbons are the most widely used electrode materials due to their relatively good electrical properties, large surface area, and moderate cost. Activated carbons are generally produced from physical (thermal) and/or chemical activation of various types of carbonaceous materials (e.g., wood, coal, nutshell, etc.). It is well known that the porous structure of activated carbons obtained through activation processes has a wide range of pore size distribution consisting of micropores (< 2 nm), mesopores (2-50 nm) and macropores (>50 nm) [16]. Several researchers have pointed out the discrepancy between the capacitance of the activated carbons and their specific surface area [6, 17]. This is because the specific capacitance is not only determined by the specific surface area. Some other parameters such as pore size distribution, electrical conductivity, pore shape and structure, and surface functionality can also influence their electrochemical performance to a great extent. In addition, excessive activation will lead to large pore volume, which results in the drawbacks of low material density and conductivity. These would in turn cause a low volumetric energy density and loss of power capability [18].

Besides the porous structure of activated carbons, the surface functionalities also play essential roles on the activated carbon electrode properties, due to they can affect the wettability of the carbon surface by the electrolyte ions and give additional pseudocapacitance [18-19].

In summary, activated carbons have been widely used as supercapacitor electrode materials. However, the limited energy storage and rate capability of the activated carbons limit their more widely commercial applications. Although activated carbons can provide a high specific surface area, the pore structure and control of pore size distribution are still challenging at the present stage. Therefore, the design of activated carbons to have suitable size distribution (access to transport of ions in the electrolyte) with an interconnected pore structure and short pore length together with controlled surface chemistry can offer the possibility to achieve an enhanced energy density of supercapacitors, without deteriorating their long cycle life and high power density.

1.3.1.2 Carbon nanotubes (CNTs)

The discovery of carbon nanotubes has much promoted the development of carbon-based electrode materials. Carbon nanotubes, as EDLCs electrode materials, have gained enormous attention due to their superior electrical properties, unique pore structure, and good mechanical and thermal stability [20-22]. CNTs can be divided into single-walled/multi-walled carbon nanotubes, both of which have been widely used as supercapacitor electrode materials. Usually, due to their excellent electrical conductivity and readily accessible surface area, CNTs are considered as the choice of the high-power electrode materials. Besides, the open tubular network and high mechanical resilience of CNTs make them an excellent support for active materials. However, due to CNTs have a relatively small specific surface area (generally < 500 m^2/ g), the energy density of CNTs electrode is lower than activated carbon electrode. And more important, it is the difficulty in retaining the intrinsic properties of individual CNTs on a macroscopic scale [21] and the electrolyte-dependent capacitance performance [20].

Recent studies show that aligned CNTs are more efficient in facilitating fast ionic transportation when compared with entangled CNTs, due to the irregular pore structures and high entanglement of the CNT structure in entangled CNTs [23]. Therefore, the design of aligned CNT seems to be easier to obtain high power performance. Another way to enhance the electrochemical performance is by modifying CNTs with active materials to realize pseudocapacitance through faradic reaction.

In short, despite their superior performances, the limited surface area of CNTs restricted their use as high energy performance supercapacitors. Therefore, the present difficulty in purification and high cost of production still limit their more widely practical applications.

1.3.1.3 Templated carbons

A templating method, as a very useful synthesis method, can fabricate nanostructured carbons with well-controlled narrow pore size distributions, ordered pore structures, and large specific surface areas. In a typical synthesis process, templated carbons are infiltration of a carbon precursor into the pores of the template, followed by a carbonization treatment and finally the removal of the template to leave behind a porous carbon structure.

Based on different types of template and carbon precursors, some studies have produced various carbon structures with well controlled micropores, mesopores and/or macropores [24-26]. Compared to activated carbons, whose micropores are essentially disordered and broad in pore size distribution, the templated microporous carbons are better for use as high energy density electrode materials due to their narrow pore size distribution, well adapted pore size to the electrolyte ions and the ordered straight pore channels. Besides, the well-controlled porous structure of templated carbons can facilitate efficient use of pseudocapacitance from the oxygenated and nitrogenated functionalities of the carbon materials.

Through careful selection of the template materials, carbon precursors and with good control over the carbonization process, templating method can obtain templated carbons with desirable physical and chemical properties. Despite the cost, templated carbons are suitable materials to study, which provide valuable information about the effect of pore size, pore shape, channel structures and other parameters on the ion diffusion and charge storage in the nanoconfined system.

1.3.1.4 Other carbon structures

Other carbon structures such as activated carbon fibers and carbon aerogels have also been studied for supercapacitor electrode material applications. The general rules for the selection of supercapacitor electrode materials are a high and an accessible specific surface area with good electrical conductivity. Activated carbon fibers typically have high specific surface areas, up to 3000 m^2/g, and a more or less controllable pore size distribution [27]. Carbon aerogels are other interesting material suitable for use as a supercapacitor electrode. They are ultralight, highly porous materials, predominantly with mesopores, and have the possibility of usage without binding substances [28].

1.3.2 Metal oxides/hydroxides

Compared to carbon materials for EDLCs, the metal oxides/hydroxides for pseudocapacitors can provide higher energy density due to their charge storage through both faradic redox reactions and the electrochemical adsorption/desorption of ions at the electrode/electrolyte interface.

The general requirements for metal oxides/hydroxides as supercapacitor electrode materials are: [4] (1) good electrical conductivity, (2) the metal can exist in two or more oxidation states that coexist over a continuous range with no phase changes, and (3) enable protons to freely intercalate into oxide lattice on reduction, allowing facile interconversion of $O^{2-} \leftrightarrow OH^-$. To date, the most commonly used electroactive materials include ruthenium oxide (RuO_2), manganese oxide (MnO_2), cobalt oxide/hydroxide (Co_3O_4/$Co(OH)_2$), nickel oxide/hydroxide (NiO/$Ni(OH)_2$), iron oxide (Fe_2O_3 and Fe_3O_4), binary metal oxide, and other metal oxides.

1.3.2.1 RuO_2

The earliest studied transition metal oxide was RuO_2 due to its high theoretical specific capacitance, high electric conductivity, high rate capability, wide potential window, good electrochemical reversibility, and long cycle life [29-32]. In an acidic electrolyte, the pseudocapacitive behavior of RuO_2 can be described as a fast and a reversible faradaic reaction accompanied by electro-absorption of protons on the surface of active material, which can be explained by reaction equation (1) [7]:

$$\mathrm{RuO_2 + xH^+ + xe^- \leftrightarrow RuO_{2-x}(OH)_x} \qquad (1)$$

Despite the remarkable performance of RuO_2 material, it is still not suitable for commercial application in supercapacitors, due to its high cost and environmental harmfulness [33]. To solve this problem, significant efforts have been devoted to developing low-cost and environmentally friendly materials that present electrochemical behavior similar to that of RuO_2.

1.3.2.2 MnO_2

In order to reduce the cost of electrode materials, an alternative approach is to develop cheap metal oxides/hydroxides to replace RuO_2. These alternative materials include MnO_2, Co_3O_4/$Co(OH)_2$, NiO/$Ni(OH)_2$, Fe_2O_3/Fe_3O_4, binary metal oxide, and other metal oxides.

As an alternative to replacing RuO_2, various forms of MnO_2 have been fabricated for supercapacitor electrode materials due to their high theoretical specific capacitance (from 1100 to 1300 F/g) [34], low cost, large abundance, and environmental safety [35-36]. The capacitance of MnO_2 mainly comes from pseudocapacitance. There are two mechanisms proposed to explain the MnO_2 charge storage behavior [36-37]. The first one implies the insertion of electrolyte cations into the bulk of the electrode material. It can be expressed as an equation (2). The second one is based on the surface adsorption of electrolyte cations on the MnO_2. It can be expressed as an equation (3).

$$\mathrm{MnO_2 + C^+ + e^- \leftrightarrow MnOOC} \qquad (2)$$

$$\mathrm{(MnO_2)_{surface} + C^+ + e^- \leftrightarrow (MnOOC)_{surface}} \qquad (3)$$

where C^+ denotes the protons and alkali metal cations (Li^+, Na^+, K^+) in the electrolyte. Both the mechanisms involve a redox reaction between the III and IV oxidation states of Mn.

Although the theoretical specific capacitance of MnO_2 is pretty high, the practical specific capacitance of unmodified MnO_2 is usually lower than 350 F/g, which is not comparable to RuO_2 [34]. In addition, MnO_2 electrode is also suffered capacitance degradation during cycling, low surface area, and poor electronic conductivity. To solve these problems, the studies on MnO_2 nanostructured [38-40] and MnO_2 composite materials [41-44] are both feasible ways.

1.3.2.3 Co_3O_4/$Co(OH)_2$

Co_3O_4 has been considered a promising electrode material for supercapacitor due to it seems excellent reversible redox behavior, large surface area, high conductivity, long-term performance, and good corrosion stability [45-47]. The redox reactions of Co_3O_4 can be described as follows equation (4) and (5) [48]:

$$Co_3O_4 + OH^- + H_2O \leftrightarrow 3\,CoOOH + e^- \qquad (4)$$

$$CoOOH + OH^- \leftrightarrow CoO_2 + H_2O + e^- \qquad (5)$$

Co_3O_4, as a p-type semiconductor, has low electronic and ionic conductivity, leading to the poor rate capability. Co_3O_4 structure also suffers from a large volume change during the cycle process, resulting in a short cycle life [49]. These recent studies indicate that the appropriate morphology and microstructure are necessary to achieve an enhanced electrochemical performance of Co_3O_4-based supercapacitor [50-52].

$Co(OH)_2$-based electrode materials are attractive due to their layered structure and large interlayer spacing, which promises high surface area and a fast ion insertion/desertion rate [53]. The redox reactions can be expressed in equation (6) and (7) [54-55]. However, its shortcomings are still poor rate capability and cycle stability.

$$Co(OH)_2 + OH^- \leftrightarrow CoOOH + H_2O + e^- \qquad (6)$$

$$CoOOH + OH^- \leftrightarrow CoO_2 + H_2O + e^- \qquad (7)$$

In summary, the specific capacitances of $Co(OH)_2$-based supercapacitor electrodes higher than that of Co_3O_4. However, such high specific capacitance of $Co(OH)_2$ is only located in low potential ranges, which limits its practical application in supercapacitors.

1.3.2.4 NiO/$Ni(OH)_2$

Nickel oxide is considered an alternative electrode material for supercapacitor in alkaline electrolytes due to its easy synthesis, relatively high specific capacitance, environment friendliness, and low cost [56-57]. The redox reaction of nickel oxide in a KOH electrolyte can be expressed by reaction equation (8) [58].

$$NiO + OH^- \leftrightarrow NiOOH + e^- \qquad (8)$$

At this stage, NiO electrode materials are suffering their poor cycle performance and low electrical conductivity. To address these problems, fabricating nanostructured NiO and composing NiO with other materials are both feasible.

$Ni(OH)_2$ is a hexagonal layered structure and has two polymorphs, α- and β-$Ni(OH)_2$ [59]. α-$Ni(OH)_2$ is a hydroxyl-deficient phase with interlayered anions and water molecules. β-$Ni(OH)_2$ possesses a brucite structure without water molecules. Compared to NiO electrode material, $Ni(OH)_2$ can yield much higher specific capacitances. Further optimize its porous structure, $Ni(OH)_2$ can be achieved much better performance.

1.3.2.5. Binary metal oxides

Recently, binary metal oxides with spinel structures have received much attention, such as $NiFe_2O_4$ [60], $NiCo_2O_4$ [61], $ZnMnO_4$ [62], $CoFe_2O_4$ [63], $ZnCo_2O_4$ [64] and $CoMn_2O_4$ [65]. Some recent studies indicate that the electrical conductivity of these binary metal oxides is higher than that of unitary metal oxides and contain both components contributions to the total capacitance, which result in better electrochemical performance than individual components [66-67].

1.3.2.6 Other metal oxides

Many other metal oxide materials, such as V_2O_5 [68], SnO [69], Bi_2O_3 [70], MoO_2 [71] and TiO_2 [72], have also been extensively studied by researchers. But these materials usually suffer from low capacitance or some other drawbacks. They may become promising supercapacitive materials if researchers make breakthroughs in solving their shortcomings.

1.3.3 Conducting polymers (CPs)

Conducting polymers are generally attractive electrode material for supercapacitor as they have high conductivity, high voltage window, high storage capacity/porosity/reversibility, low cost, and low environmental impact [73-75].

Conducting polymers stores charge through a redox reaction. When oxidation takes place, ions are transferred to the polymer backbone, and when reduction occurs, the ions are released from this backbone into the electrolyte. The redox reaction in the polymer backbone occurs throughout the bulk of the material, not only on the surface [76]. As the charging/discharging process does not involve any phase changes, the processes are highly reversible.

Conducting polymers can be p-doped with (counter) anions when oxidized and n-doped with (counter) cations when reduced. The simplified equations for these two charging/discharging processes are as follows:

$$\mathrm{CPs} \leftrightarrow \mathrm{CPs}^{n+}(\mathrm{A}^-)_n + ne^- \quad \text{(p-doped)} \quad (9)$$

$$\mathrm{CPs} + ne^- \leftrightarrow (\mathrm{C}^+)_n\mathrm{CPs}^{n-} \quad \text{(n-doping)} \quad (10)$$

The conducting polymers that are most commonly studied for use in supercapacitor electrode material are polypyrrole (PPy), polyaniline (PANI), polythiophene (PTh), and their corresponding derivatives [77]. PPy and PANI are usually in the form of p-doped type due to their n-doping potentials are much lower than the reduction potential of common electrolyte solutions. So, they are generally used as cathode materials. PTh and its derivatives can be in the form of p-doped and n-doped type.

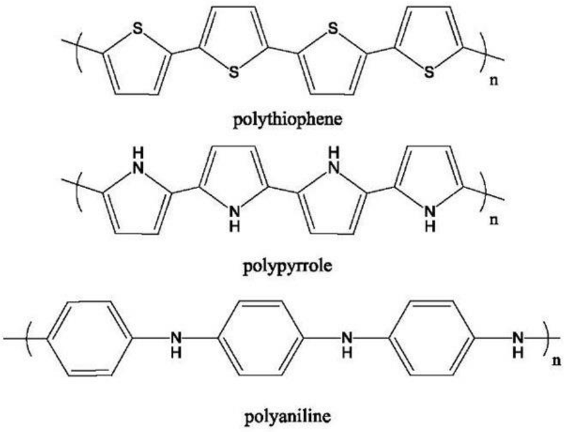

Figure 1.4. Chemical structure of typical conducting polymer.

Unfortunately, swelling and shrinking of conducting polymer may occur during the doping/de-doping (intercalation/deintercalation) of ions. These problems often lead to mechanical degradation of the electrode, causes fading electrochemical performance under prolonged cycling. Conducting polymer, as an electrode material, usually remarkably degrade under less than a thousand cycles. It has been reported that the PPy electrodes showed an initial capacitance of 120 F/g at a current density of 2 mA/cm^2, which was degraded by ~50% within one thousand cycles [78]. PANI also suffered from a similarly serious problem due to its volumetric changes during the intercalation/deintercalation process. The capacity degradation of PANI nanorods could be as high as 29.5% within 1000 cycles between 0.2 and 0.8 V [79]. As to PTh, the relatively poor stability of the n-doped state could lead to a continuous decrease in electrochemical performance under long cycling [80]. Apparently, poor cycle life is a very serious problem for conducting polymer materials when they are used as supercapacitor electrode.

To solve the problem of low stability of conducting polymer electrodes, many efforts have been devoted to realizing improved electrochemical performance. (1) Design nanostructured conducting polymer materials. Nanostructured conducting polymers, such as nanofibers, nanorods, nanowires, and nanotubes, have received much attention. Because they could reduce cycling degradation problems caused by volumetric changes or mechanical forces by providing a relatively short diffusion length to enhance the utilization of electrode materials. It has been reported that the packed nanometer-scale PANI whisker discharge capacitance loss was about 5% after 3000 cycles, which indicated the materials have long-term electrochemical stability [81]. (2) Fabricating composite electrode materials. It was demonstrated the development of composite conducting polymer electrodes such as couple other materials such as carbon materials or metal oxides could enhance the cycling stability. For example, PANI/GO composites showed excellent electrochemical performance, high electrochemical capacitance, and long cycling stability (~92% retention after 2000 cycles) [82]. Compared with pure PPy electrodes whose loss in specific capacitance was close to 50%, the MnO_2/PPy nanocomposite electrodes showed a relatively stable performance degrading only by ~10% in the initial 1000 cycles and a relatively stable performance at much higher specific capacity is seen in the subsequent 4000 cycles at a current density of 2 mA/cm^2 [78]. Recent research finds that conducting polymer composite materials can give a wide distribution of capacitance values, which are also dependent on many parameters such as the electrolytes, current load, scan rate, constituents of composites, and the mass ratio of the components as well as cell configuration. Therefore, more efforts are still needed to optimize these parameters to achieve optimized electrochemical properties of these conducting polymer-based composites for supercapacitor applications [4].

1.3.4 Trends in supercapacitor electrodes

To develop new materials with optimal performance, two important research directions in supercapacitor electrode exploration are:

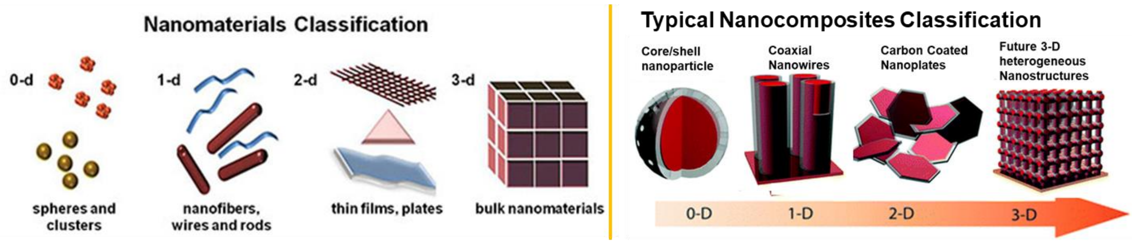

Figure 1.5. Typical nanomaterials and nanocomposites classification [83-84].

(1) Synthesis of novel nanostructured electrode materials

In the design of electrode materials, the favored properties of electrode materials include large active surface area, high electric conductivity of the active material, and excellent connection and contact between active materials and substrates. Apparently, the capacitance of supercapacitor heavily depends on the specific surface area of the electrode materials. Material morphology is closely related to the specific surface area and the diffusion of ions in the electrode. Nanostructured materials possess a high specific surface area. They can provide short transport/diffusion path lengths for ions and electrons, leading to faster kinetics, more efficient contact of electrolyte ions, and more electroactive sites for faradaic energy storage, resulting in high charge/discharge capacities even at high current densities.

(2) Design of composite electrode materials

The composite design is the future trend in the development of electrode materials. The individual substances in the composites can have a synergistic effect through minimizing particle size, enhancing specific surface area, inducing porosity, preventing particles from agglomerating, facilitating electron and proton conduction, expanding active sites, extending the potential window, protecting active materials from mechanical degradation. And the composite can significantly improve cycling stability, and providing extra pseudocapacitance. As a result, the obtained composites can overcome the drawbacks of the individual substances and embody the advantages of all constituents.

1.4 Electrolytes for Supercapacitors

The electrolytes used in supercapacitor devices are as significant as the electrode materials, because they define the performance of supercapacitors, especially the energy density. Up to now, various types of electrolytes have been developed by researchers. The electrolyte used in supercapacitor can be classified into three types: (1) aqueous electrolyte, (2) organic electrolyte, (3) ionic liquids electrolyte, and (4) solid-state polymer electrolyte.

(1) Aqueous electrolyte

Compared with organic electrolytes, aqueous electrolytes gave higher capacitance and higher power than those with organic electrolytes, probably due to higher ionic concentration and smaller ionic radius. Besides, aqueous electrolytes can be prepared and utilized without stringently controlling the preparing processes and conditions, while organic ones need strict processes and conditions to obtain ultra-pure electrolytes.

Unfortunately, aqueous electrolytes have a large limitation in terms of improving both energy and power densities due to their narrow voltage window as low as about 1.2 V, much lower than those of organic electrolytes. This is the reason why organic electrolytes are often recommended.

(2) Organic electrolyte

Compared to aqueous electrolytes, organic electrolytes can provide a voltage window as high as 3.5 V. This is a significant advantage of organic over aqueous electrolytes. Among organic electrolytes, acetonitrile, and propylene carbonate (PC) are the most commonly used solvents. Acetonitrile can dissolve larger amounts of salt than other solvents, but suffers from environmental and toxic problems. PC-based electrolytes are friendly to the environment and can offer a wide electrochemical window, a wide range of operating temperature, as well as good conductivity. Besides, organic salts such as tetraethylammonium tetrafluoroborate, tetraethyl phosphonium tetrafluoroborate, and triethylmethylammonium tetrafluoroborate (TEMABF4) have also been used in supercapacitor electrolytes.

(3) Ionic liquids electrolyte

Recently, ionic liquids have received significant interest as alternative electrolytes for supercapacitors because of their negligible volatility, high thermal, chemical and electrochemical stability, low flammability, and wide electrochemical stability window of 4.5 V. The main ionic liquids studied for supercapacitor applications are imidazolium, pyrrolidinium, as well as asymmetric, aliphatic quaternary ammonium salts with anions such as tetrafluoroborate, trifluoromethanesulfonate, bis(trifluoromethanesulfonyl)imide, bis(fluorosulfonyl)imide or hexafluorophosphate [85]. The challenge for ionic liquids is to design them having a wider potential range together with high conductivity in a wide temperature range.

(4) Solid-state polymer electrolyte

Solid polymer electrolyte-based supercapacitors have attracted considerable interest in recent years due to the rapidly growing demand for power for various types of electronics. The solid polymer electrolytes can act as ionic conducting media and electrode separators. There are three types of polymer-based solid electrolyte for supercapacitors: dry polymer electrolyte, gel polymer electrolyte, and polyelectrolyte. Among these, the gel polymer electrolyte has recently been the most extensively investigated electrolyte because of its high ionic conductivity. Additionally, the gel polymer electrolyte is known as a hydrogel polymer electrolyte when using water as the plasticizer. And this type of hydrogel polymer electrolyte generally possesses three-dimensional polymeric networks. Owing to easy preparation, excellent hydrophilicity, outstanding film-forming properties, non-toxic features, and low cost, poly(vinyl alcohol) (PVA) has been the most greatly investigated polymer matrix to date, and is commonly mixed with other aqueous solutions [86].

1.5 Supercapacitor Systems

According to the composition difference of electrode materials, supercapacitor devices can be classed as follows: symmetric supercapacitor, asymmetric supercapacitor, and hybrid supercapacitor, as shown in Figure 1.6. The classification of supercapacitor categories has been well reviewed recently [10, 87]; herein, we briefly describe the characteristics of symmetric, asymmetric, and hybrid supercapacitors.

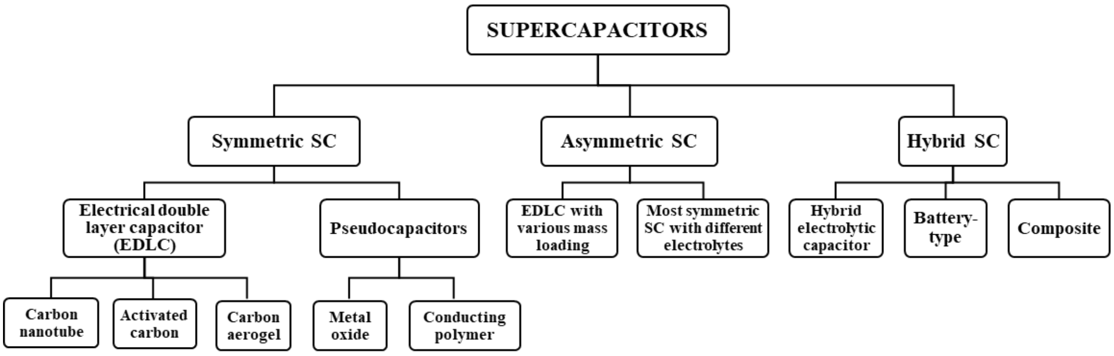

Figure 1.6. Classification of supercapacitor categories and classes [10, 87].

1.5.1 Symmetric supercapacitors

Symmetric supercapacitors are typically composed of two identical supercapacitor-type electrodes, including activated carbons (AC) and pseudocapacitive materials. It is noted that, although the symmetric supercapacitors are using the same supercapacitor-type materials as the positive and negative electrode, the masses of the two electrodes are different based on the different electrolyte ions absorbed on the positive and negative electrodes during the charge-discharge process.

1.5.2 Asymmetric supercapacitors

Asymmetric supercapacitors are composed of two different supercapacitor-type electrodes, one electrode being of a double layer carbon material and the other being of a pseudocapacitance material. For example, AC//MnO_2 is one type of promising asymmetric supercapacitor and has recently been widely studied for energy storage [88].

1.5.3 Hybrid supercapacitors

Hybrid supercapacitors are typically composed of a supercapacitor-type electrode and a battery-type electrode [89-91]. Recently, many hybrid systems have been reported in aqueous or nonaqueous electrolytes, such as AC//PbO_2, AC//$Ni(OH)_2$, AC//$Li_4Ti_5O_{12}$, AC//graphite, and AC//$LiMn_2O_4$ [87].

1.6 Objectives and Scope of the Dissertation

As mentioned above, the electrode material is the most critical part of supercapacitor, and it is also a critical factor in determining its performance. Pseudocapacitor has the potential to achieve higher specific capacitance and higher energy storage compared to EDLC. In this thesis, the pseudocapacitors electrode materials are mainly studied, include metal oxides/hydroxides and conducting polymers. To obtain new electrode materials with high electrochemical performance, two major research directions are the synthesis of nanostructured electrode materials and composite materials.

Specifically, the intention of this dissertation research is to develop nanostructured metal oxide/hydroxide and metal oxide/hydroxide with conducting polymer hybrid electrodes to realize improved electrochemical performance in terms of specific capacitance, energy and power densities, and cycling stability.

In more specific terms, the main objective of this research is to develop nanostructured metal oxide/hydroxide and metal oxide/hydroxide with conducting polymer hybrid electrodes for supercapacitors with the following considerations.

(1) Development of porous nanostructured metal oxide/hydroxide electrodes with different morphologies by hydrothermal method. Usually, the nanostructured porous materials can facilitate ionic motion, improve the rate capability, and increase the utilization of active materials. In this thesis, the CoAl, NiAl and NiFe layered double hydroxides (LDHs) nanosheet films were first synthesized. The LDHs nanosheet films with porous structure were grown perpendicularly on the substrate as binder-free electrodes. In addition, the preparation of

oriented CoAl LDH nanosheet was achieved by hydrothermal grow and slip casting with the assistance of a strong magnetic field. The hexagonal tungsten oxide (h-WO_3) nanowire films with porous structure were also synthesized. The h-WO_3 nanowire films can grow directly on the substrate as a binder-free electrode.

(2) Design and fabrication of metal oxide/hydroxide with conducting polymer hybrid electrodes. Unfortunately, transition metal oxides/hydroxides are mostly low electric conductivity, and as a result, it is challenging to build effective supercapacitors based on pure metal oxides/hydroxides electrodes. In this thesis, we report a new strategy for achieving high performance supercapacitors and overcoming the low electric conductivity problems of transition metal oxides/hydroxides by hybridization metal oxides/hydroxides with a conductive polymer, polyaniline (PANI). A synergistic effect is observed in this strategy. The deposited PANI can efficiently improve the conductivity of metal oxides/hydroxides and enhance faradaic processes across the interface. In this thesis, we mainly synthesized CoAl LDH-PANI and WO_3-PANI hybrid nanomaterials by the hydrothermal-electrodeposition method.

(3) Identification of the effect of PANI content in the hybrid materials on the electrochemical performance of supercapacitors in order to maximize the specific capacitance and energy density. The mechanism for the synergistic effects was proposed.

(4) Structural characterization of electrode materials using the following: Fourier transform infrared spectrometer (FTIR), X-ray diffraction (XRD), synchrotron X-ray diffraction (SXRD), field emission scanning electron microscopy (SEM), energy dispersive X-ray spectroscopy (EDX), and X-ray photoelectron spectroscopy (XPS).

(5) Evaluation and optimization of electrochemical performances, such as specific capacitance, rate ability, equivalent series resistance (ESR), energy density, power density, and cycle life of the fabricated supercapacitors using the synthesized materials.

1.7 Organization of the Dissertation

The structure of this dissertation can be summarized as follows.

In Chapter 1, it focuses on the literature review on supercapacitors, including energy storage mechanisms, electrode materials, electrolytes, and classification of supercapacitors.

In Chapter 2, a series of layered double hydroxides (LDHs) CoAl LDH, NiAl LDH, and NiFe LDH nanosheet films with porous structures were successfully synthesized by hydrothermal methods. The LDHs nanosheet films were grown perpendicularly on the substrate and examined them as binder-free electrodes for pseudocapacitors. The CoAl LDH has the best reversibility and the highest capacitance among the three types of LDHs, which make it promising candidates for practical application as supercapacitor electrode materials.

In Chapter 3, a novel inner/outer layer structured CoAl LDH-PANI hybrid nanomaterial was successfully synthesized through the hydrothermal-electrodeposition process. The hybrid architecture CoAl LDH-PANI exhibited greatly enhanced specific capacitance and cycling stability and was superior to the non-decorated CoAl LDH.

In Chapter 4, the preparation of oriented CoAl LDH nanosheets was studied by hydrothermal grow and slip casting with the assistance of an external magnetic field. The preferred growth orientation of CoAl LDH nanosheets was obtained with the assistance of an external magnetic field. The addition of a strong magnetic field has no change the crystal phase, but the obvious reduced the amount of interlayer water molecules in CoAl LDH. The supplemental strong magnetic field provides a novel strategy for developing an oriented microstructure.

In Chapter 5, the hybrid architecture WO_3-PANI was successfully synthesized through the hydrothermal-electrodeposition process. The hybrid architecture WO_3-PANI exhibited an outstanding areal specific capacitance, good rate capability, and excellent cycling stability. The fabricated all-solid-state supercapacitor device also exhibited high flexibility, high capacitance retention, and long lifetime.

In Chapter 6, it mainly concludes the dissertation with major findings and focuses on future research recommended for the future development of supercapacitors.

Reference

1. Zervos, A.; Network R., Renewables 2018 global status report - REN21. **2018**.
2. Kandalkar, S.; Dhawale, D.; Kim, C.K.; Lokhande, C., Chemical synthesis of cobalt oxide thin film electrode for supercapacitor application. *Synthetic Metals* **2010,** *160* (11-12), 1299-1302.
3. Largeot, C.; Portet, C.; Chmiola, J.; Taberna, P.L.; Gogotsi, Y.; Simon, P., Relation between the ion size and pore size for an electric double-layer capacitor. *Journal of the American Chemical Society* **2008,** *130* (9), 2730-2731.
4. Wang, G.; Zhang, L.; Zhang, J., A review of electrode materials for electrochemical supercapacitors. *Chemical Society Reviews* **2012,** *41* (2), 797-828.
5. Yu, G.; Xie, X.; Pan, L.; Bao, Z.; Cui, Y., Hybrid nanostructured materials for high-performance electrochemical capacitors. *Nano Energy* **2013,** *2* (2), 213-234.
6. Simon, P.; Gogotsi, Y., Materials for electrochemical capacitors. In *Nanoscience And Technology: A Collection of Reviews from Nature Journals* **2010**, 320-329.
7. Winter, M.; Brodd, R.J., What are batteries, fuel cells, and supercapacitors? ACS Publications: **2004**, 4245-4270.
8. Yu, Z.; Tetard, L.; Zhai, L.; Thomas, J., Supercapacitor electrode materials: nanostructures from 0 to 3 dimensions. *Energy & Environmental Science* **2015,** *8* (3), 702-730.
9. Long, J.W.; Bélanger, D.; Brousse, T., Asymmetric electrochemical capacitors-Stretching the limits of aqueous electrolytes. MRS Bulletin, 2011, *36*(7): 513-522.
10. Conte, M., Supercapacitors technical requirements for new applications. *Fuel cells* **2010,** *10* (5), 806-818.
11. Chuang, C.M.; Huang, C.W.; Teng, H.; Ting, J.M., Effects of carbon nanotube grafting on the performance of electric double layer capacitors. *Energy & Fuels* **2010,** *24* (12), 6476-6482.
12. Arico, A.S.; Bruce, P.; Scrosati, B.; Tarascon, J.M.; Van Schalkwijk, W., Nanostructured materials for advanced energy conversion and storage devices. *Materials For Sustainable Energy: A Collection of Peer-Reviewed Research and Review Articles from Nature Publishing Group* **2011**, 148-159.
13. Choi, D.; Kumta, P.N., Nanocrystalline TiN derived by a two-step halide approach for electrochemical capacitors. *Journal of the Electrochemical Society* **2006,** *153* (12), A2298-A2303.
14. Lee, H.; Cho, M.S.; Kim, I.H.; Do Nam, J.; Lee, Y., RuO_x/polypyrrole nanocomposite electrode for electrochemical capacitors. *Synthetic Metals* **2010,** *160* (9-10), 1055-1059.

15. Zhang, Y.; Feng, H.; Wu, X.; Wang, L.; Zhang, A.; Xia, T.; Dong, H.; Li, X.; Zhang, L., Progress of electrochemical capacitor electrode materials: A review. *International journal of hydrogen energy* **2009,** *34* (11), 4889-4899.
16. Liu, C.; Li, F.; Ma, L.P.; Cheng, H.M., Advanced materials for energy storage. *Advanced materials* **2010,** *22* (8), E28-E62.
17. Kierzek, K.; Frackowiak, E.; Lota, G.; Gryglewicz, G.; Machnikowski, J., Electrochemical capacitors based on highly porous carbons prepared by KOH activation. *Electrochimica Acta* **2004,** *49* (4), 515-523.
18. Raymundo-Piñero, E.; Leroux, F.; Béguin, F., A high-performance carbon for supercapacitors obtained by carbonization of a seaweed biopolymer. *Advanced Materials* **2006,** *18* (14), 1877-1882.
19. Seredych, M.; Hulicova-Jurcakova, D.; Lu, G.Q.; Bandosz, T.J., Surface functional groups of carbons and the effects of their chemical character, density and accessibility to ions on electrochemical performance. *Carbon* **2008,** *46* (11), 1475-1488.
20. Frackowiak, E.; Jurewicz, K.; Delpeux, S.; Béguin, F., Nanotubular materials for supercapacitors. *Journal of Power Sources* **2001,** *97*, 822-825.
21. Futaba, D.N.; Hata, K.; Yamada, T.; Hiraoka, T.; Hayamizu, Y.; Kakudate, Y.; Tanaike, O.; Hatori, H.; Yumura, M.; Iijima, S., Shape-engineerable and highly densely packed single-walled carbon nanotubes and their application as super-capacitor electrodes. *Nature materials* **2006,** *5* (12), 987.
22. Niu, C.; Sichel, E.K.; Hoch, R.; Moy, D.; Tennent, H., High power electrochemical capacitors based on carbon nanotube electrodes. *Applied Physics Letters* **1997,** *70* (11), 1480-1482.
23. Zhang, H.; Cao, G.; Yang, Y.; Gu, Z., Comparison between electrochemical properties of aligned carbon nanotube array and entangled carbon nanotube electrodes. *Journal of The Electrochemical Society* **2008,** *155* (2), K19-K22.
24. Ania, C.O.; Khomenko, V.; Raymundo-Piñero, E.; Parra, J.B.; Beguin, F., The large electrochemical capacitance of microporous doped carbon obtained by using a zeolite template. *Advanced Functional Materials* **2007,** *17* (11), 1828-1836.
25. Li, W.; Chen, D.; Li, Z.; Shi, Y.; Wan, Y.; Wang, G.; Jiang, Z.; Zhao, D., Nitrogen-containing carbon spheres with very large uniform mesopores: the superior electrode materials for EDLC in organic electrolyte. *Carbon* **2007,** *45* (9), 1757-1763.
26. Wang, D.W.; Li, F.; Liu, M.; Lu, G.Q.; Cheng, H.M., 3D aperiodic hierarchical porous graphitic carbon material for high-rate electrochemical capacitive energy storage. *Angewandte Chemie International Edition* **2008,** *47* (2), 373-376.

27. Xu, B.; Wu, F.; Chen, R.; Cao, G.; Chen, S.; Zhou, Z.; Yang, Y., Highly mesoporous and high surface area carbon: a high capacitance electrode material for EDLCs with various electrolytes. *Electrochemistry Communications* **2008,** *10* (5), 795-797.
28. Zhang, L.L.; Zhao, X., Carbon-based materials as supercapacitor electrodes. *Chemical Society Reviews* **2009,** *38* (9), 2520-2531.
29. Yan, J.; Wang, Q.; Wei, T.; Fan, Z., Recent advances in design and fabrication of electrochemical supercapacitors with high energy densities. *Advanced Energy Materials* **2014,** *4* (4), 1300816.
30. Jia, Q.; Song, S.; Wu, X.; Cho, J.; Foltyn, S.; Findikoglu, A.; Smith, J., Epitaxial growth of highly conductive RuO_2 thin films on (100) Si. *Applied physics letters* **1996,** *68* (8), 1069-1071.
31. Kim, I.H.; Kim, K.B., Electrochemical characterization of hydrous ruthenium oxide thin-film electrodes for electrochemical capacitor applications. *Journal of The Electrochemical Society* **2006,** *153* (2), A383-A389.
32. Sakiyama, K.; Onishi, S.; Ishihara, K.; Orita, K.; Kajiyama, T.; Hosoda, N.; Hara, T., Deposition and properties of reactively sputtered ruthenium dioxide films. *Journal of The Electrochemical Society* **1993,** *140* (3), 834-839.
33. Fan, L.Z.; Hu, Y.S.; Maier, J.; Adelhelm, P.; Smarsly, B.; Antonietti, M., High electroactivity of polyaniline in supercapacitors by using a hierarchically porous carbon monolith as a support. *Advanced Functional Materials* **2007,** *17* (16), 3083-3087.
34. Wei, W.; Cui, X.; Chen, W.; Ivey, D.G., Manganese oxide-based materials as electrochemical supercapacitor electrodes. *Chemical society reviews* **2011,** *40* (3), 1697-1721.
35. Pang, S.C.; Anderson, M.A.; Chapman, T.W., Novel electrode materials for thin-film ultracapacitors: comparison of electrochemical properties of sol-gel-derived and electrodeposited manganese dioxide. *Journal of the Electrochemical Society* **2000,** *147* (2), 444-450.
36. Toupin, M.; Brousse, T.; Bélanger, D., Charge storage mechanism of MnO_2 electrode used in aqueous electrochemical capacitor. *Chemistry of Materials* **2004,** *16* (16), 3184-3190.
37. Zhu, J.; Shi, W.; Xiao, N.; Rui, X.; Tan, H.; Lu, X.; Hng, H.H.; Ma, J.; Yan, Q., Oxidation-etching preparation of MnO_2 tubular nanostructures for high-performance supercapacitors. *ACS applied materials & interfaces* **2012,** *4* (5), 2769-2774.
38. Dubal, D.; Dhawale, D.S.; Salunkhe, R.; Lokhande, C., Conversion of interlocked cube-like Mn_3O_4 into nanoflakes of layered birnessite MnO_2 during supercapacitive studies. *Journal of Alloys and Compounds* **2010,** *496* (1-2), 370-375.

39. Nam, H.S.; Yoon, J.K.; Ko, J.M.; Kim, J.D., Electrochemical capacitors of flower-like and nanowire structured MnO_2 by a sonochemical method. *Materials Chemistry and Physics* **2010,** *123* (1), 331-336.
40. Xia, H.; Feng, J.; Wang, H.; Lai, M.O.; Lu, L., MnO_2 nanotube and nanowire arrays by electrochemical deposition for supercapacitors. *Journal of Power Sources* **2010,** *195* (13), 4410-4413.
41. Bordjiba, T.; Bélanger, D., Direct redox deposition of manganese oxide on multiscaled carbon nanotube/microfiber carbon electrode for electrochemical capacitor. *Journal of The Electrochemical Society* **2009,** *156* (5), A378-A384.
42. Chen, S.; Zhu, J.; Wu, X.; Han, Q.; Wang, X., Graphene oxide-MnO_2 nanocomposites for supercapacitors. *ACS nano* **2010,** *4* (5), 2822-2830.
43. Hou, Y.; Cheng, Y.; Hobson, T.; Liu, J., Design and synthesis of hierarchical MnO_2 nanospheres/carbon nanotubes/conducting polymer ternary composite for high performance electrochemical electrodes. *Nano letters* **2010,** *10* (7), 2727-2733.
44. Wang, Y.; Foo, C.Y.; Hoo, T.K.; Ng, M.; Lin, J., Designed smart system of the sandwiched and concentric architecture of RuO_2/C/RuO_2 for high performance in electrochemical energy storage. *Chemistry-A European Journal* **2010,** *16* (12), 3598-3603.
45. Liu, T.C.; Pell, W.; Conway, B., Stages in the development of thick cobalt oxide films exhibiting reversible redox behavior and pseudocapacitance. *Electrochimica Acta* **1999,** *44* (17), 2829-2842.
46. Kim, H.K.; Seong, T.Y.; Lim, J.H.; Cho, W.I.; Yoon, Y.S., Electrochemical and structural properties of radio frequency sputtered cobalt oxide electrodes for thin-film supercapacitors. *Journal of power sources* **2001,** *102* (1-2), 167-171.
47. Srinivasan, V.; Weidner, J.W., Capacitance studies of cobalt oxide films formed via electrochemical precipitation. *Journal of power sources* **2002,** *108* (1-2), 15-20.
48. Shan, Y.; Gao, L., Formation and characterization of multi-walled carbon nanotubes/Co_3O_4 nanocomposites for supercapacitors. *Materials chemistry and physics* **2007,** *103* (2-3), 206-210.
49. Wang, H.; Holt, C.M.; Li,Z.; Tan, X.; Amirkhiz, B.S.; Xu, Z.; Olsen, B.C.; Stephenson, T.; Mitlin, D., Graphene-nickel cobaltite nanocomposite asymmetrical supercapacitor with commercial level mass loading. *Nano Research* **2012,** *5* (9), 605-617.
50. Gao, Y.; Chen, S.; Cao, D.; Wang, G.; Yin, J., Electrochemical capacitance of Co_3O_4 nanowire arrays supported on nickel foam. *Journal of Power Sources* **2010,** *195* (6), 1757-1760.

51. Wang, G.; Shen, X.; Horvat, J.; Wang, B.; Liu, H.; Wexler, D.; Yao, J., Hydrothermal synthesis and optical, magnetic, and supercapacitance properties of nanoporous cobalt oxide nanorods. *The Journal of Physical Chemistry C* **2009,** *113* (11), 4357-4361.
52. Xu, J.; Gao, L.; Cao, J.; Wang, W.; Chen, Z., Preparation and electrochemical capacitance of cobalt oxide (Co_3O_4) nanotubes as supercapacitor material. *Electrochimica Acta* **2010,** *56* (2), 732-736.
53. Gupta, V.; Kusahara, T.; Toyama, H.; Gupta, S.; Miura, N., Potentiostatically deposited nanostructured α-$Co(OH)_2$: A high performance electrode material for redox-capacitors. *Electrochemistry Communications* **2007,** *9* (9), 2315-2319.
54. Liang, Y.; Schwab, M.G.; Zhi, L.; Mugnaioli, E.; Kolb, U.; Feng, X.; Müllen, K., Direct access to metal or metal oxide nanocrystals integrated with one-dimensional nanoporous carbons for electrochemical energy storage. *Journal of the American Chemical Society* **2010,** *132* (42), 15030-15037.
55. Yu, Z.J.; Dai, Y.; Chen, W., Electrochemical deposited nanoflakes $Co(OH)_2$ porous films for electrochemical capacitors. *Journal of the Chinese Chemical Society* **2010,** *57* (3A), 423-428.
56. Castro, E.; Real, S.; Dick, L.P., Electrochemical characterization of porous nickel-cobalt oxide electrodes. *International journal of hydrogen energy* **2004,** *29* (3), 255-261.
57. Wu, M.S.; Huang, Y.A.; Jow, J.J.; Yang, W.D.; Hsieh, C.Y.; Tsai, H.M., Anodically potentiostatic deposition of flaky nickel oxide nanostructures and their electrochemical performances. *International Journal of Hydrogen Energy* **2008,** *33* (12), 2921-2926.
58. Wang, Y.G.; Xia, Y.Y., Electrochemical capacitance characterization of NiO with ordered mesoporous structure synthesized by template SBA-15. *Electrochimica Acta* **2006,** *51* (16), 3223-3227.
59. Jayashree, R.; Kamath, P.V., Suppression of the $\alpha \rightarrow \beta$-nickel hydroxide transformation in concentrated alkali: Role of dissolved cations. *Journal of applied electrochemistry* **2001,** *31* (12), 1315-1320.
60. Wang, Z.; Zhang, X.; Li, Y.; Liu, Z.; Hao, Z., Synthesis of graphene-$NiFe_2O_4$ nanocomposites and their electrochemical capacitive behavior. *Journal of Materials Chemistry A* **2013,** *1* (21), 6393-6399.
61. Liu, X.; Zhang, Y.; Xia, X.; Shi, S.; Lu, Y.; Wang, X. L.; Gu, C.; Tu, J., Self-assembled porous $NiCo_2O_4$ hetero-structure array for electrochemical capacitor. *Journal of Power Sources* **2013,** *239*, 157-163.
62. Kim, S.W.; Lee, H.W.; Muralidharan, P.; Seo, D.H.; Yoon, W.S.; Kim, D. K.; Kang, K., Electrochemical performance and ex situ analysis of $ZnMn_2O_4$ nanowires as anode materials for lithium rechargeable batteries. *Nano Research* **2011,** *4* (5), 505-510.

63. Xiong, Q.; Tu, J.; Shi, S.; Liu, X.; Wang, X.; Gu, C., Ascorbic acid-assisted synthesis of cobalt ferrite ($CoFe_2O_4$) hierarchical flower-like microspheres with enhanced lithium storage properties. *Journal of Power Sources* **2014,** *256*, 153-159.
64. Karthikeyan, K.; Kalpana, D.; Renganathan, N., Synthesis and characterization of $ZnCo_2O_4$ nanomaterial for symmetric supercapacitor applications. *Ionics* **2009,** *15* (1), 107-110.
65. Yu, L.; Zhang, L.; Wu, H.B.; Zhang, G.; Lou, X.W.D., Controlled synthesis of hierarchical $Co_xMn_{3-x}O_4$ array micro-/nanostructures with tunable morphology and composition as integrated electrodes for lithium-ion batteries. *Energy & Environmental Science* **2013,** *6* (9), 2664-2671.
66. Huang, L.; Chen, D.; Ding, Y.; Feng, S.; Wang, Z.L.; Liu, M., Nickel-cobalt hydroxide nanosheets coated on $NiCo_2O_4$ nanowires grown on carbon fiber paper for high-performance pseudocapacitors. *Nano letters* **2013,** *13* (7), 3135-3139.
67. Yang, W.; Gao, Z.; Ma, J.; Zhang, X.; Wang, J.; Liu, J., Hierarchical $NiCo_2O_4$@ NiO core-shell hetero-structured nanowire arrays on carbon cloth for a high-performance flexible all-solid-state electrochemical capacitor. *Journal of Materials Chemistry A* **2014,** *2* (5), 1448-1457.
68. Sathiya, M.; Prakash, A.; Ramesha, K.; Tarascon, J.M.; Shukla, A., V_2O_5-anchored carbon nanotubes for enhanced electrochemical energy storage. *Journal of the American Chemical Society* **2011,** *133* (40), 16291-16299.
69. Pusawale, S.; Deshmukh, P.; Lokhande, C., Chemical synthesis and characterization of hydrous tin oxide (SnO_2:H_2O) thin films. *Bulletin of Materials Science* **2011,** *34* (6), 1179-1183.
70. Gujar, T.; Shinde, V.; Lokhande, C.; Han, S.H., Electrosynthesis of Bi_2O_3 thin films and their use in electrochemical supercapacitors. *Journal of power sources* **2006,** *161* (2), 1479-1485.
71. Zheng, L.; Xu, Y.; Jin, D.; Xie, Y., Well-aligned molybdenum oxide nanorods on metal substrates: solution-based synthesis and their electrochemical capacitor application. *Journal of Materials Chemistry* **2010,** *20* (34), 7135-7143.
72. Xia, X.; Zeng, Z.; Li, X.; Zhang, Y.; Tu, J.; Fan, N.C.; Zhang, H.; Fan, H.J., Fabrication of metal oxide nanobranches on atomic-layer-deposited TiO_2 nanotube arrays and their application in energy storage. *Nanoscale* **2013,** *5* (13), 6040-6047.
73. Zhou, Y.K.; He, B.L.; Zhou, W.J.; Huang, J.; Li, X.H.; Wu, B.; Li, H.L., Electrochemical capacitance of well-coated single-walled carbon nanotube with polyaniline composites. *Electrochimica Acta* **2004,** *49* (2), 257-262.

74. Prasad, K.R.; Koga, K.; Miura, N., Electrochemical deposition of nanostructured indium oxide: high-performance electrode material for redox supercapacitors. *Chemistry of materials* **2004,** *16* (10), 1845-1847.
75. Kalaji, M.; Murphy, P.; Williams, G., The study of conducting polymers for use as redox supercapacitors. *Synthetic metals* **1999,** *102* (1-3), 1360-1361.
76. Sharma, P.; Bhatti, T., A review on electrochemical double-layer capacitors. *Energy conversion and management* **2010,** *51* (12), 2901-2912.
77. Sivakkumar, S.; Saraswathi, R., Performance evaluation of poly(N-methylaniline) and polyisothianaphthene in charge-storage devices. *Journal of power sources* **2004,** *137* (2), 322-328.
78. Sharma, R.; Rastogi, A.; Desu, S., Manganese oxide embedded polypyrrole nanocomposites for electrochemical supercapacitor. *Electrochimica Acta* **2008,** *53* (26), 7690-7695.
79. Zhu, Z.Z.; Wang, G.C.; Sun, M.Q.; Li, X.W.; Li, C.Z., Fabrication and electrochemical characterization of polyaniline nanorods modified with sulfonated carbon nanotubes for supercapacitor applications. *Electrochimica Acta* **2011,** *56* (3), 1366-1372.
80. Naudin, É.; El Mehdi, N.; Soucy, C.; Breau, L.; Bélanger, D., Poly(3-arylthiophenes): syntheses of monomers and spectroscopic and electrochemical characterization of the corresponding polymers. *Chemistry of materials* **2001,** *13* (2), 634-642.
81. Wang, Y.G.; Li, H.Q.; Xia, Y.Y., Ordered whiskerlike polyaniline grown on the surface of mesoporous carbon and its electrochemical capacitance performance. *Advanced materials* **2006,** *18* (19), 2619-2623.
82. Xu, J.; Wang, K.; Zu, S.Z.; Han, B.H.; Wei, Z., Hierarchical nanocomposites of polyaniline nanowire arrays on graphene oxide sheets with synergistic effect for energy storage. *ACS nano* **2010,** *4* (9), 5019-5026.
83. A. Alagarasi. Introduction to Nanomaterial. **2011**, Retrieved from https://nccr.iitm.ac.in/2011.pdf.
84. Liu, R.; Duay, J.; Lee, S.B., Heterogeneous nanostructured electrode materials for electrochemical energy storage. Chemical Communications, **2011**, *47*(5), 1384-1404.
85. Lewandowski, A.; Galiński, M., Carbon-ionic liquid double-layer capacitors. *Journal of Physics and Chemistry of Solids* **2004,** *65* (2-3), 281-286.
86. Fei, H.; Yang, C.; Bao, H.; Wang, G., Flexible all-solid-state supercapacitors based on graphene/carbon black nanoparticle film electrodes and cross-linked poly(vinyl alcohol)-H_2SO_4 porous gel electrolytes. *Journal of Power Sources* **2014,** *266*, 488-495.
87. Wang, Y.; Song, Y.; Xia, Y., Electrochemical capacitors: mechanism, materials, systems, characterization and applications. *Chemical Society Reviews* **2016,** *45* (21), 5925-5950.

88. Brousse, T.; Toupin, M.; Belanger, D., A hybrid activated carbon-manganese dioxide capacitor using a mild aqueous electrolyte. *Journal of the Electrochemical Society* **2004,** *151* (4), A614-A622.
89. Ma, F.X.; Yu, L.; Xu, C.Y.; Lou, X.W.D., Self-supported formation of hierarchical $NiCo_2O_4$ tetragonal microtubes with enhanced electrochemical properties. *Energy & Environmental Science* **2016,** *9* (3), 862-866.
90. Yu, L.; Guan, B.; Xiao, W.; Lou, X.W., Formation of yolk-shelled Ni-Co mixed oxide nanoprisms with enhanced electrochemical performance for hybrid supercapacitors and lithium ion batteries. *Advanced Energy Materials* **2015,** *5* (21), 1500981.
91. Yu, X.Y.; Yu, L.; Lou, X.W., Metal sulfide hollow nanostructures for electrochemical energy storage. *Advanced Energy Materials* **2016,** *6* (3), 1501333.

Chapter 2 Synthesis and Electrochemical Properties of CoAl, NiAl, CoFe and NiFe Layered Double Hydroxide Films

2.1 Introduction

Worsening depletion of energy resource and global warming have stimulated intense research on energy storage and conversion from alternative energy sources. Supercapacitors (also known as electrochemical capacitors), as promising energy storage devices, have attracted considerable attention due to their fast charge-discharge capability, high power density and long cycle life [1-3]. Depending on different charge storage mechanism, supercapacitors can be classified into pseudocapacitors and electrical double layer capacitors (EDLCs) [4]. Compared to EDLCs, pseudocapacitors have the potential to achieve high specific capacitances and high energy storage, and the research on pseudocapacitors has gradually become a hot research area of supercapacitor in recent years [5].

As well know, the electrochemical activity of electrode materials plays the key factor in determining its performance of supercapacitors. The electrode materials of supercapacitors. mainly include transition metal oxides/hydroxides, carbon-based materials and conductive polymers at this stage [6]. Transition metal including layered double hydroxides (LDHs), also called anionic clays, have a general molecular formula of $M^{2+}_{1-x}M^{3+}_{x}(OH)_2(A^{n-})_{x/n}\cdot mH_2O$, where M^{2+} and M^{3+} are divalent and trivalent [7]. Generally, Mg, Co, Zn and Al are used divalent and trivalent metal cations, which can be replaced by some transition metal. The unique hydrotalcite-like space structure of LDH not only makes it have thermal stability and structural controllability, but also provides large active specific surface area for redox reaction. Moreover, the interlayer variable valence anions can also provide a large number of electrochemical active sites to produce high capacitance [8]. Based on it, LDHs may be ideal electrode materials for pseudocapacitors because of their high surface areas, high redox activity, low cost and environmentally friendly nature [9-10]. Previously, the powder LDHs have been reported as electrode materials of supercapacitor [11-12]. However, the powder LDHs need to be used as electrode with additives and binders [13]. They restrict the active LDHs having large active specific surface area for redox reaction and thus greatly reduce the capacitance. In this study, we synthesized CoAl, NiAl, CoFe and NiFe LDH nanosheet structures directly grown on nickel substrates by facile hydrothermal methods and examined them as binder-free electrode for supercapacitor. We investigated the differences in structural morphology and electrochemical properties of the LDHs samples.

2.2 Materials and Methods

2.2.1 Synthesis of the LDHs nanosheet structures.

The CoAl, NiAl, CoFe and NiFe LDHs were synthesized by a simple homogeneous hydrothermal method as follows. The CoAl LDH were prepared as follows (The preparation of CoFe, NiAl and NiFe were the same method). In a typical synthesis, 0.686 mmol of $Co(NO_3)_2 \cdot 6H_2O$, 0.23 mmol of $Al(NO_3)_3 \cdot 9H_2O$, 4.56 mmol of $CO(NH_2)_2$ and 2.3 mmol of NH_4F were dissolved in 40 mL distilled water. The mixed solution was stirred and then transferred into a stainless-steel autoclave with a Teflon lining. A piece of clean nickel plates (size: 50 mm × 10 mm, thickness: 0.1 mm) were immersed into the reaction solution (In this paper, Ni plates were used as substrate for LDH nanofilms growth). The autoclave was sealed and the reaction was conducted at 120 °C for 6 h in the oven. Subsequently, the autoclave was cooled to room temperature. Finally, the reaction product was taken out gently from the solution and washed with distilled water several times. The products were then dried at 60 °C for 5 h. The mass loading of CoAl LDH was about 0.7 mg/cm^2 on Ni substrate. We also obtained NiAl, CoFe and NiFe samples by the same method.

2.2.2 Structural characterization and electrochemical measurement

To analyse the structure of the sample, X-ray diffraction (XRD) patterns were measured by an X-ray diffractometer with monochromated Cu Kα radiation (RINT-2100, Rigaku). The sample chemical structures were further examined by Fourier transform infrared (FTIR) spectrometer (FTIR4100, JASCO) analysis with ATR attachment. The surface morphologies of particle shapes in the films were observed by field emission scanning electron microscopy (JSM-6500F, JEOL).

The electrochemical measurements were carried out in a three-electrode cell by electrochemical workstation (HZ 7000, Hokuto Denko) at room temperature with the 1 M KOH/KCl aqueous solution. Galvanostatic charge-discharge (GCD) and cyclic voltammetry (CV) were measured between 0 to 0.6 V, in a three-electrode cell with a SCE as the reference electrode and a Pt plate as the counter electrode.

Specific capacitance was calculated from the galvanostatic charge-discharge curves, by the equation [14]:

$$C = \frac{2i_m \int V\,dt}{(V_h^2 - V_l^2)} \qquad (1)$$

where C (F/g) represents the galvanostatic charge-discharge specific capacitance. i_m is the controlled current density. V is the measured potential, and V_h and V_l represent high and low potential values.

The specific capacitance values were calculated from the CV curves using the following equation:

$$C = \frac{1}{sm(V_h - V_l)} \int_{V_l}^{V_h} idV \qquad (2)$$

where C (F/g) represents specific capacitance from the cyclic voltammetry. The factors of s and m are scanning rate and mass of the samples, respectively. V_h and V_l mean high and low potential values, and i is the oxidation or reduction current.

2.3 Results and Discussion

2.3.1 Structural study

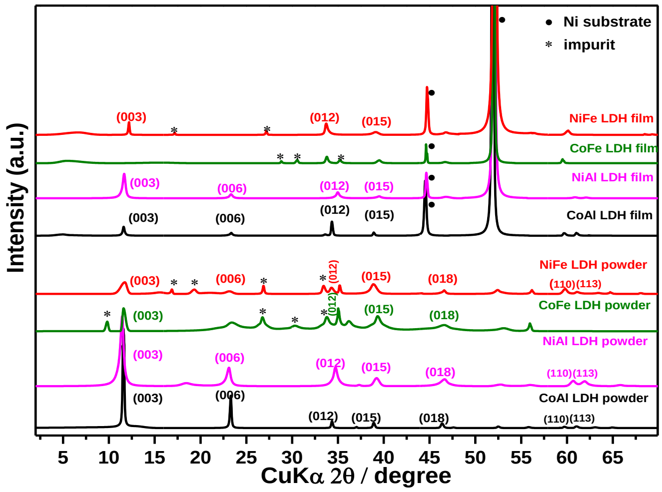

Figure 2.1. XRD patterns of the CoAl LDH powder, NiAl LDH powder, CoFe powder, NiFe LDH powder, CoAl LDH film, NiAl LDH film, CoFe LDH film and NiFe LDH film.

The crystal structures of LDHs were confirmed by X-ray diffraction. Figure 2.1 shows the XRD patterns of the LDHs powder and films. From the XRD patterns of the powder sample, it can be seen that the characteristic diffraction peaks of CoAl, NiAl and NiFe LDHs were consistent with the same position. The diffraction peaks at 2θ values of around 11.5°, 23.1°, 34.3°, 38.9°, 46.4°, 59.7° and 60.9°, corresponding to (003), (006), (012), (015), (018), (110) and (113), respectively, and combination of these peaks indicate that the LDH structure has been successfully obtained $^{15-16}$. For CoAl and NiAl LDH film and powder samples, all diffraction peaks are sharp and narrow, indicating the highly crystalline nature of both types of LDHs. The X-ray diffraction pattern of NiFe LDH shows that it generates a little amount of impurities during the reaction, and characteristic peaks of layered structure can be easily found in NiFe LDH film spectra. But the XRD pattern of CoFe LDH powder shows that many impurities emerge during the reaction and no characteristic peaks of LDH have been found in the CoFe LDH film. These results show that we didn't successfully obtain CoFe LDH under this experimental condition. For CoAl and NiAl samples, compared to the powder samples, the diffraction peaks (00*l*) diminished for the thin film samples. Such difference may result from a preferential orientation of LDH crystallites on Ni substrate with their ab plane perpendicular to the Ni substrate, which can be further confirmed by the SEM observation.

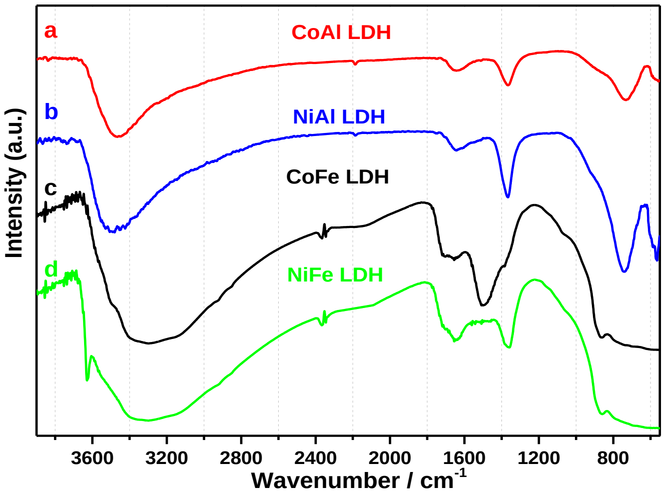

Figure 2.2. FTIR spectra of (a) CoAl LDH, (b) NiAl LDH, (c) CoFe LDH and (d) NiFe LDH.

FT-IR analysis was carried out to verify the conversion of CoAl, NiAl, CoFe and NiFe LDH in the reaction process. As shown in Figure 2.2, for CoAl, NiAl and NiFe LDHs, the characteristic absorption peaks were consistent with the same position. A strong broad band around 3400 cm^{-1} correspond to the stretching mode of metal-OH and hydrogen bonded H_2O surrounding the interlayer anion. The absorption peak at 1640 cm^{-1} could be ascribed to the H-O-H bending vibration of interlayer water molecules, while those at 1360 and 750 cm^{-1} could be assigned to the asymmetric stretching vibration of CO_3^{2-} of the C-O bond. The lower wavenumber of absorption bands at 600-800 cm^{-1} ascribed to the vibrational modes of M-O, O-M-O, and M-O-M [13, 17]. The FT-IR spectra of CoFe LDH do not contain signals associated with the interlayer carbonate anion (1360 cm^{-1}). These absorptions implied that CoFe LDH was not obtained in the reaction process. Based on this, we have not further analysed the CoFe sample in the following.

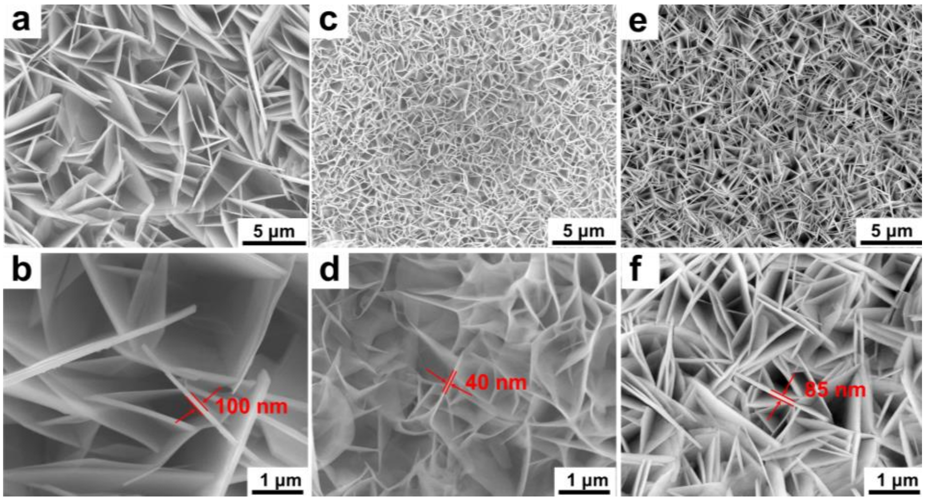

Figure 2.3. SEM micrographs of the surface of (a, b) CoAl LDH film, (c, d) NiAl LDH film (e, f) and NiFe LDH film.

Figure 2.3 shows the SEM micrographs of the surface of the CoAl, NiAl and NiFe LDH films prepared by hydrothermal treatment. SEM image shows that the LDH nanosheets in the prepared films tend to be vertically oriented and randomly distributed on the substrate surface. This result is relatively consistent with the XRD analyses. The high magnification SEM micrographs show that nanoflakes of CoAl LDH have a thickness of ~100 nm. The NiAl LDH had a randomly arrangement with a thickness of ~ 40 nm. The NiFe LDH was found to be closer arrangement with a thickness of ~85 nm. SEM micrograph shows that the LDHs films are arranged by nanosheet morphology. In addition, it can be seen from the SEM image that there is no aggregation of LDHs on the substrate surface. It shows that nickel plate is beneficial to the specific orientation growth of LDHs.

2.3.2 Electrochemical performance

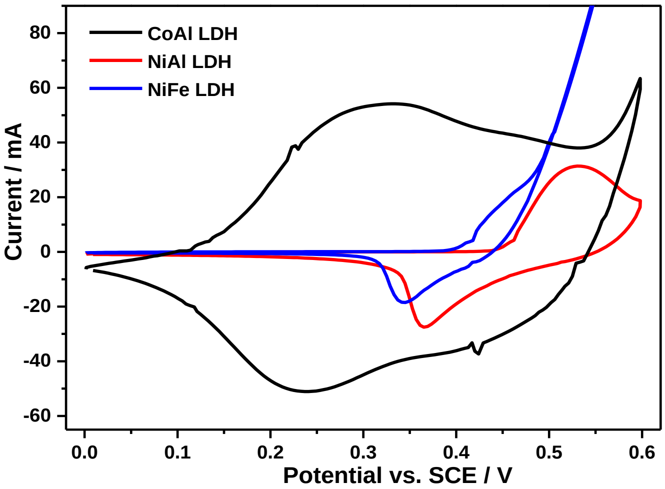

Figure 2.4. (a) CV curves of the CoAl, NiAl and NiFe LDH films at a scan rate of 20 mV/s within the potential window of 0 to 0.6 V.

Cyclic voltammetry was carried out to study the electrochemical performance of the CoAl, NiAl and NiFe LDH films. Figure 2.4 shows the cyclic voltammograms of LDH films measured in 1M KOH/KCl mixed electrolyte with a scan rate of 20 mV/s and a voltage range of 0 V to 0.6 V (vs. SCE). For the three types of LDHs, they all have a pair of redox peaks, which indicates that all LDHs have faradaic capacitance. For the CoAl LDH electrode, the CV curves possess a pair of anodic and cathodic (~0.3 and ~0.24 V) redox peaks, which were caused by the quasi-reversible faradic redox reactions. This pair may correspond to the valence transformation between $Co(OH)_2$ and CoOOH 13) and then the faradaic reaction can be easy to occur as shown in equation (3). For the NiAl LDH electrode, the CV curves possess a pair of anodic and cathodic (~0.53 and ~0.36 V) redox peaks. For the NiFe LDH electrode, the CV curves possess a pair of anodic and cathodic (~0.45 and ~0.34 V) redox peaks. They should be attributed to the valence transformation between $Ni(OH)_2$ and NiOOH [18] and then the faradaic reaction can be easy to occur as shown in equation (4).

$$Co(OH)_2 + OH^- \rightleftharpoons CoOOH + H_2O + e^- \quad (3)$$

$$Ni(OH)_2 + OH^- \rightleftharpoons NiOOH + H_2O + e^- \quad (4)$$

In the three types of LDHs, the potential difference of the CoAl LDH between the cathodic and the anodic peak is minimum, indicating that the electrochemical oxidation reaction has the best reversibility [19]. The specific capacitance of CoAl, NiAl and NiFe LDH were calculated to be 520, 159 and 71 F/g, respectively. These results apparently indicated that CoAl LDH has the best reversibility and the highest capacitance among the three types of LDHs. Then we tested the cycle stability of CoAl LDH sample.

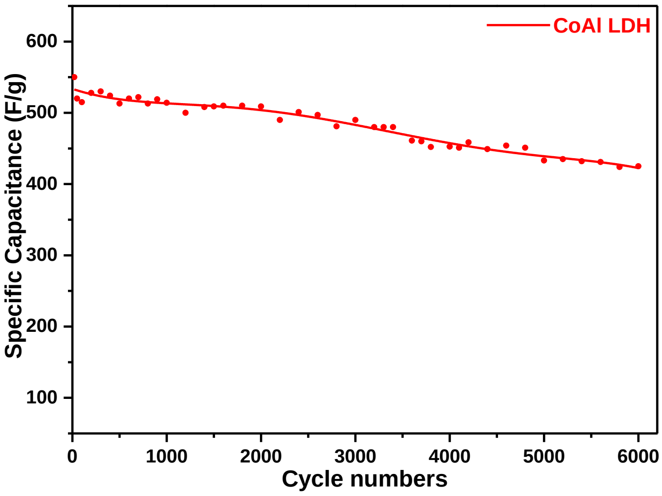

Figure 2.5. Cycling stability of the CoAl LDH. (Current density 10 A/g).

The cycling performance is one of the most important indexes in the practical use of supercapacitor. The long-term stability of CoAl LDH electrode was carried out at a current density of 10 A/g using galvanostatic charge-discharge techniques. Figure 2.5 shows cycling stability of the CoAl LDH. After 6000 times cycle test, the specific capacitance remained at 425 F/g and retained 77.3% of the initial value, indicating that the CoAl LDH nanosheets had relatively good cycling stability. With the increase in the cycle numbers, the specific capacitance of LDH decreases due to the destruction of the layered structure. In order to better understand the results, then we studied the surface morphology of CoAl LDH obtained by 6000 cycles.

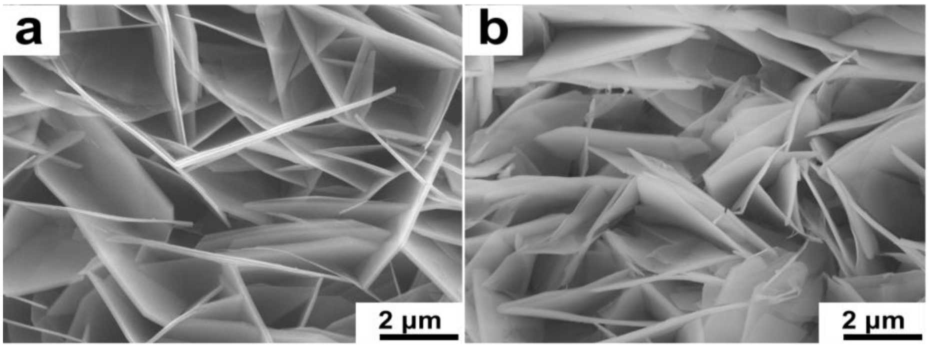

Figure 2.6. SEM micrograph of (a) pristine CoAl LDH (b) CoAl LDH obtained by 6000 cycles galvanostatic charge-discharge test.

The morphology of CoAl LDH was also observed by SEM after 6000 cycles galvanostatic charge-discharge test. Figure 2.6 shows SEM micrograph of CoAl LDH (a, b) obtained by 6000 cycles galvanostatic charge-discharge test. Compared with the pristine CoAl LDH vertically arranged on the substrate (Figure 2.6a), the micrographs indicate that the nanosheets of CoAl LDH seem to have a slant angle to substrate after 6000 cycles (Figure 2.6b). It may be responsible for the specific capacitance of LDH decreased. In addition, it can be seen from the SEM micrograph that the plate-like structure of LDH has been remained intact and no collapse occurred after 6000 cycles. This good mechanical stability maybe a direct answer for the good cycling stability.

2.4 Conclusion

In this work, we successfully synthesized CoAl LDH, NiAl LDH and NiFe LDH nanosheet structures directly grown on Ni substrates by facile hydrothermal methods. Under identical experimental conditions, CoFe LDH cannot be obtained. Although the samples have hydrotalcite structure, due to their different morphology and composition, the electrochemical properties of the LDHs have significant differences. The CoAl LDH has the best reversibility and the highest capacitance (520 F/g) among the three types of LDHs. In addition, CoAl LDH also has a good cycling stability with the specific capacitance remained at 425 F/g and retained 77.3% of the high value after 6000 cycles at a current density 10 A/g. The good cycling stability was possibly related with the stable plate-like nanosheets structure demonstrated by SEM analysis, which make it promising candidates for practical application as supercapacitor electrode materials.

Reference

1. Bae, J.; Song, M.K.; Park, Y.J.; Kim, J.M.; Liu, M.; Wang, Z.L., Fiber supercapacitors made of nanowire-fiber hybrid structures for wearable/flexible energy storage. *Angewandte Chemie International Edition* **2011,** *50* (7), 1683-1687.
2. Lu, X.; Wang, G.; Zhai, T.; Yu, M.; Xie, S.; Ling, Y.; Liang, C.; Tong, Y.; Li, Y., Stabilized TiN nanowire arrays for high-performance and flexible supercapacitors. *Nano letters* **2012,** *12* (10), 5376-5381.
3. Peng, L.; Peng, X.; Liu, B.; Wu, C.; Xie, Y.; Yu, G., Ultrathin two-dimensional MnO_2/graphene hybrid nanostructures for high-performance, flexible planar supercapacitors. *Nano letters* **2013,** *13* (5), 2151-2157.
4. Wang, G.; Zhang, L.; Zhang, J., A review of electrode materials for electrochemical supercapacitors. *Chemical Society Reviews* **2012,** *41* (2), 797-828.
5. Wang, H.; Casalongue, H.S.; Liang, Y.; Dai, H., $Ni(OH)_2$ nanoplates grown on graphene as advanced electrochemical pseudocapacitor materials. *Journal of the American Chemical Society* **2010,** *132* (21), 7472-7477.
6. Zhang, Y.; Feng, H.; Wu, X.; Wang, L.; Zhang, A.; Xia, T.; Dong, H.; Li, X.; Zhang, L., Progress of electrochemical capacitor electrode materials: A review. *International journal of hydrogen energy* **2009,** *34* (11), 4889-4899.
7. Cavani, F.; Trifiro, F.; Vaccari, A., Hydrotalcite-type anionic clays: Preparation, properties and applications. *Catalysis today* **1991,** *11* (2), 173-301.
8. Yang, Q.; Lu, Z.; Liu, J.; Lei, X.; Chang, Z.; Luo, L.; Sun, X., Metal oxide and hydroxide nanoarrays: Hydrothermal synthesis and applications as supercapacitors and nanocatalysts. *Progress in Natural Science: Materials International* **2013,** *23* (4), 351-366.
9. Abushrenta, N.; Wu, X.; Wang, J.; Liu, J.; Sun, X., Hierarchical Co-based porous layered double hydroxide arrays derived via alkali etching for high-performance supercapacitors. *Scientific reports* **2015,** *5*, 13082.
10. Huang, J.; Lei, T.; Wei, X.; Liu, X.; Liu, T.; Cao, D.; Yin, J.; Wang, G., Effect of Al-doped β-$Ni(OH)_2$ nanosheets on electrochemical behaviors for high performance supercapacitor application. *Journal of Power Sources* **2013,** *232*, 370-375.
11. Cao, F.; Pan, G.; Tang, P.; Chen, H., Hydrothermal-synthesized $Co(OH)_2$ nanocone arrays for supercapacitor application. *Journal of Power Sources* **2012,** *216*, 395-399.
12. Turco, M.; Bagnasco, G.; Costantino, U.; Marmottini, F.; Montanari, T.; Ramis, G.; Busca, G., Production of hydrogen from oxidative steam reforming of methanol: I. Preparation and characterization of $Cu/ZnO/Al_2O_3$ catalysts from a hydrotalcite-like LDH precursor. *Journal of catalysis* **2004,** *228* (1), 43-55.

13. Pan, G.X.; Xia, X.H.; Luo, J.S.; Cao, F.; Yang, Z.H.; Fan, H.J., Preparation of CoAl layered double hydroxide nanoflake arrays and their high supercapacitance performance. *Applied Clay Science* **2014,** *102*, 28-32.
14. Mai, L.Q.; Minhas-Khan, A.; Tian, X.; Hercule, K.M.; Zhao, Y.L.; Lin, X.; Xu, X., Synergistic interaction between redox-active electrolyte and binder-free functionalized carbon for ultrahigh supercapacitor performance. *Nature communications* **2013,** *4*, 2923.
15. Han, J.B.; Lu, J.; Wei, M.; Wang, Z.L.; Duan, X., Heterogeneous ultrathin films fabricated by alternate assembly of exfoliated layered double hydroxides and polyanion. *Chemical Communications* **2008,** (41), 5188-5190.
16. Rudolf, C.; Dragoi, B.; Ungureanu, A.; Chirieac, A.; Royer, S.; Nastro, A.; Dumitriu, E., NiAl and CoAl materials derived from takovite-like LDHs and related structures as efficient chemoselective hydrogenation catalysts. *Catalysis Science & Technology* **2014,** *4* (1), 179-189.
17. Li, H.; Su, X.; Bai, C.; Xu, Y.; Pei, Z.; Sun, S., Detection of carbon dioxide with a novel HPTS/NiFe-LDH nanocomposite. *Sensors and Actuators B: Chemical* **2016,** *225*, 109-114.
18. Zhang, C.; Shao, M.; Zhou, L.; Li, Z.; Xiao, K.; Wei, M., Hierarchical NiFe layered double hydroxide hollow microspheres with highly-efficient behavior toward oxygen evolution reaction. *ACS applied materials & interfaces* **2016,** *8* (49), 33697-33703.
19. He, F.; Hu, Z.; Liu, K.; Guo, H.; Zhang, S.; Liu, H.; Xie, Q., Facile fabrication of GNS/NiCoAl-LDH composite as an advanced electrode material for high-performance supercapacitors. *Journal of Solid State Electrochemistry* **2015,** *19* (2), 607-617.

Chapter 3 Enhanced Supercapacitor Performance Based on CoAl LDH-PANI Hybrid Electrodes by Hydrothermal-Electrodeposition Technology

3.1 Introduction

Supercapacitors (also known as electrochemical capacitors), as promising energy storage devices, have excellent electrochemical properties such as fast charge-discharge capability, high power density, and long cycle life [1-3]. Pseudocapacitors (also called Faradaic capacitors) represent an appealing type of supercapacitors, which have the potential to achieve high specific capacitance and high energy storage resulting from the active electrode materials and reversible redox reactions [4-6]. The research on pseudocapacitors has therefore drawn increasing attention in recent years [7]. In the meantime, the energy stored in the supercapacitor is still relatively lower than battery and thus limiting its application in high cycle life and power density [8].

Electrode material is the most critical part of supercapacitor, and it is also a key factor in determining its performance [9]. At this stage, there are three main categories of electrode materials: transition metal oxides/hydroxides, carbon-based, and conductive polymers [10]. The transition metals, including layered double hydroxides (LDHs), are ideal electrode materials for pseudocapacitors owing to their high redox activity, structural controllability and environmentally friendly nature [11-13]. Nevertheless, the relatively poor cycling life and low electronic conductivity of the LDHs limit their practical applications. To further improve the electrochemical performance, several unique carbon hybrid materials such as activated carbon/LDHs, carbon nanotube/LDHs, graphene/LDHs, and graphene oxide/LDHs have been fabricated [14-17]. Recently, more advanced and innovative nanocomposites based on LDHs have been constructed to improve the performance of pseudocapacitive materials by creating nanostructures, such as hollow LDHs spheres, LDHs/metal hydroxides, and LDHs/conducting polymers hybrid materials [18-23]. A few studies so far have focused on LDHs/conducting polymers nanocomposites, with the aim of improving the specific capacitance and cyclic stability. Han et al. successfully prepared CoAl LDH@PEDOT nanocomposite, which exhibited excellent long-term cycling stability [19]. Whereas, its specific capacitance didn’t show a significant increase and needed to be further improved. Shao et al. prepared PPY@ LDH core-shell composite via a two-step electrosynthesis, which exhibited a high energy density and excellent cycling stability [24]. Compared to conductive polymer polypyrrole (PPY) and poly(3,4-ethylenedioxythiophene) (PEDOT), polyaniline (PANI) has broader application and becomes important research subject because of its excellent electrical conductivity, good environmental stability, high specific capacitance, ease of synthesis and redox stability [25-28]. Little is known, however, about the investigation of CoAl LDH-PANI nanocomposite. The aim of this research was consequently to study the performance of CoAl LDH-PANI nanocomposite. We deemed that the study of CoAl LDH-PANI would usefully supplement and extend the research field of LDHs/conducting polymer hybrid electrode.

Inspired by the idea that conductive polymer of PEDOT and PPY can improve the electrochemical performance of LDHs, here, we elaborately designed and fabricated CoAl LDH-PANI nanocomposites directly grown on a Ni substrate by the hydrothermal-electrodeposition route and used them a binder-free electrode for pseudocapacitor. The nanocomposite exhibited significantly improved specific capacitance, good rate performance, and cyclic stability. The synergistic effect of inner LDH and outer PANI layer was studied in detail. Hence, we also believe that this work provides a promising approach for design and fabricate LDH/PANI electrode, which can be potentially used in energy storage devices.

3.2 Materials and Methods

3.2.1 Synthesis of the CoAl LDH nanosheet structures

The CoAl LDH was synthesized by a homogeneous hydrothermal method. In a typical synthesis, $Co(NO_3)_2 \cdot 6H_2O$ (0.857 mmol), $Al(NO_3)_3 \cdot 9H_2O$ (0.286 mmol), NH_4F (2.86 mmol) and urea (5.7 mmol) were dissolved in 50 mL distilled water. The mixed solution was stirred for 30min and then transferred to an autoclave with a Teflon lining. A piece of clean nickel plate (50 mm × 10 mm × 0.1 mm) was immersed into the reaction solution. The autoclave was sealed and heated at 120 °C for 6 h, subsequently cooled to room temperature. Finally, the sample was taken out gently from the solution and washed three times with distilled water. The sample was then dried at room temperature. The load weight of CoAl LDH on the Ni substrate was measured with an analytical microbalance, and the mass loading was about 1.4 mg/cm^2.

3.2.2 Synthesis of the CoAl LDH-PANI nanocomposites

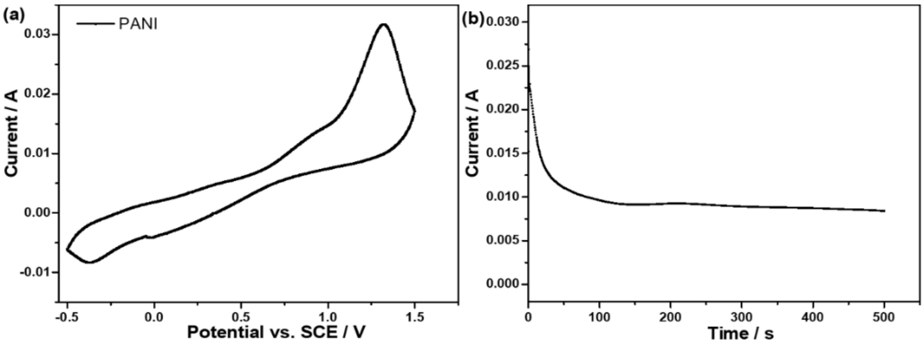

Figure 3.1. (a) CV of 0.05 M aniline in an aqueous solution (0.02 M SDS + 0.1 M $LiClO_4$) on the Ni plate at a scan rate of 20 mV/s. An anodic peak appears at ∼1.18 V, which corresponds to the

electropolymerization of aniline monomer. (b) Chronoamperograms of 0.05 M aniline in an aqueous solution (0.02 M SDS + 0.1 M $LiClO_4$) on the Ni plate at 1.18 V versus SCE.

Hybridization with polymer PANI was carried out by a potentiostatic electrodeposition technique in an aqueous medium (0.05 M aniline + 0.02 M sodium dodecyl sulfate + 0.1 M $LiClO_4$). Cyclic voltammetry experiments were performed to determine the deposition potential of PANI in a three-electrode electrochemical cell with a Ni substrate as the working electrode, a saturated calomel electrode (SCE) as the reference electrode, and a Pt plate as the counter electrode, respectively. As shown in Figure 3.1a, the optimum redox potential is selected at 1.18 V vs. SCE electrode according to the CV curve of aniline monomer. Subsequently, the Ni substrate/CoAl LDH film was used as the working electrode for the deposition of PANI at 1.18 V vs. SCE, as seen from Figure 3.1b. The deposition time varied from 50 to 600 s. After deposition, extreme caution must be taken when the as-prepared CoAl LDH-PANI electrode was washed with distilled water to prevent wash away PANI coating. And then the composite electrode was dried at room temperature. Finally, the mass loading of these deposited PANI on the Ni plate was obtained by the weight difference before and after electrochemical deposition.

3.2.3 Structural characterization, theoretical calculation and electrochemical measurement

The chemical structures of the samples were examined by Fourier transform infrared spectrometer (FTIR, FTIR4100, JASCO) analysis with ATR attachment. X-ray diffraction (XRD) patterns of the samples were obtained on an X-ray diffractometer with monochromated Cu Kα radiation (RINT-2100, Rigaku). Synchrotron X-ray diffraction (SXRD) measurements in this study were performed at SPring-8, BL02B2. The surface morphologies of the samples were characterized by field emission scanning electron microscopy (FESEM, JSM-6500F, JEOL) equipped with EDX analyzer. The surface compositions of the samples were analyzed by X-ray photoelectron spectroscopy (XPS, AXIS Ultra DLD, Kratos). The band structure and density of states (DOS) curves of the host CoAl LDH crystals were calculated by the Vienna ab-initio simulation with VASP 5.3 [29-30]. The model structure of the calculation was the LDH with Co:Al of 3:1 with intercalation of chlorine anion. The structure was optimized up to the convergence and then the band structure was calculated. These calculations were carried out by Perdew-Burke-Ernzerhof (PBE) potentials. The DOS curves for guest PANI molecules in the supporting information were calculated by DV-Xα simulation [31].

The electrochemical measurements were carried out in a three-electrode mode using the HZ 7000 electrochemical workstation (Hokuto Denko) at room temperature with the 1 M KOH/KCl aqueous solution. Cyclic voltammetry (CV) and galvanostatic charge-discharge (GCD) were measured in a three-electrode cell within the potential window between 0 to 0.56

V. The Ni substrate/sample was used as the working electrode, an SCE as the reference electrode, and a Pt plate as the counter electrode. Electrochemical impedance spectroscopy (EIS) measurements were conducted by using an AC voltage with 5 mV amplitude at 0.3 V in a frequency range from 0.01 to 100 kHz.

The specific capacitance and specific capacity values were calculated from the CV curves using the following equation (1) and (2) [32]:

$$Capacitance_{sp} = \frac{1}{sm(V_h - V_l)} \int_{V_l}^{V_h} idV \tag{1}$$

$$Capacity_{sp} = \frac{1}{3.6 \times sm} \int_{V_l}^{V_h} idV \tag{2}$$

Where C (F/g) and C (mAh/g) represent the specific capacitance and specific capacity from the CV curves; s and m are scanning rate and mass of the samples separately; V_h and V_l represent high and low potential values; i is the oxidation or reduction current. Specific capacitance and specific capacity were also calculated from the galvanostatic charge-discharge curves, by the equation (3) and (4) [33]:

$$Capacitance_{sp} = \frac{2i_m \int Vdt}{(V_h^2 - V_l^2)} \tag{3}$$

$$Capacity_{sp} = \frac{2i_m \int Vdt}{3.6 \times (V_h + V_l)} \tag{4}$$

Where C (F/g) and C (mAh/g) represent the specific capacitance and specific capacity from the GCD curves; i_m is the current density; $\int Vdt$ is the integral current area; V_h and V_l represent high and low potential values.

3.3 Results and Discussion

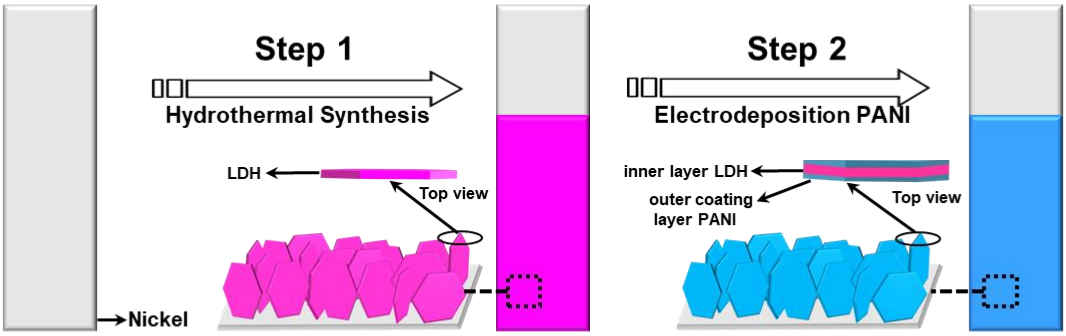

Figure 3.2. Schematic illustration of the two-step fabrication process of CoAl LDH-PANI nanosheet structures.

3.3.1 Structural study

Our approach for constructing hierarchical CoAl LDH-PANI as a binder-free electrode involves a two-step process, as schematically shown in Figure 3.2. Firstly, vertically arranged CoAl LDH nanosheets were obtained on a Ni substrate as a binder-free electrode through homogeneous hydrothermal method. Secondly, a thin layer of conductive polymer PANI was hybridized with the pristine CoAl LDH by electrodeposition technique to form the inner/outer coating layer structures.

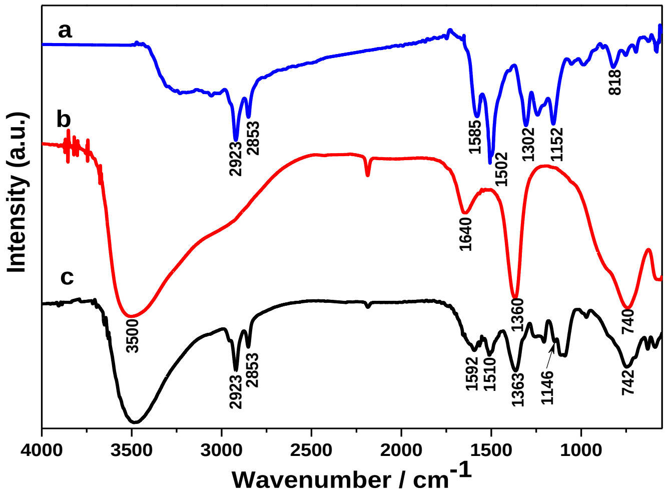

Figure 3.3. FT-IR spectra of (a) PANI, (b) CoAl LDH, and (c) CoAl LDH-PANI composite.

The molecular structures of as-prepared samples were characterized by Fourier transform infrared (FT-IR) spectroscopy. The FT-IR spectrum of pure PANI in Figure 3.3a shows the spectrum information is consistent with previously reported results [34-37]. The peaks at 2923 and 2853 cm^{-1} are separately ascribed to the asymmetric and symmetric stretching vibration of -CH_2-, which caused by sodium dodecyl sulfate (SDS) doped with PANI [38]. The main peaks at 1585 and 1502 cm^{-1} are assigned to stretching deformations of benzene and quinoid rings. Also, the bands at 1302, 1152 and 818 cm^{-1} can be attributed to C-N stretch vibration, the aromatic C-H in the plane and out of plane bending vibration of the 1,4-disubstituted benzene ring, respectively. As to the CoAl LDH in Figure 3.3b, the strong, broad band around 3500 cm^{-1} can be explained as the metal-OH stretching mode and hydrogen bond interlayer H_2O surrounding the interlayer anion [39]. The weak absorption band near 1640 cm^{-1} can be assigned to the H-O-H bending vibration of interlayer water molecules. The intense peaks at 1360 and 740 cm^{-1} can be attributed to CO_3^{2-}, owing to the asymmetric stretching vibration of the C-O bond. The lower wavenumber absorption bands at 400-700 cm^{-1} belong to the M-O, O-M-O, and M-O-M related vibrational modes of LDHs [9]. After the PANI modified CoAl LDH, several new characteristic peaks appear at 2923, 2853, 1592 and 1510 cm^{-1}; these peaks were associated with PANI-SDS, which indicated the CoAl LDH has been successfully coated by PANI.

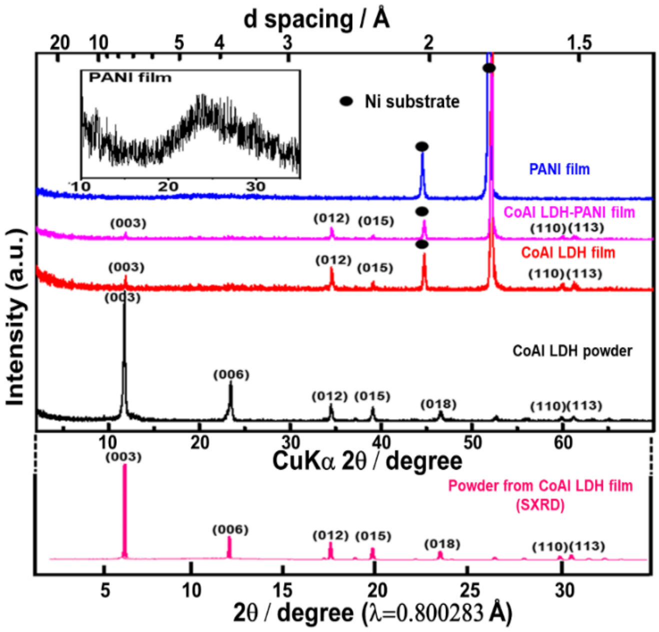

Figure 3.4. XRD patterns of CoAl LDH powder, CoAl LDH film, CoAl LDH-PANI film, PANI film, and SXRD patterns of the powder obtained from CoAl LDH film.

As shown in Figure 3.4, the crystal phase of each sample is further confirmed by X-ray diffraction (XRD). For the CoAl LDH powder, the diffraction peaks at 2θ values of around 11.5°, 23.1°, 34.3°, 38.9°, 46.4°, 59.7° and 60.9°, corresponding to (003), (006), (012), (015), (018), (110) and (113) of CoAl LDH phase (JCPDS: 51-0045), respectively [40]. Compared to the CoAl LDH powder sample, the diffraction peaks (00*l*) diminished for the thin film sample. Such a difference may result from a preferential orientation of LDH crystallites with their ab plane perpendicular to the Ni substrate, which can also be further confirmed by the FESEM observation. The existence of the LDHs on the substrate surface was also identified by SXRD. By calculating the interplanar spacing of the SXRD spectrum of CoAl LDH film, the results exhibited that the diffraction peaks of CoAl LDH film were consistent with CoAl LDH powder. It indicated that LDHs could grow well on the substrate by the hydrothermal method. Additionally, the presence of PANI in the CoAl LDH-PANI was also tested by XRD analysis. As the PANI is a long-range disordered amorphous structure, only one broad peak reflections around 2θ = 24.2° can be observed, which is caused by the emeraldine base form of PANI [41-42]. The XRD patterns of CoAl LDH-PANI film showed similar peaks to those CoAl LDH film, except that the peak intensities were decreased obviously. It could be attributed to the presence of the uniform coating of PANI on the CoAl LDH nanosheets.

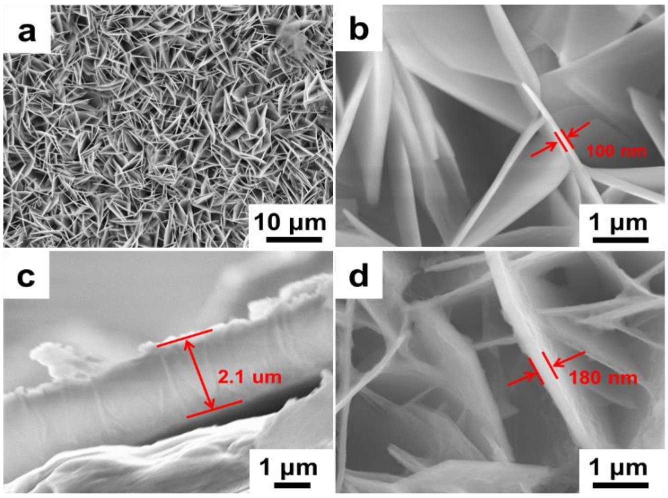

Figure 3.5. FESEM micrographs of (a, b) top-view of CoAl LDH, (c) cross-section of CoAl LDH, and (d) CoAl LDH-PANI composite.

The morphologies of CoAl LDH and CoAl LDH-PANI are investigated by field emission scanning electron microscope (FESEM), as shown in Figure 3.5. Figure 3.5a and 3.5b display top-view FESEM observations of the CoAl LDH nanosheets with a porous structure, and the nanoflakes with the thickness of ~100 nm. Figure 3.5a also displays that the CoAl LDH film can distribute uniformly on the substrate surface and consists of closely packed nanosheets with vertically arranged on the substrate in large amounts. A representative cross-sectional FESEM micrograph in Figure 3.5c shows that the CoAl LDH nanosheets have an average lateral size of ~2.1μm. As to the composite in Figure 3.5d, it reveals that the LDH nanosheets are evenly wrapping with PANI coating layer and the morphology of CoAl LDH is well retained after the deposition of PANI, with the thickness of ~180 nm.

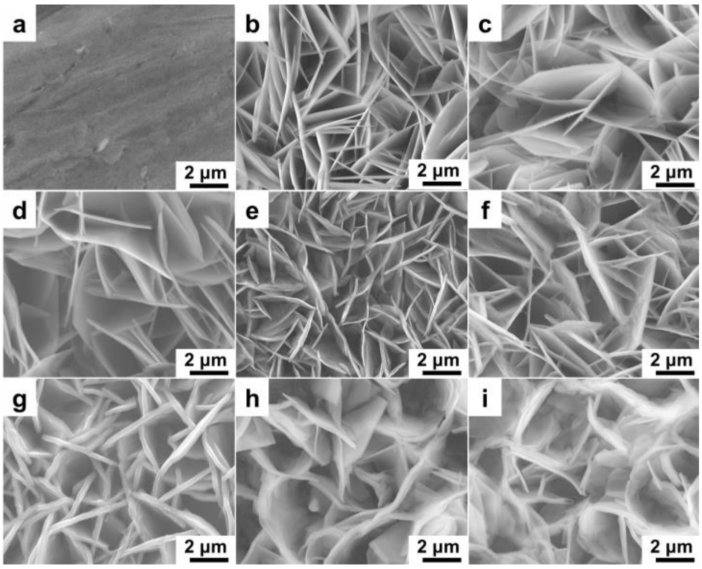

Figure 3.6. (a-i) FESEM micrographs of (a) PANI obtained by electrodeposition 600 s, (b-i) the CoAl LDH-PANI obtained by electrodeposition for various times: (b) 0 s, (c) 50 s, (d) 100 s, (e) 200 s, (f) 300 s, (g) 400 s, (h) 500 s, and (i) 600 s.

In addition, the morphologies of CoAl LDH-PANI composite obtained at different electrodeposition time were further observed by FESEM (Figure 3.6). In Figure 3.6a, the morphology of PANI film is flat and smooth wrapping on the Ni substrate surface, which implies the chronoamperometry technique is appropriate to prepare CoAl LDH hybrid PANI. From Figure 3.6b-e, with increasing the deposition time from 0 s to 200 s, the PANI coating is deposited and tends to form a thin film on the surface of LDH nanosheets, which is uniformly covered the layer of thin film at deposition 200 s. Further prolonging the deposition time from 300 to 500 s, as shown in Figure 3.6f-i, the mass of PANI coating is further increased. Also, the gaps between the layers are gradually covered, and the porous structure is gradually blocked. It is known that the suitable mesopore size distribution is beneficial for the insertion of a large number of guest ions, which can effectively increase the storage capacity. It is also one of the vital factors to consider for electrodeposited CoAl LDH-PANI electrode.

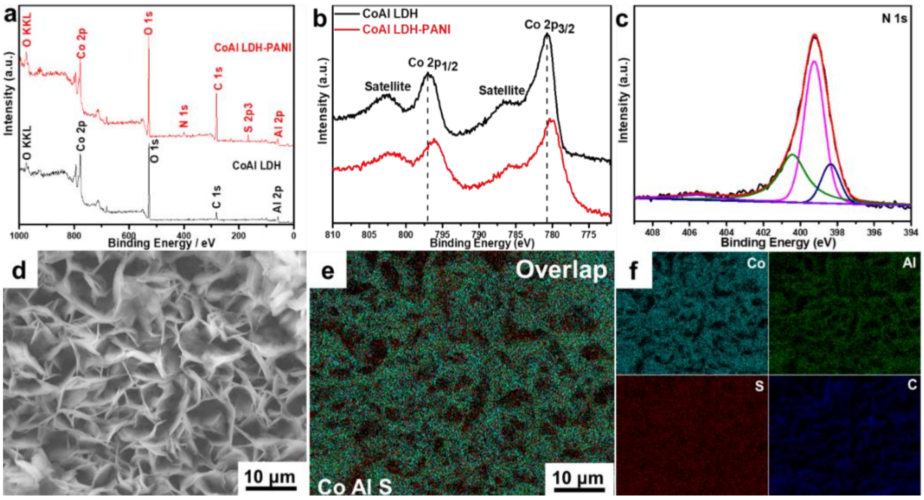

Figure 3.7. (a) The XPS full spectra and (b) Co 2p spectra of CoAl LDH and CoAl LDH-PANI. (c) N 1s spectrum of CoAl LDH-PANI. (d-f) FESEM image of CoAl LDH-PANI corresponding to the EDX elemental mapping images of Co, Al, S, and C showing uniform distribution of the elements.

In order to further study the elemental valence state and elemental distribution, X-ray photoelectron spectroscopy (XPS) and energy dispersive X-ray spectrometry (EDX) were carried out to characterize the pristine CoAl LDH and CoAl LDH-PANI samples. As illustrated in Figure 3.7a, Co 2p, O 1s, C 1s, and Al 2p peaks appear in the survey spectrum of pristine CoAl LDH, suggesting stacked CO_3^{2-}-LDH in CoAl-LDH. The full XPS spectrum of the CoAl LDH is also consistent with previously reported [43], while the presence of the N 1s and S 2p peaks in CoAl LDH-PANI spectrum indicate that CoAl LDH successfully hybrid PANI.

Furthermore, S 2p peak revealed in the spectrum of the CoAl LDH-PANI, which was ascribed to the SDS doped PANI in the CoAl LDH-PANI composites. As shown in Figure 3.7b, the Co 2p line of CoAl LDH is split into Co $2p_{1/2}$ (796.9 eV) and Co $2p_{3/2}$ (780.6 eV) peaks accompanied by satellite bands. After hybrid with PANI, the Co $2p_{3/2}$ and Co $2p_{1/2}$ main peaks slightly shift to lower energy levels (796.1 and 780.1 eV, respectively). The shift in the binding energy of Co 2p peak position provides evidence of an interaction between the inner CoAl LDH and outer PANI coating layer. The N 1s line of CoAl LDH-PANI in Figure 3.7c can be deconvoluted into three peaks at 398.50, 399.27 and 400.37, as reported previously [32]. EDX analysis in Figure 3.7d-f shows homogeneously distributed elements, Co, Al, C, and S, which implied the CoAl LDH-PANI was well distributed on the substrate surfaces. As the low energy of the characteristic X-rays in light elements, the N element has not been captured. In additional, the superposition image in Figure 3.7e reveals that S element is uniformly decorated on the nanosheets and it gives visualized evidence that PANI is evenly coated the CoAl LDH nanosheet, resulting in uniform CoAl LDH-PANI inner/outer coating nanostructure.

3.3.2 Electrochemical performance

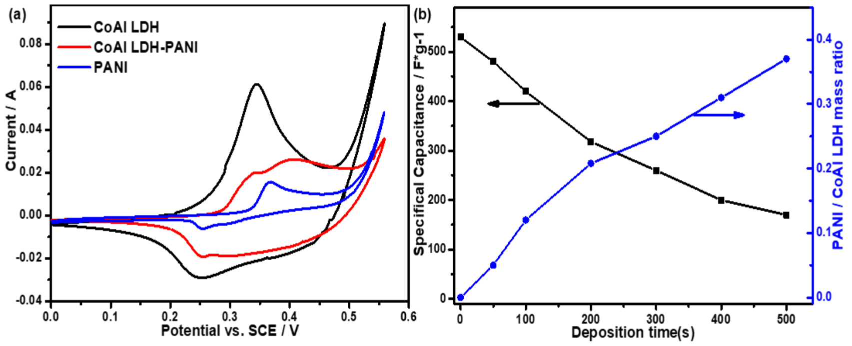

Figure 3.8. (a) CV curves of pristine PANI, CoAl LDH, and CoAl LDH-PANI composite obtained by deposition 200 s. (b) Specific capacitance values (obtained from CV measurement) and mass ratio of PANI: LDH for CoAl LDH-PANI electrode as a function of deposition time. (scan rate 20 mV/s)

Cyclic voltammetry (CV) was carried out to study the electrochemical performance of as-prepared electrodes using a three-electrode system at a scan rate of 20 mV/s. For the PANI electrode in Figure 3.8a, the CV curve possesses a pair of redox peaks (0.37/0.26 V), which has been reported previously [44]. As to the CoAl LDH electrode, the CV curve possesses a pair of redox peaks (0.34/0.25 V), which is caused by the quasi-reversible faradic redox reaction (1) [9]. The nonrectangular shape of the CV curve also indicated that faradaic reactions contributed to most of the charge storage.

$$\mathrm{Co}(OH)_2 + OH^- \leftrightarrow CoOOH + H_2O + e^- \qquad (1)$$

For the CoAl LDH-PANI electrode, the CV curve possesses characteristic redox peaks of CoAl LDH (0.34/0.25 V) and PANI (0.39/0.29 V), which revealed the composite possesses the characteristics of both constituents. Unexpectedly, the CoAl LDH-PANI exhibited a lower current than those of the CoAl LDH. For the composite, the intensity of the CV curve was weakened, and the peak potential has slightly changed, which was caused by hybrid PANI in the initial cycle. The pristine PANI electrode exhibited a very lower resulting current than those of CoAl LDH and CoAl LDH-PANI electrodes. From the data in Figure 3.8b, the specific capacitance values of CoAl LDH-PANI are a trend of decreasing with the electrodeposition time increases. Comprehensive analysis of the morphologies in Figure 3.6 and specific capacitance values in Figure 3.8b, the CoAl LDH-PANI with deposition 200 s (PANI: CoAl LDH mass ratio of 0.21:1) was chosen as the test electrode for further evaluation of electrochemical performance.

For the pristine CoAl LDH and CoAl LDH-PANI electrodes, the oxidation and reduction reactions could be explained by the following equation (1), and the theoretical specific capacitance (C_t) could be calculated by the following equation (2).

$$C_t = \frac{nF}{\Delta EM} \qquad (2)$$

Where ΔE is the potential range; M is the molecular mass of monomer; F is the Faraday constant (96485 C/mol); n is the average number of electrons transferred during the redox reaction.

The theoretical capacitance value of ~ 1834 F/g is obtained in the potential range of 0 ~ 0.56 V for $Co(OH)_2$. Therefore, we can simply calculate the electrochemically active Co (II) amount in both the pristine CoAl LDH and composite electrodes. For the CoAl LDH electrode, the practical specific capacitance value of ~ 525 F/g is calculated from Figure 3.8, and its electrochemically active Co (II) amount is about 28.6%. If we assume that there is no interaction between CoAl LDH and PANI in the composite, the specific capacitance of CoAl LDH-PANI should be the sum of specific capacitance of CoAl LDH and PANI. For the CoAl LDH-PANI (PANI: CoAl LDH mass ratio of 0.21:1), its specific capacitance can be calculated by the following equation (3).

$$C_{LDH-PANI} = C_{LDH}\frac{1}{(1+0.21)} + C_{PANI}\frac{0.21}{(1+0.21)} \qquad (3)$$

Based on the CV curves in Figure 3.8a, the practical specific capacitances of CoAl LDH-PANI and PANI are 318 and 120 F/g. After calculation by equation (3), the specific capacitance of CoAl LDH in the composite is 360 F/g. The electrochemically active Co (II) amount of CoAl LDH in composite is about 19.6%. Compare the electrochemically active Co (II) amount in the both pristine CoAl LDH and CoAl LDH-PANI electrodes, it indicates that the inner active CoAl LDH in the composite have not been fully utilized at the initial cycle.

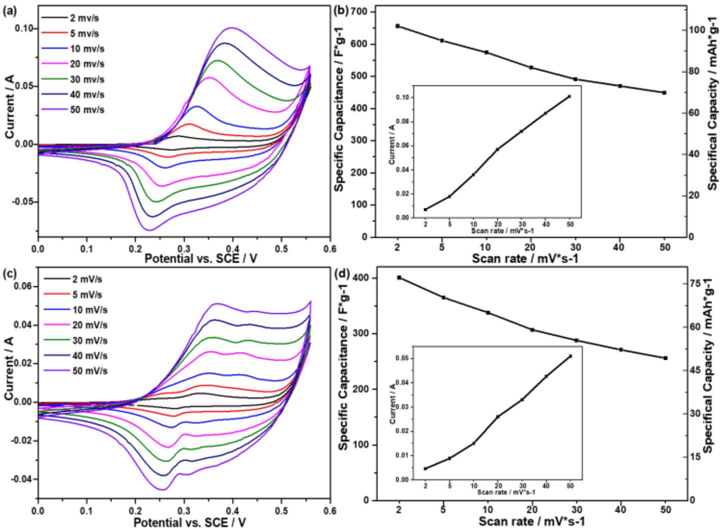

Figure 3.9. (a, c) CV curves of CoAl LDH and CoAl LDH-PANI electrodes at various current densities. (b, d) Specific capacitance and specific capacity of CoAl LDH and CoAl LDH-PANI electrodes calculated from CV curves. The insets in Figure 3.9b,d show the linearity of anodic current density with scan rate.

Figure 3.9a,c show CV curves of the pristine CoAl LDH and CoAl LDH-PANI electrodes at various scan rates. As the scan rate increases, the cathodic and anodic peaks shift to lower and higher potentials, respectively. And this shift was caused by the polarization of the electrode in highly porous LDH. As shown in the insets of Figure 3.9b,d, the almost linear relationship of the plot of anodic peak current versus the scan rate displays the surface-controlled redox reaction, which indicated the pseudocapacitance behavior of both electrodes [45]. As to the pseudocapacitance-battery behaviors of CoAl LDH and CoAl LDH-PANI, the electrochemical performances of the electrodes were assessed by determining the specific capacitance (F/g) and specific capacity (mAh/g), respectively.

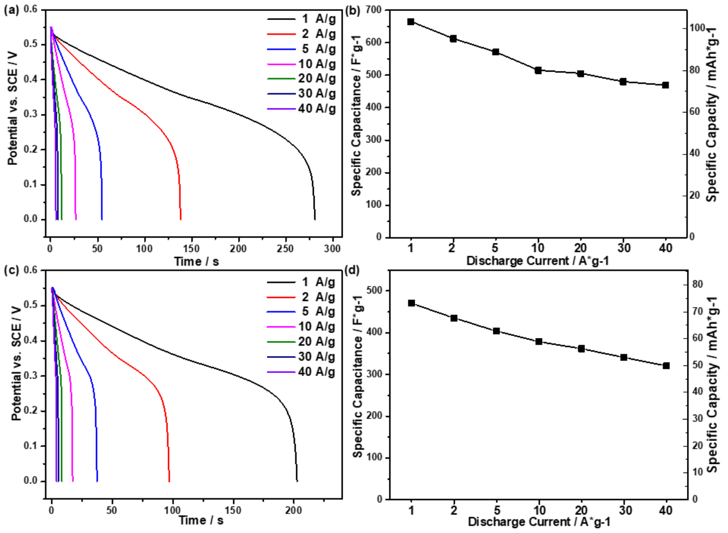

Figure 3.10. (a, c) Galvanostatic discharge curves of CoAl LDH and CoAl LDH-PANI electrodes at various current densities. (b, d) Specific capacitance and specific capacity of CoAl LDH and CoAl LDH-PANI electrodes calculated from galvanostatic discharge curves.

Rate capability is one of the significant parameters for supercapacitor. Herein, galvanostatic charge-discharge (GCD) curves were used to test the rate capability of the pristine CoAl LDH and CoAl LDH-PANI electrodes (Figure 3.10). Figure 3.10 illustrates galvanostatic discharge curves at various current densities in the initial cycle numbers. At the same current density, the specific capacitance of CoAl LDH-PANI electrode was lower than that of CoAl LDH electrode. The specific capacitance of both electrodes has a high retention rate at high current density. At a high current density of 40 A/g, the specific capacitance maintains 70.5% and 67.7% for the pristine CoAl LDH and CoAl LDH PANI electrodes, which revealed good rate capability of the as-prepared electrode. The GCD test results indicated that the composite electrode also has good rate performance.

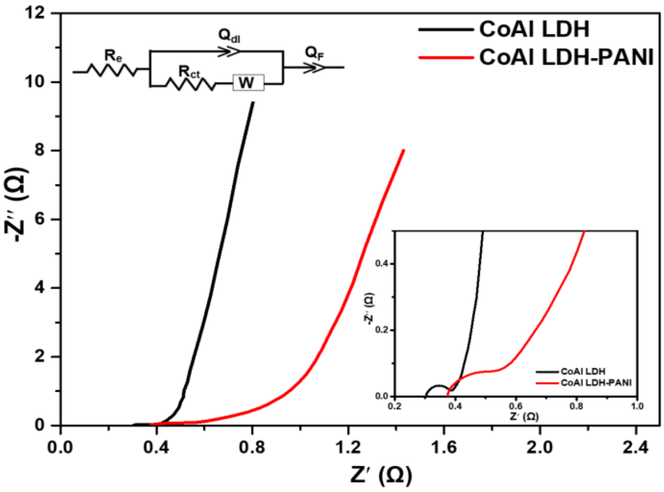

Figure 3.11. Nyquist plots of the EIS in the frequency range from 0.01 Hz to 100 kHz with an AC amplitude of 5 mV in 1 M KOH/KCl electrolyte.

Table 3.1. The R_e, R_{ct} and n parameters of electrodes obtained from the Nyquist plot fitting.

Electrode	R_e (Ω)	R_{ct} (Ω)	W (Ω/s$^{1/2}$)	n_{dl}	n_F
CoAl LDH	0.304	0.076	0.137	0.891	1
CoAl LDH-PANI	0.375	0.381	0.315	0.729	0.974

In the initial cycle, the reduced capacitance of the composite has further analyzed the reasons by the electrochemical impedance spectroscopy (EIS) tests. Figure 3.11 shows the Nyquist plots of the EIS spectra for CoAl LDH and CoAl LDH-PANI, which consist of approximate semi-circles in the high-frequency range and an inclined straight line in the low-frequency range. The Nyquist plots are analyzed by applying the equivalent circuit shown in the inset of Figure 3.11. The inset shows the equivalent circuit diagram. R_e is the equivalent series resistance, including the ionic resistance of the electrolyte, the intrinsic resistance of the substrate and electroactive material, and contact resistance at the interface between electrolyte and electrode [46]. R_{ct} is the charge-transfer resistance. Due to the porous surface of electrodes, the constant phase element (CPE) is used in the equivalent circuit. The impedance of CPE is defined as $Q = \frac{1}{T(jw)^n}$, where T and n are the frequency- independent constant and a correction factor range from -1 to 1. If n=-1, the CPE is an inductor and if n=1, CPE is a pure capacitor and if n=0, CPE is a pure resistor [47]. Q_{dl} represents the constant phase element, which is mainly attributed to the double-layer capacitance. Q_F represents the constant phase element, which is mainly attributed to the faradic pseudocapacitance. W is the Warburg resistance, which is caused by the diffusion/transport of OH^- ions within the porous structure of electrodes [48]. A summary of the CoAl LDH and CoAl LDH-PANI fitting parameters from the impedance spectra is presented in Table 3.1. In the high-frequency range, the intersecting point with the real axis represents the equivalent series resistance (R_e). In addition, the approximate semi-circle is associated with Faradic reactions, and its diameter represents the interfacial charge-transfer resistance (R_{ct}). In the low-frequency range, the slope is caused by the Warburg impedance (W), which is related to the diffusion resistance of the OH^- electrolyte ions in the electrode pores [19]. Furthermore, in the very low-frequency range (≤ 100 mHZ), the EIS spectra deviate from the idealized porous electrode model, and the slope of the straight line is larger than 45°. For the PANI-coated CoAl LDH electrode, this deviation behavior becomes more pronounced. Such behavior at very low frequency, also reported by Cooper [49] and Chamaani [50], is related to the frequency dispersion originating from the deficiency in the porous electrode structures. As shown in the inset of Figure 3.11, the value of the intersecting point with the real axis of CoAl LDH-PANI (0.375 Ω) is slightly larger than that of CoAl LDH (0.304 Ω), revealing that PANI only a small increase resistance to the composite electrode. The diameter of the approximate semi-circles of CoAl LDH-PANI is larger than CoAl LDH, and the slope of the straight line for CoAl LDH-PANI is less than CoAl LDH. It indicated that the composite electrode has a larger interfacial charge-transfer resistance and higher diffusion resistances that correspond to a reduced capacitance, compared to CoAl LDH. To put that another way, the PANI-coated CoAl LDH leads to an increase in “inactive” material (inner CoAl LDH) which is not very accessible to the OH^- electrolyte ions, and thus causes lower utilization of active material in the initial cycle. The n-value obtained from the Nyquist plot fitting is between 0.7 and 1, indicating the capacitive behavior of the CoAl LDH and CoAl LDH-PANI electrodes.

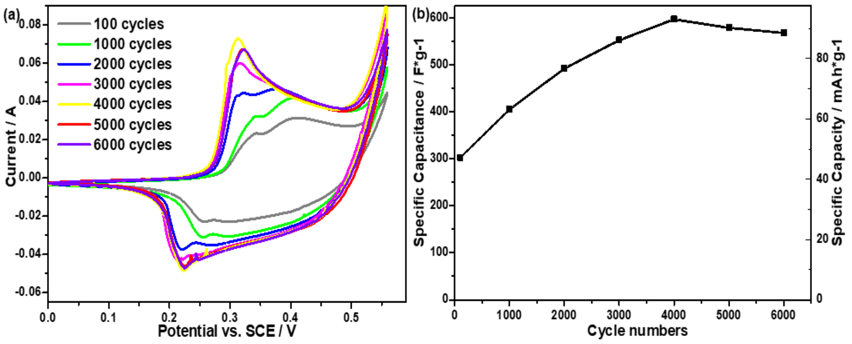

Figure 3.12. (a) CV curves of CoAl LDH-PANI electrode at different scan cycles. (b) Specific capacitance and specific capacity values (obtained from CV curves) of CoAl LDH-PANI electrode as a function of cycle numbers. (scan rate 20 mV/s)

The CV curves in Figure 3.12a exhibit the redox process of CoAl LDH-PANI electrode with cycle number from 100 to 6000 cycles. Interestingly, with the scan cycles increase, the CV curve tends to enlarge area accordingly, which indicates the specific capacitance and specific capacity increase correspondingly. As can be seen, the specific capacitances of CoAl LDH-PANI are calculated to be 308 F/g and 567 F/g after 100 and 6000 cycles. Besides, the specific capacity is also presented in Figure 3.12b. The specific capacity values of the CoAl LDH-PANI are calculated to be 47.9, 63.1, 76.6, 86.2, 92.9, 90.1 and 88.2 mAh/g as scan cycles of 100, 1000, 2000, 3000, 4000, 5000 and 6000 cycles, respectively. The CoAl LDH-PANI electrode exhibited increase current of redox peaks before 2000 cycles. The enhancement in specific capacitance could be attributed to the self-activation process of the inner CoAl LDH, which has also been supported by earlier reported [51-52]. Based on the EIS analysis, after hybrid with PANI, the inner active materials of CoAl LDH have not been fully utilized in the initial cycle. After repetitive redox process, the gradual activation of inner active points of the electrode materials exposed to the electrolyte, and hence enhanced the specific capacitance. It is also interesting to find that the current for the CoAl LDH-PANI increases continuously over 2000 cycles, with the disappearance of the PANI redox peak. It may have occurred the decomposition of polyaniline and formation of new active materials with highly electrochemically during the long scan process [53-54]. Perhaps the self-activation and degradation processes occurred simultaneously throughout the cycles. This enhanced capacitance is what we expect and will be further discussed the reasons below.

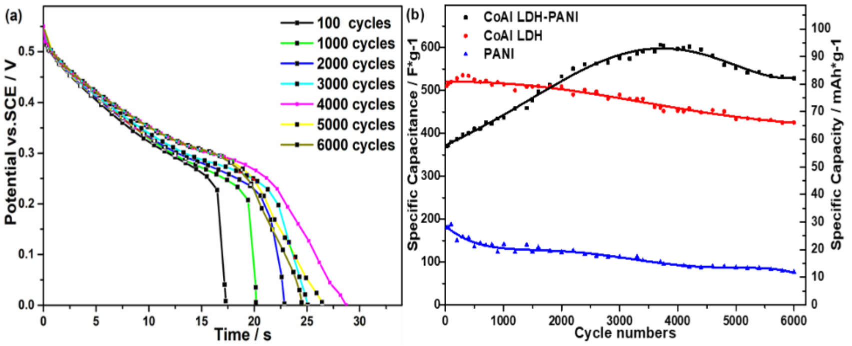

Figure 3.13. (a) Galvanostatic discharge curves of the CoAl LDH-PANI electrode at different scan cycles. (b) Cycling performance of the CoAl LDH, PANI, and CoAl LDH-PANI electrodes, respectively. (Current density 10 A/g)

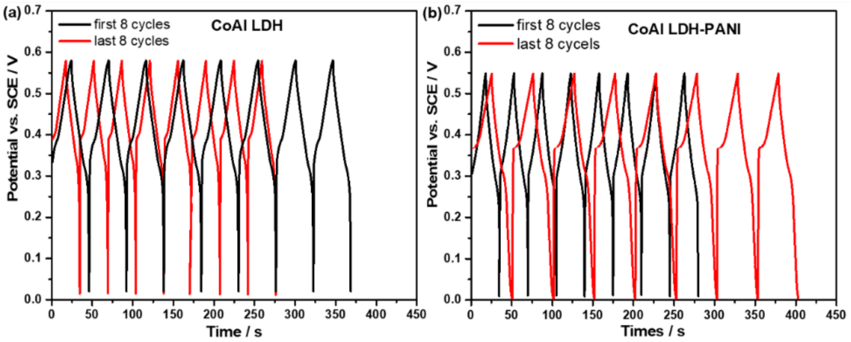

Figure 3.14. Galvanostatic charge-discharge curves of first 8 cycles and last 8 cycles for (a) CoAl LDH and (b) CoAl LDH-PANI during 6000 GCD cycles (current density of 10 A/g).

The cycling performance is one of the most critical indices in the practical use of electrochemical supercapacitors. The long-term stability of as-prepared electrodes was tested by GCD, and the results are presented in Figure 3.13. As can be seen from Figure 3.13a, the galvanostatic discharge curves of the CoAl LDH-PANI electrode are extended the time with cycle numbers from 100 to 6000 cycles, which indicate the specific capacitance rise correspondingly. For the CoAl LDH electrode, the GCD time of the last 8 cycles decreased notably than that of the first 8 cycles (Figure 3.14). However, for the CoAl LDH-PANI, the GCD time of the last 8 cycles increased greatly compared with the first 8 cycles after 6000 GCD cycles. The results of this study indicated that the advantage of CoAl LDH-PANI was the increase of specific capacitance at high cycles. For the CoAl LDH electrode in Figure 3.13b, its specific capacitance increases from 510 to 535 F/g (79.3 to 83.2 mAh/g) in the initial 400 cycles due to the self-activation process, and then continuous decline from 535 F/g to 425 F/g (83.2 to 66.1 mAh/g, 83.3% retention after 6000 cycles). For the CoAl LDH-PANI electrode, it is pleasantly surprising to find that the specific capacitance increases from 370 to 600 F/g (57.6 to 93.3 mAh/g) over 3500 cycles, and then gradually decreased from 600 to 528 F/g (93.3 to 82.1 mAh/g, 142.7% retention after 6000 cycles). The cycling stability behavior was also observed for the PANI electrode. The specific capacitance of pristine PANI electrode has a dramatic drop from 180 to 76 F/g (28 to 11.8 mAh/g, 42.2% retention after 6000 cycles), which was ascribed to PANI structures suffer from a large volumetric alternation during the charge-discharge process. Comprehensive analysis of Figure 3.12 and Figure 3.13, the enhanced specific capacitance of CoAl LDH-PANI electrode may be attributed to both the self-activation process of electrode materials and decomposition of PANI to form new active substances during the long cycle process. Nevertheless, so far, the process of polyaniline degradation to form new active substances has not been made clear yet. In order to deeply investigate the reasons, we studied this reason by using the FT-IR, FESEM and XPS methods.

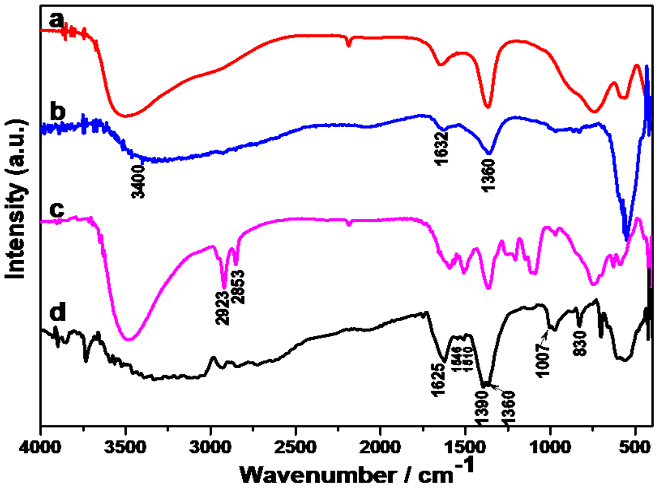

Figure 3.15. FT-IR spectra of (a) CoAl LDH obtained by pristine sample, (b) CoAl LDH obtained by 6000 GCD cycles, (c) CoAl LDH-PANI obtained by pristine sample, and (d) CoAl LDH-PANI obtained by 6000 GCD cycles.

After 6000 GCD cycles, the molecular structures of CoAl LDH and CoAl LDH-PANI samples were further characterized by FT-IR spectroscopy. What stands out in Figure 3.15 is the apparently different infrared spectrum of CoAl LDH-PANI before and after 6000 GCD cycles. For the CoAl LDH in Figure 3.15b, the intensity of the peak around 3400 cm^{-1} decreases and the peak becomes broader. The lower wavenumber absorption bands at 700-800 cm^{-1} become very weak. Combined with the analysis of Figure 3.3b, it implied that the part of CO_3^{2-} anion interlayer space exchange to OH^-. As to the CoAl LDH-PANI in Figure 3.15d, there are numerous new peaks appeared in the spectra, which indicate the oxidative degradation of PANI in alkaline solution. The peaks at 2923 and 2853 cm^{-1} disappear, which is assigned to the de-doping of SDS of PANI backbone in alkaline solutions (Possible degradation process sees the Supporting Information, Scheme S1). The release of dopant anion in the PANI backbone may cause its conductivity to decrease. Moreover, the absorption peaks of the degradation products group overlap with CoAl LDH, resulting in broader and enhanced absorption bands. The enhanced peak around 1625 cm^{-1} is caused by the H-O-H bending vibration of LDH interlayer water molecules, the stretching vibration of the terminal group C=O, and C=N stretching vibration of aromatic [55]. The weak band at 1546 cm^{-1} is assigned to the asymmetric stretching vibrations of NO_2. The band at 1510 cm^{-1} becomes very weak in the spectrum, indicating the absence of p-phenylenediamine form (N-B-N) during the degradation process. The enhanced peak around 1390 cm^{-1} may be assigned to the interactions between the asymmetric stretching vibration of the C-O bond and symmetric stretching modes of the terminal group NO_2. Herein, we speculated that the nitro group might be due to oxidizing the amino group and the imino group to form, which can be further confirmed by the XPS analysis. The bands at 1007 and 830 cm^{-1} are severally due to the C-H in-plane bending and the C-H out-of-plane bending vibrations of the 1,4-disubstituted benzene ring [37]. Considering the fact that the oxidative degradation of PANI, we may conclude that the polymer suffers oxidative degradation was ascribed by an inherent instability of PANI at high potentials.

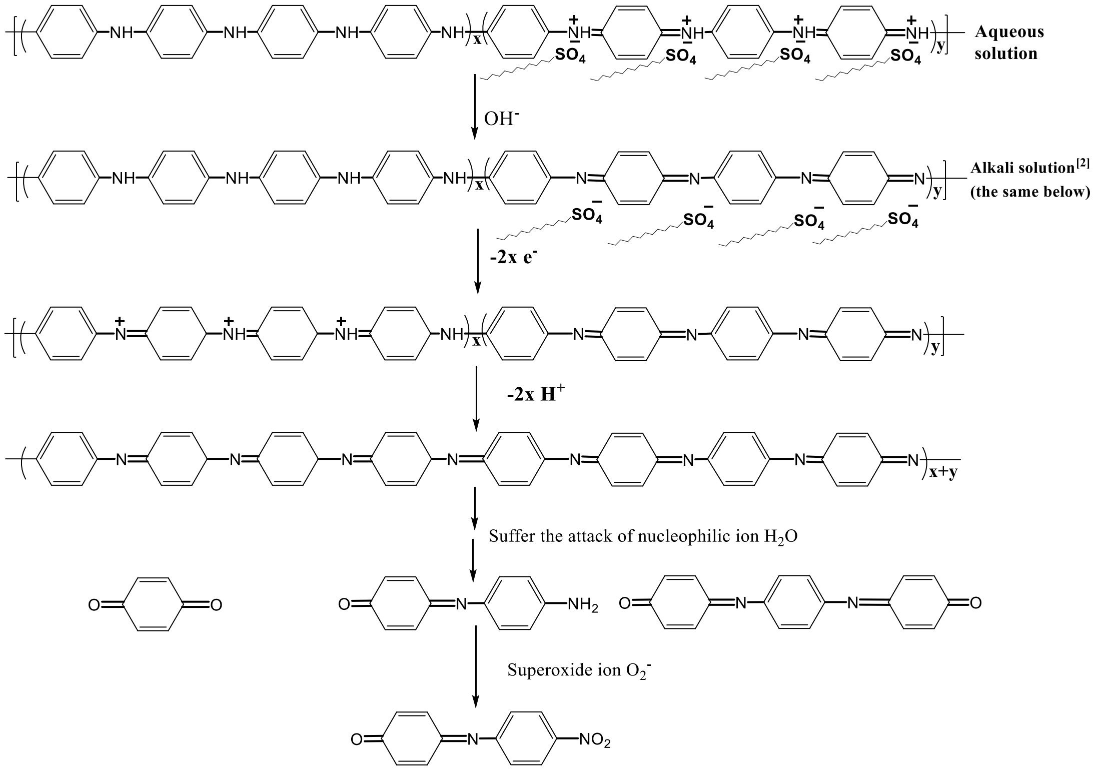

Scheme 1. Degradation of PANI during electrochemical process in the alkaline solutions.

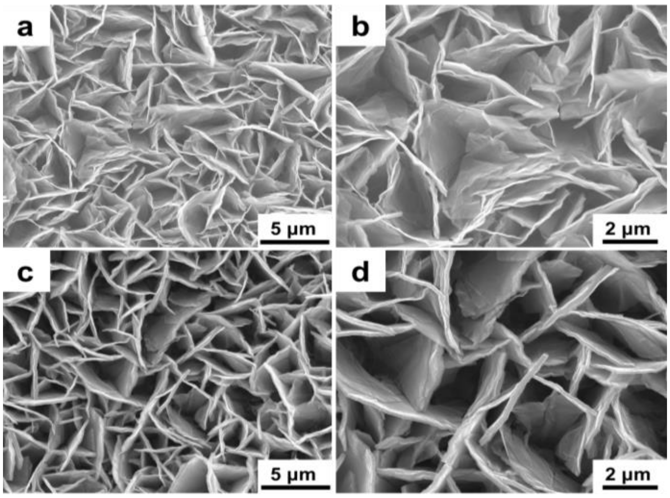

Figure 3.16. FESEM micrographs of (a, b) CoAl LDH and (c, d) CoAl LDH-PANI obtained by 6000 GCD cycles.

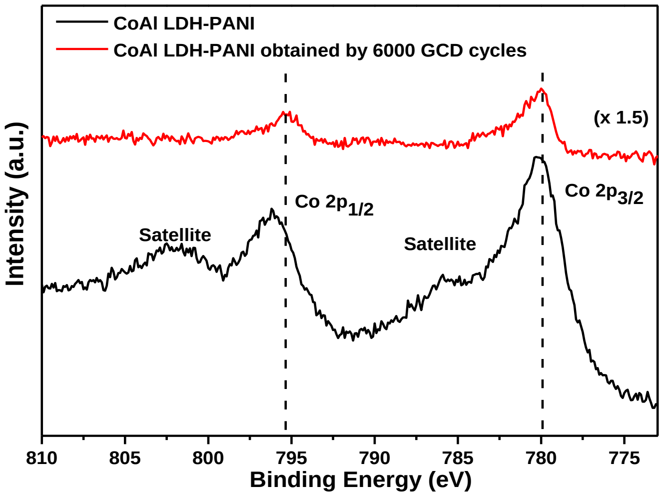

Figure 3.17. Co 2p spectra of pristine CoAl LDH-PANI and CoAl LDH-PANI obtained by 6000 GCD cycles.

The morphologies of CoAl LDH and CoAl LDH-PANI electrodes were further observed by FESEM after 6000 GCD cycles. Compared with the pristine CoAl LDH (Figure 3.5a) vertically arranged on the substrate, it can be seen from the micrographs in Figure 3.16a and 3.16b that the nanosheets of CoAl LDH seem to have a slant angle to the substrate and partial collapse after 6000 GCD cycles. As to the CoAl LDH-PANI electrode in Figure 3.16c and 3.16d, they give visible evidence that the structures were well-preserved without any nanosheets cracks and collapses occurred. As we mentioned before, for the composite, the LDH nanosheets were uniformly wrapping with PANI coating layer and covered the gaps between the layers, which might play an essential role in the prevention of the electrolyte ions from degrading the inner nanosheets. Judging from this aspect, the presence of PANI coating layer sharply enhanced the structural stability of LDH nanosheets during the redox reaction. This good structural stability may be a direct answer for the better cycling stability. Figure 3.17 shows Co 2p spectra of pristine CoAl LDH-PANI and CoAl LDH-PANI obtained by 6000 GCD cycles. After 6000 GCD cycles, the Co $2p_{3/2}$ and Co $2p_{1/2}$ main peaks slightly shifted to higher energy levels with the intensity of the Co 2p peaks and satellite bands significantly decreased. These differences indicated that part of Co^{2+} in the composite was oxidized to Co^{3+} after 6000 GCD cycles. Furthermore, after 6000 GCD tests, the crystallinity seemed to be preserved due to the morphology of nanosheet on the plate could be observed in Figure 3.16. Given the result of SEM micrograph and XPS spectrum, it indicated that crystallinity of CoAl LDH in composite after 6000 GCD cycles was partially preserved.

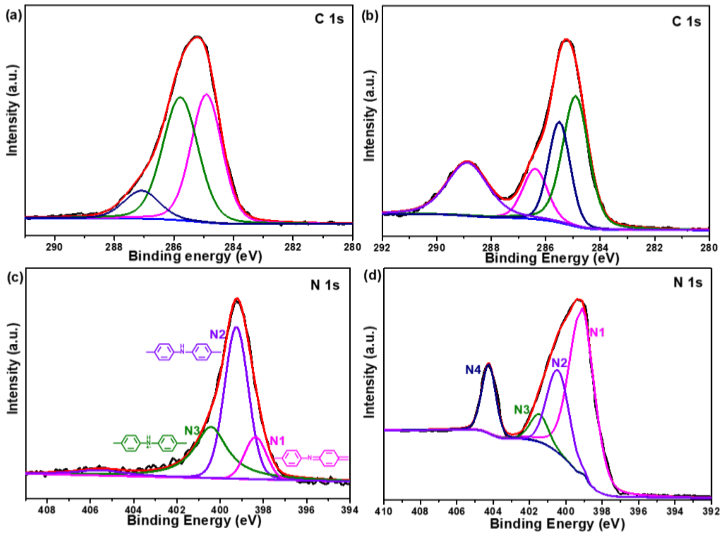

Figure 3.18. C 1s and N 1s spectra of (a, c) pristine CoAl LDH-PANI and (b, d) CoAl LDH-PANI obtained by 6000 GCD cycles.

Figure 3.18 illustrates the surface elemental C 1s and N 1s spectra of pristine CoAl LDH-PANI and CoAl LDH-PANI obtained by 6000 GCD cycles. The C 1s line of pristine CoAl LDH-PANI in Figure 3.18a can be deconvoluted in three peaks at different binding energies: 284.89 eV (C-C/C-H), 285.78 eV (C-N/C=N) and 287.12eV (C-O/C=O) [56]. The peak at 287.12 eV can be assigned to carboxylate carbon, indicating that CoAl-LDHs are partly intercalated by CO_3^{2-} anion [57]. Whereas the C 1s line of CoAl LDH-PANI in Figure 3.18b can be deconvoluted in four peaks at different binding energies: 284.91 eV (C-C/C-H), 285.52 eV (C-N/C=N), 286.39 eV (C-O) and 288.89 eV (C=O). As mentioned in Figure 3.15, most of the carbonate ions in the LDH intercalation are replaced by hydroxide ions after LDH 6000 GCD cycles. Thus the C=O functional groups might be assigned to the formation of the terminal group C=O structure with degradation products. The N 1s line of pristine CoAl LDH in Figure 3.18c can be deconvoluted into three peaks at different binding energies: 398.50 eV (-N=), 399.27 eV (-NH-) and 400.37 eV (-N$^+$H-) [44]. However, as to the CoAl LDH-PANI in Figure 3.18d, there is a new N 1s peak line appeared at 404.41eV (N4), which can be assigned to the formation of the terminal nitro group (-NO_2) with degradation products [58-59]. And the N 1s peak also has similar deconvoluted with those of pristine CoAl LDH-PANI. Furthermore, the intensity of N1 line was maximum in Figure 3.18d, which indicated the composite has a higher ratio of quinoid groups. The above analysis results are also in accord with the FTIR analysis in Figure 3.15. The degradation products may be the critical factor for achieving higher electrochemical activity in electrolyte to increase the capacitance. Generally, hydroquinone can be oxidized to benzoquinone at 0.7 V versus SHE in acidic condition. This potential will decrease to around -0.1 V in the alkaline condition from Lewis equation. For the C=O group in our sample, the quinone ring is bonded with imino group which shows electron attraction by mesomeric (-M) effect. The imino group is connected with nitrophenol having the electron attractive property. These electron attractive groups will tend to increase the potential of the redox reaction between C=O and C-OH. Therefore, the redox process may occur within the potential window between 0 to 0.56 V versus SCE and contribute to increasing the capacitance. Furthermore, the degradation products of the terminal nitro group may also be closely related to achieving high electrochemical activity. Given the results of FT-IR and XPS analysis, it was also worthwhile mentioning that the degradation behavior of PANI was a difference between the alkaline and acid electrolyte solutions [60-61]. We were also aware that our research might also have the limitation. It is generally known that the random chain scission of polymer molecular chains is relatively complicated during the degradation of the PANI. Herein, we have only confirmed the possible terminal group structures generated during the degradation process. Regrettably, however, we were unable to definitely give the specific molecular formula of the new active materials.

3.3.3 Band structure and synergistic mechanism

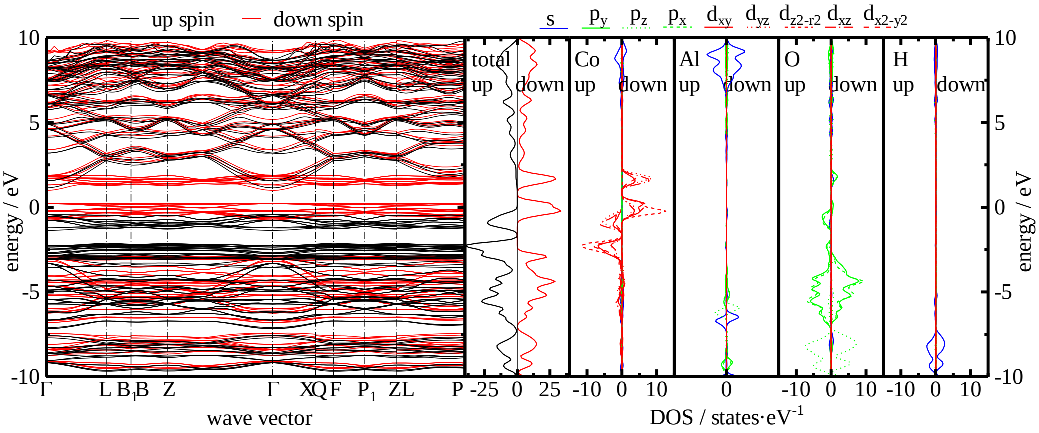

Figure 3.19. Band structure, total DOS, and partial DOS for each element of CoAl LDH.

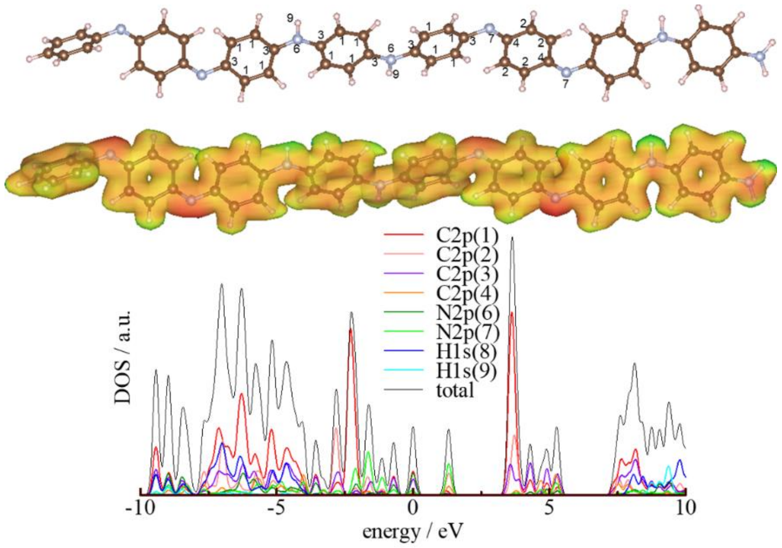

Figure 3.20. Charge density model and DOS of PANI molecules.

Up to this point, a fundamental understanding of the synergistic mechanism of inner CoAl LDH and outer PANI layer is still missing. Here, we tried to reveal the synergistic mechanism from the perspective of the band structure. Figure 3.19 shows the band dispersion, density of states (DOS) of a total, Co, Al, and O calculated by ab-initio simulation. For these curves, the Fermi level is at 0 eV. From the band dispersion curve, Fermi level was slightly lower than the conduction band minimum (CBM), which was composed of down spin. Actually, CoAl LDH shows a slight conductive property. From the partial DOS, only the 3d electrons in Co was split between up and down spin nearby the Fermi level by exchange splitting due to delocalization of d orbital. In both spins, d orbitals are a bimodal shape with separation of around 1.9 eV, and components of each band are same as follows. The lower band is composed of large $d_{z2\text{-}r2}$ orbital and small amounts of $d_{x2\text{-}y2}$, d_{xy}, d_{yz}, and d_{xz} orbitals. In the higher band, large d_{yz} and d_{xz} orbitals and small $d_{x2\text{-}y2}$ and d_{xy} orbitals exist. These components implied that these separations were provided from degeneracy by crystal field splitting, focusing on the same direction of z-axis between electron orbital crystal structure. Since CoO_6 octahedra are connected with edge sharing, d orbitals may be overlapped and provide electron conductivity with layer direction. On the other hand, the band with lower energy composed of O 2p is also split to p_z and the others. The p_z orbital binds with a 1s electron in a proton. There is a small energy gap of 0.25 eV at around 7-8 eV. Therefore, the electron should be hopped when the redox reaction (1) occurs. In the case of CoAl-LDH with PANI hybrid, charge transfer may occur between LDH and PANI. Figure 3.20 shows DOS of PANI calculated by Discrete Variational X (DV-X). From these curves, orbital of N 2p distributes widely within the band in the range from -10 to -3 eV for amino and from -8 to 0 eV for imino group, respectively. Such wideband structure may result in easy hopping for the charge transfer due to overlapping energy with both O 2p_x, p_y and p_z in the LDH structure.

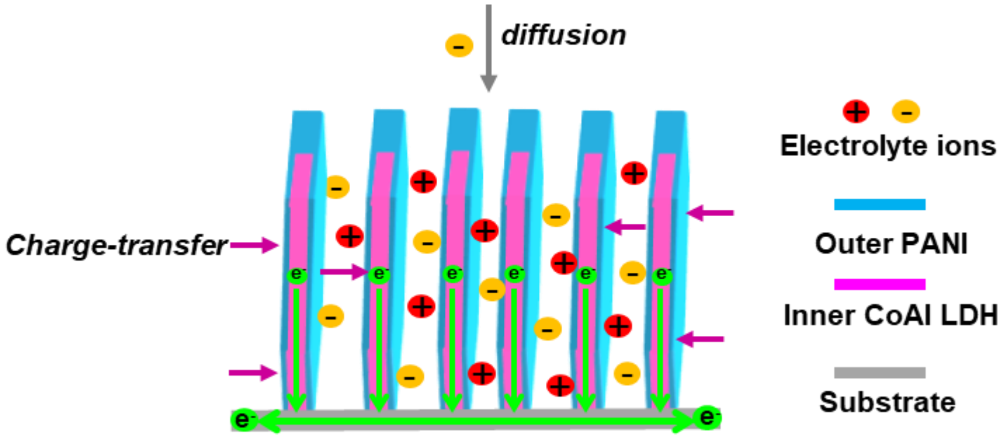

Figure 3.21. A schematic cross section illustration of electrolyte diffusion paths in CoAl LDH-PANI nanosheets.

Based on the above results, the high specific capacitance and excellent cycling stability of CoAl LDH-PANI composite should be related to its well-designed nanosheets structure and synergistic effect between the inner LDH layer and outer PANI coating layer. They can be explained by the following reasons. (1) The CoAl LDH nanosheet can directly grow on the substrate with its ab-faces perpendicular to the substrate without any additive, which revealed a lower contact resistance and large specific surface area. As shown in Figure 3.21, the porous structures of CoAl LDH inner and thin PANI outer resulted in high utilization of active materials and short ionic diffusion path. (2) The space between CoAl LDH nanosheets is large enough to buffer the large volumetric swelling/shrinkage of PANI during charging/discharging process; while stable PANI shell also acts as a protection layer to preserve the CoAl LDH nanosheets from direct exposure to the corrosive environment. Especially Al can be dissolved in a strong alkaline solution. In this sense, the composite design that couple CoAl LDH with PANI can effectively make up the disadvantages of cycling stability of each component. (3) The enhancement in specific capacitance can be attributed to two aspects. The first aspect is due to the self-activation process of composites. At the initial cycle, active materials are not fully utilized, and it can delay the increase of the capacitance. After repeated charge-discharge process, the continuous activation of redox components is fully exposed to the electrolyte and they can greatly increase the capacitance by synergistic effect. The other aspect is the PANI can further maximize the specific capacitance of the whole electrode due to the decomposition of PANI to form new materials with highly electrochemically, and the improvement of ion diffusion rose the specific capacitance.

3.4. Conclusion

In summary, we have successfully used in hydrothermal-electrodeposition method to prepare a novel inner/outer layer structural CoAl LDH-PANI nanocomposite in which the CoAl LDH nanofilms are well grown on Ni surface and the inner CoAl LDH is decorated by outer PANI layer. The hybrid architecture CoAl LDH-PANI exhibited greatly enhanced specific capacitance and cyclic stability (528 F/g at a current density of 10 A/g, 142.7% retention after 6000 cycles) and was superior to the non-decorated CoAl LDH (425 F/g at a current density of 10 A/g, 83.3% retention after 6000 cycles). The hydrothermal-electrodeposition method for synthesis of LDH-PANI growth on Ni substrate was straightforward and controllable. Our study results indicate that the PANI can be oxidized to other products which can act in the alkaline solution to increase of the capacitance under a proper working electrode and device voltage. Future studies are required to further identify the specific molecular structures of PANI degraded active products for the enhanced electrochemical activity of the LDH-based hybrid capacitor, and they are currently underway to examine in our laboratory. The possible mechanism of synergistic effect is also proposed in a new perspective. We deem that our research will be valuable in improving knowledge about LDHs/conducting polymer hybrid. The novel design strategy presented here also have a potential application for the direct design and fabrication of other hydroxides/oxides and conductive polymers hybrid films, for obtaining high electrochemical performance supercapacitor electrode material.

Reference

1. Bae, J.; Song, M.K.; Park, Y.J.; Kim, J.M.; Liu, M.; Wang, Z.L., Fiber supercapacitors made of nanowire-fiber hybrid structures for wearable/flexible energy storage. *Angewandte Chemie International Edition* **2011,** *50* (7), 1683-1687.
2. Lu, X.; Wang, G.; Zhai, T.; Yu, M.; Xie, S.; Ling, Y.; Liang, C.; Tong, Y.; Li, Y., Stabilized TiN nanowire arrays for high-performance and flexible supercapacitors. *Nano letters* **2012,** *12* (10), 5376-5381.
3. Peng, L.; Peng, X.; Liu, B.; Wu, C.; Xie, Y.; Yu, G., Ultrathin two-dimensional MnO_2/graphene hybrid nanostructures for high-performance, flexible planar supercapacitors. *Nano letters* **2013,** *13* (5), 2151-2157.
4. He, Y.B.; Li, G.R.; Wang, Z.L.; Su, C.Y.; Tong, Y.X., Single-crystal ZnO nanorod/amorphous and nanoporous metal oxide shell composites: Controllable electrochemical synthesis and enhanced supercapacitor performances. *Energy & Environmental Science* **2011,** *4* (4), 1288-1292.
5. Li, J.; Yang, M.; Wei, J.; Zhou, Z., Preparation and electrochemical performances of doughnut-like $Ni(OH)_2$-$Co(OH)_2$ composites as pseudocapacitor materials. *Nanoscale* **2012,** *4* (15), 4498-4503.
6. Mai, L.Q.; Yang, F.; Zhao, Y.L.; Xu, X.; Xu, L.; Luo, Y.Z., Hierarchical $MnMoO_4$/$CoMoO_4$ heterostructured nanowires with enhanced supercapacitor performance. *Nature communications* **2011,** *2*, 381.
7. Wang, H.; Casalongue, H.S.; Liang, Y.; Dai, H., $Ni(OH)_2$ nanoplates grown on graphene as advanced electrochemical pseudocapacitor materials. *Journal of the American Chemical Society* **2010,** *132* (21), 7472-7477.
8. Yan, Tao.; Li, Z.J.; Li, R.Y.; Ning, Q.; Kong, H.; Niu, Y.L.; Liu, J.K., Nickel-cobalt double hydroxides microspheres with hollow interior and hedgehog-like exterior structures for supercapacitors. *Journal of Materials Chemistry* **2012,** *22* (44), 23587-23592.
9. Pan, G.X.; Xia, X.H.; Luo, J.S.; Cao, F.; Yang, Z.H.; Fan, H.J., Preparation of CoAl layered double hydroxide nanoflake arrays and their high supercapacitance performance. *Applied Clay Science* **2014,** *102*, 28-32.
10. Zhang, Y.; Feng, H.; Wu, X.; Wang, L.; Zhang, A.; Xia, T.; Dong, H.; Li, X.; Zhang, L., Progress of electrochemical capacitor electrode materials: A review. *International journal of hydrogen energy* **2009,** *34* (11), 4889-4899.
11. Huang, J.; Lei, T.; Wei, X.; Liu, X.; Liu, T.; Cao, D.; Yin, J.; Wang, G., Effect of Al-doped β-$Ni(OH)_2$ nanosheets on electrochemical behaviors for high performance supercapacitor application. *Journal of Power Sources* **2013,** *232*, 370-375.

12. Abushrenta, N.; Wu, X.; Wang, J.; Liu, J.; Sun, X., Hierarchical Co-based porous layered double hydroxide arrays derived via alkali etching for high-performance supercapacitors. *Scientific reports* **2015,** *5*, 13082.
13. Goh, K.H.; Lim, T.T.; Dong, Z., Application of layered double hydroxides for removal of oxyanions: a review. *Water research* **2008,** *42* (6-7), 1343-1368.
14. Malak-Polaczyk, A.; Vix-Guterl, C.; Frackowiak, E., Carbon/layered double hydroxide (LDH) composites for supercapacitor application. *Energy & Fuels* **2010,** *24* (6), 3346-3351.
15. Wang, Y.G.; Cheng, L.; Xia, Y.Y., Electrochemical profile of nano-particle CoAl double hydroxide/active carbon supercapacitor using KOH electrolyte solution. *Journal of power sources* **2006,** *153* (1), 191-196.
16. Yang, J.; Yu, C.; Fan, X.; Ling, Z.; Qiu, J.; Gogotsi, Y., Facile fabrication of MWCNT-doped NiCoAl-layered double hydroxide nanosheets with enhanced electrochemical performances. *Journal of Materials Chemistry A* **2013,** *1* (6), 1963-1968.
17. Hong, W.; Wang, J.; Niu, L.; Sun, J.; Gong, P.; Yang, S., Controllable synthesis of CoAl LDH@Ni(OH)$_2$ nanosheet arrays as binder-free electrode for supercapacitor applications. *Journal of Alloys and Compounds* **2014,** *608*, 297-303.
18. Chen, Z.; Augustyn, V.; Jia, X.; Xiao, Q.; Dunn, B.; Lu, Y., High-performance sodium-ion pseudocapacitors based on hierarchically porous nanowire composites. *ACS nano* **2012,** *6* (5), 4319-4327.
19. Han, J.; Dou, Y.; Zhao, J.; Wei, M.; Evans, D.G.; Duan, X., Flexible CoAl LDH@PEDOT Core/Shell Nanoplatelet Array for High-Performance Energy Storage. *Small* **2013,** *9* (1), 98-106.
20. Liu, R.; Duay, J.; Lee, S. B., Redox exchange induced MnO$_2$ nanoparticle enrichment in poly(3,4-ethylenedioxythiophene) nanowires for electrochemical energy storage. *ACS Nano* **2010,** *4* (7), 4299-4307.
21. Rakhi, R.; Chen, W.; Cha, D.; Alshareef, H.N., Substrate dependent self-organization of mesoporous cobalt oxide nanowires with remarkable pseudocapacitance. *Nano letters* **2012,** *12* (5), 2559-2567.
22. Shao, M.; Ning, F.; Zhao, Y.; Zhao, J.; Wei, M.; Evans, D.G.; Duan, X., Core-shell layered double hydroxide microspheres with tunable interior architecture for supercapacitors. *Chemistry of Materials* **2012,** *24* (6), 1192-1197.
23. Zhao, J.; Lu, Z.; Shao, M.; Yan, D.; Wei, M.; Evans, D.G.; Duan, X., Flexible hierarchical nanocomposites based on MnO$_2$ nanowires/CoAl hydrotalcite/carbon fibers for high-performance supercapacitors. *RSC Advances* **2013,** *3* (4), 1045-1049.

24. Shao, M.; Li, Z.; Zhang, R.; Ning, F.; Wei, M.; Evans, D. G.; Duan, X., Hierarchical Conducting Polymer@Clay Core-Shell Arrays for Flexible All-Solid-State Supercapacitor Devices. *Small* **2015,** *11* (29), 3530-3538.
25. Bhadra, S.; Khastgir, D.; Singha, N.K.; Lee, J.H., Progress in preparation, processing and applications of polyaniline. *Progress in polymer science* **2009,** *34* (8), 783-810.
26. MacDiarmid, A.G., "Synthetic metals": A novel role for organic polymers (Nobel lecture). *Angewandte Chemie International Edition* **2001,** *40* (14), 2581-2590.
27. Snook, G.A.; Kao, P.; Best, A.S., Conducting-polymer-based supercapacitor devices and electrodes. *Journal of power sources* **2011,** *196* (1), 1-12.
28. Zhang, K.; Zhang, L.L.; Zhao, X.; Wu, J., Graphene/polyaniline nanofiber composites as supercapacitor electrodes. *Chemistry of Materials* **2010,** *22* (4), 1392-1401.
29. Kresse, G.; Furthmüller, J., Efficient iterative schemes for ab initio total-energy calculations using a plane-wave basis set. *Physical review B* **1996,** *54* (16), 11169.
30. Kresse, G.; Joubert, D., From ultrasoft pseudopotentials to the projector augmented-wave method. *Physical Review B* **1999,** *59* (3), 1758.
31. Adachi, H.; Tsukuda, M.; Satoko, C., Discrete variational Xα cluster calculations. I. Application to metal clusters. *Journal of the Physical Society of Japan* **1978,** *45* (3), 875-883.
32. Muralidharan, N.; Westover, A.S.; Sun, H.; Galioto, N.; Carter, R.E.; Cohn, A.P.; Oakes, L.; Pint, C.L., From the Junkyard to the Power Grid: Ambient Processing of Scrap Metals into Nanostructured Electrodes for Ultrafast Rechargeable Batteries. *ACS Energy Letters* **2016,** *1* (5), 1034-1041.
33. Mai, L.Q.; Minhas-Khan, A.; Tian, X.; Hercule, K.M.; Zhao, Y.L.; Lin, X.; Xu, X., Synergistic interaction between redox-active electrolyte and binder-free functionalized carbon for ultrahigh supercapacitor performance. *Nature communications* **2013,** *4*, 2923.
34. Gao, H.; Jiang, T.; Han, B.; Wang, Y.; Du, J.; Liu, Z.; Zhang, J., Aqueous/ionic liquid interfacial polymerization for preparing polyaniline nanoparticles. *Polymer* **2004,** *45* (9), 3017-3019.
35. Kutlu, B.; Leuteritz, A.; Boldt, R.; Jehnichen, D.; Wagenknecht, U.; Heinrich, G., PANI-LDH prepared by polymerization-adsorption method and processing to conductive compounds. *Applied Clay Science* **2013,** *72*, 91-95.
36. Leng, W.; Zhou, S.; Gu, G.; Wu, L., Wettability switching of SDS-doped polyaniline from hydrophobic to hydrophilic induced by alkaline/reduction reactions. *Journal of colloid and interface science* **2012,** *369* (1), 411-418.

37. Trchová, M.; Stejskal, J., Polyaniline: The infrared spectroscopy of conducting polymer nanotubes (IUPAC Technical Report). *Pure and Applied Chemistry* **2011,** *83* (10), 1803-1817.
38. Chatterjee, S.; Salaün, F.; Campagne, C., The influence of 1-butanol and trisodium citrate ion on morphology and chemical properties of chitosan-based microcapsules during rigidification by alkali treatment. *Marine drugs* **2014,** *12* (12), 5801-5816.
39. Kloprogge, J.T.; Hickey, L.; Frost, R.L., FT-Raman and FT-IR spectroscopic study of synthetic Mg/Zn/Al-hydrotalcites. *Journal of Raman Spectroscopy* **2004,** *35* (11), 967-974.
40. Han, J.B.; Lu, J.; Wei, M.; Wang, Z.L.; Duan, X., Heterogeneous ultrathin films fabricated by alternate assembly of exfoliated layered double hydroxides and polyanion. *Chemical Communications* **2008,** (41), 5188-5190.
41. Sinha, S.; Bhadra, S.; Khastgir, D., Effect of dopant type on the properties of polyaniline. *Journal of Applied Polymer Science* **2009,** *112* (5), 3135-3140.
42. Zheng, W.; Angelopoulos, M.; Epstein, A.; MacDiarmid, A., Concentration dependence of aggregation of polyaniline in NMP solution and properties of resulting cast films. *Macromolecules* **1997,** *30* (24), 7634-7637.
43. Fan, G.; Wang, H.; Xiang, X.; Li, F., Co-Al mixed metal oxides/carbon nanotubes nanocomposite prepared via a precursor route and enhanced catalytic property. *Journal of Solid State Chemistry* **2013,** *197*, 14-22.
44. Nguyen, V.H.; Shim, J.J., Green synthesis and characterization of carbon nanotubes/polyaniline nanocomposites. *Journal of Spectroscopy* **2015,** *2015*.
45. Augustyn, V.; Simon, P.; Dunn, B., Pseudocapacitive oxide materials for high-rate electrochemical energy storage. *Energy & Environmental Science* **2014,** *7* (5), 1597-1614.
46. Fang, J.; Li, M.; Li, Q.; Zhang, W.; Shou, Q.; Liu, F.; Zhang, X.; Cheng, J., Microwave-assisted synthesis of CoAl-layered double hydroxide/graphene oxide composite and its application in supercapacitors. *Electrochimica Acta* **2012,** *85*, 248-255.
47. Zhou, Y.; Xu, H.; Lachman, N.; Ghaffari, M.; Wu, S.; Liu, Y.; Ugur, A.; Gleason, K.K.; Wardle, B.L.; Zhang, Q., Advanced asymmetric supercapacitor based on conducting polymer and aligned carbon nanotubes with controlled nanomorphology. *Nano Energy* **2014,** *9*, 176-185.
48. Masikhwa, T.M.; Dangbegnon, J.K.; Bello, A.; Madito, M.J.; Momodu, D.; Manyala, N., Preparation and electrochemical investigation of the cobalt hydroxide carbonate/activated carbon nanocomposite for supercapacitor applications. *Journal of Physics and Chemistry of Solids* **2016,** *88*, 60-67.
49. Cooper, S.J.; Bertei, A.; Finegan, D.P.; Brandon, N.P., Simulated impedance of diffusion in porous media. *Electrochimica Acta* **2017,** *251*, 681-689.

50. Chamaani, A.; Safa, M.; Chawla, N.; Herndon, M.; El-Zahab, B., Stabilizing effect of ion complex formation in lithium-oxygen battery electrolytes. *Journal of Electroanalytical Chemistry* **2018,** *815*, 143-150.
51. Lu, X.; Zheng, D.; Zhai, T.; Liu, Z.; Huang, Y.; Xie, S.; Tong, Y., Facile synthesis of large-area manganese oxide nanorod arrays as a high-performance electrochemical supercapacitor. *Energy & Environmental Science* **2011,** *4* (8), 2915-2921.
52. Yuan, L.; Yao, B.; Hu, B.; Huo, K.; Chen, W.; Zhou, J., Polypyrrole-coated paper for flexible solid-state energy storage. *Energy & Environmental Science* **2013,** *6* (2), 470-476.
53. Wang, J.; Wu, J.; Bai, H., Degradation-induced capacitance: A new insight into the superior capacitive performance of polyaniline/graphene composites. *Energy & Environmental Science* **2017,** *10* (11), 2372-2382.
54. Wu, J.; Wang, J.; Huang, X.; Bai, H., A self-assembly route to porous polyaniline/reduced graphene oxide composite materials with molecular-level uniformity for high-performance supercapacitors. *Energy & Environmental Science* **2018,** *11* (5), 1280-1286.
55. Planes, G.; Rodriguez, J.; Miras, M.; Garcia, G.; Pastor, E.; Barbero, C., Spectroscopic evidence for intermediate species formed during aniline polymerization and polyaniline degradation. *Physical Chemistry Chemical Physics* **2010,** *12* (35), 10584-10593.
56. Deng, J.; Wang, T.; Guo, J.; Liu, P., Electrochemical capacity fading of polyaniline electrode in supercapacitor: An XPS analysis. *Progress in Natural Science: Materials International* **2017,** *27* (2), 257-260.
57. Wang, Y.; Dong, S.; Wu, X.; Li, M., One-step electrodeposition of MnO_2@ NiAl layered double hydroxide nanostructures on the nickel foam for high-performance supercapacitors. *Journal of The Electrochemical Society* **2017,** *164* (2), H56-H62.
58. Nakagaki, R.; Frost, D.; McDowell, C., The intramolecular charge-transfer interaction in X-ray photoelectron spectroscopy: the charge-transfer satellites observed in p-nitroaniline and related compounds. *Journal of Electron Spectroscopy and Related Phenomena* **1980,** *19* (3), 355-370.
59. Nakagaki, R.; Frost, D.; McDowell, C., X-ray photoelectron spectroscopy of nitroanilines and their derivatives. *Journal of Electron Spectroscopy and Related Phenomena* **1981,** *22* (3), 289-296.
60. Nakayama, M.; Saeki, S.; Ogura, K., In situ observation of electrochemical formation and degradation processes of polyaniline by fourier-transform infrared spectroscopy. *Analytical sciences* **1999,** *15* (3), 259-263.
61. Yang, X.; Xie, Q.; Yao, S., A comparative study on polyaniline degradation by an electrochemical quartz crystal impedance system: electrode and solution effects. *Synthetic metals* **2004,** *143* (1), 119-128.

Chapter 4 Effects of a Strong Magnetic Field on Microstructure Orientation in CoAl Layered Double Hydroxide Prepared by Hydrothermal and Slip Casting Methods

4.1 Introduction

The application of a magnetic field for advanced materials have attracted considerable attention owing to their potential application in improving the optical, mechanical, chemical, electronic properties, and so on [1-3]. The controlled development of the crystal orientation in nanomaterial is very useful for improving its properties. Recently, it has been found that a crystal orientation in materials can be controlled by imposition of a high magnetic field. The effects of a high magnetic on crystal orientation is not only ferromagnetic materials but also nonmagnetic ones such as paramagnetic and diamagnetic [4-7]. Layered double hydroxides (LDHs), also called anionic clays, have the following general formula: $\mathrm{M}_{1-x}^{2+}\mathrm{M}_{x}^{3+}(\mathrm{OH})_2(\mathrm{A}^{n-})_{x/n}\cdot \mathrm{mH_2O}$, where M^{2+} and M^{3+} are divalent and trivalent, and A^{n-} is the interlayer anion. CoAl LDH is a very attractive transition metal hydroxide material because of its excellent properties, such as good thermal stability, unique structural anisotropy, high redox activity, and flexible ion-exchangeability [8-9]. Nowadays, CoAl LDH nanomaterials are considered as promising candidates for a range of applications, as catalysts, vehicles for drug delivery, anion exchangers, and electrode material [10-12]. The fabrication of the oriented CoAl LDH nanostructure is one of the effective ways to improve its properties. Recently, magnetic-field-assisted assembly of CoFe LDH ultrathin film has been achieved by layer-by-layer method [2], which gives us the impetus to explore the fabrication of oriented CoAl LDH nanofilm with the assistance of an external magnetic field. Synthetic LDHs mainly include coprecipitation, ion-exchange, hydrothermal, and urea hydrolysis methods [13]. Among these methods, hydrothermal method is the simplest and most commonly used fabrication method for the preparation of CoAl LDH nanomaterials. Hydrothermal reaction can also directly synthesis of CoAl LDH nanofilm on substrates without binder, and this strategy is also advantageous to keep its nanostructure. Little is known, however, about the investigation of hydrothermal synthesis of oriented LDH film by an applied magnetic field.

Usually, an asymmetric crystal structure must give anisotropic magnetic susceptibilities. When the particles with an anisotropic magnetic susceptibility are placed in a magnetic field, a magnetic torque is generated from the interaction between this anisotropy and a magnetic field

[14]. For the CoAl LDH film grows directly on the substrate, the adhesion between the substrate and film is strong in the case of the out-of-flatness substrate surfaces provide bonding sites for the crystal growth; this may also prevent each nanosheet in the film from free rotation under a magnetic field. So, in order to fully investigate the induction effect of magnetic field on CoAl LDH, it is necessary for the study the CoAl LDH particle under application of a magnetic field. A well-dispersed suspension of particle is necessary for the effective utilization of a magnetic field, because the presence of van der Waals attraction between the fine particles causing them tend to spontaneously agglomerate. It is necessary to use colloidal processing for controlling the stability of particles in order to effectively use a magnetic field to rotate the particles. However, very little is known about the investigation oriented LDH achieved using colloidal processing with the assistance of an external magnetic field. This study would usefully supplement and extend the research field for fabricating the advanced LDHs material with the assistance of an external magnetic field.

The effect of the applied strong magnetic field on the molecular structure, crystal phase, morphology, and the crystal orientation of CoAl LDH prepared by hydrothermal synthesis and slip casting, has been investigated with the assistance of an external magnetic field.

4.2 Materials and Methods

4.2.1 Hydrothermal synthesis of CoAl LDH nanosheet films

In a typical hydrothermal synthesis, 0.26 mmol of $Co(NO_3)_2 \cdot 6H_2O$, 0.09 mmol of $Al(NO_3)_3 \cdot 9H_2O$, 0.86 mmol of NH_4F and 1.71 mmol of $CO(NH_2)_2$ were added in 15 mL distilled water under 15 min magnetic stirring. The mixed solution was transferred to a 20 mL Teflon lined stainless steel autoclave. Then, a piece of clean titanium plates (30 mm × 10 mm × 0.1 mm) was immersed into the reaction solution. The autoclave was sealed and placed in a heating jacket with covered the thermal insulation lid. Then the heating jacket was placed in the central position of the magnet bore in the magnetic field device. When the preset magnetic field strength was reached 12 T, the temperature control device was activated, and the temperature maintains at 120 °C for 6 h. After the reaction was completed, the superconducting magnet device was turned off, and the autoclave was removed. Finally, the thin film samples on Ti substrate was taken out gently from the solution and washed three times with distilled water. Meanwhile, the pink precipitates were collected and washed with distilled water for several times. The samples were then dried at 60 °C for 2h. For comparison, one specimen was prepared by hydrothermal synthesis without applying a strong magnetic field.

4.2.2 Slip casting of CoAl LDH nanosheets

The as-synthesized CoAl LDH powders were used as the starting materials for colloidal processing. Ethyl alcohol suspensions were prepared that contained 35 vol%; the solids consisted of CoAl LDH that include 15 wt% polyvinylpyrrolidone (PVP, K90) as the binder. The suspension was ultrasonicated for 20 min and stirred for 6 h. The suspension was put into a vacuum desiccator to remove the air. Then the suspension was poured into a gypsum mold and left to be consolidated by slip casting. A strong magnetic field of 12 T was applied to the suspension during slip casting at room temperature. The direction of the magnetic field was parallel and perpendicular to the casting direction. For comparison, one sample was prepared by slip casting without applying a strong magnetic field.

The degree of crystalline orientation was evaluated by the Lotgering orientation factor (f) from the intensities of the X-ray diffraction lines, as shown in equation (1).

$$f = \frac{P - P_0}{1 - P_0}$$

Where P and P_0 were obtained from the ratio of $\sum I(0kl)/\sum I(hkl)$. The value of P was calculated from the textured CoAl LDH sample. The value of P_0 was calculated from the ICDD card as randomly oriented specimens.

4.2.3. Structural characterization

The chemical structures of the samples were examined by Fourier transform infrared spectrometer (FT-IR, FTIR4100, JASCO) analysis with ATR attachment. X-ray diffraction patterns of the samples were obtained on an X-ray diffractometer with monochromated Cu Kα radiation (XRD, RINT-2100, Rigaku). The surface morphologies of the films were characterized by field emission scanning electron microscopy (FESEM, JSM-6500F, JEOL) equipped with EDX analyzer. The surface composition of the samples was analyzed by X-ray photoelectron spectroscopy (XPS, AXIS Ultra DLD, Kratos). A strong magnetic field was used in a room temperature bore of a superconducting magnet (JASTEC Inc., JMTD-12T100NC5).

4.3 Results and Discussion

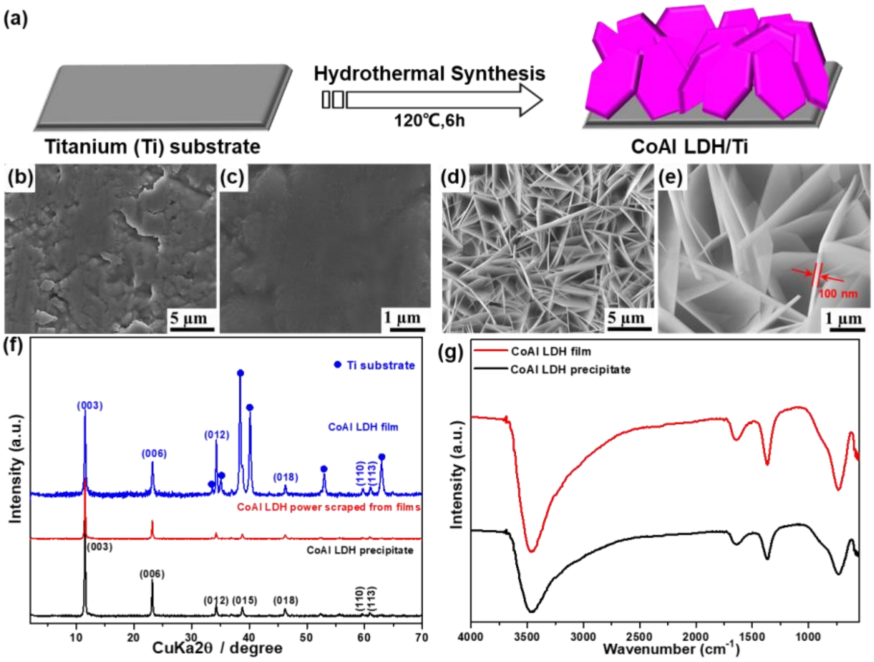

Figure 4.1. (a) Schematic illustration of the fabrication of CoAl LDH nanosheet structures. SEM images of (b,c) the Ti surface and (d,e) after covering with CoAl LDH. (f) XRD patterns of CoAl LDH precipitate, CoAl LDH film, and CoAl LDH powder scrapped from film samples. (g) FT-IR spectra of CoAl LDH film and CoAl LDH precipitate.

4.3.1 Structural study

The fabrication process of CoAl LDH nanosheet film is illustrated in Figure 4.1a. Through the homogeneous hydrothermal process, the SEM reveals that CoAl LDH nanosheets are grown and well distributed across the substrate surface with forming the porous structure (Figure 4.1d), and the nanosheet with the thickness of ~100 nm (Figure 4.1e). The crystal phase and molecular structure of as-synthesized CoAl LDH were investigated by XRD and FT-IR spectroscopy. As shown in Figure 4.1f, the XRD patterns of CoAl LDH precipitate and CoAl LDH film are consistent with that of the desired CoAl LDH phase (JCPDS: 51-0045). As shown in Figure 4.1g, the FT-IR spectrum of the CoAl LDH film is identical to that of the CoAl LDH precipitate. The strong, broad band around 3500 cm^{-1} can be explained as the metal-OH stretching mode and hydrogen bond interlayer H_2O surrounding the interlayer anion [15]. The intense peaks at 1360 and 740 cm^{-1} are assigned to the asymmetric stretching vibration of the C-O bond, which caused by the interlayer of CO_3^{2-} in CoAl LDH. The lower wavenumber absorption bands at 400-700 cm^{-1} belongs to the M-O, O-M-O, and M-O-M related vibrational modes of LDHs [8]. From the XRD and FTIR analyses, the results indicated that CoAl LDH could grow well on the substrate by the hydrothermal synthesis.

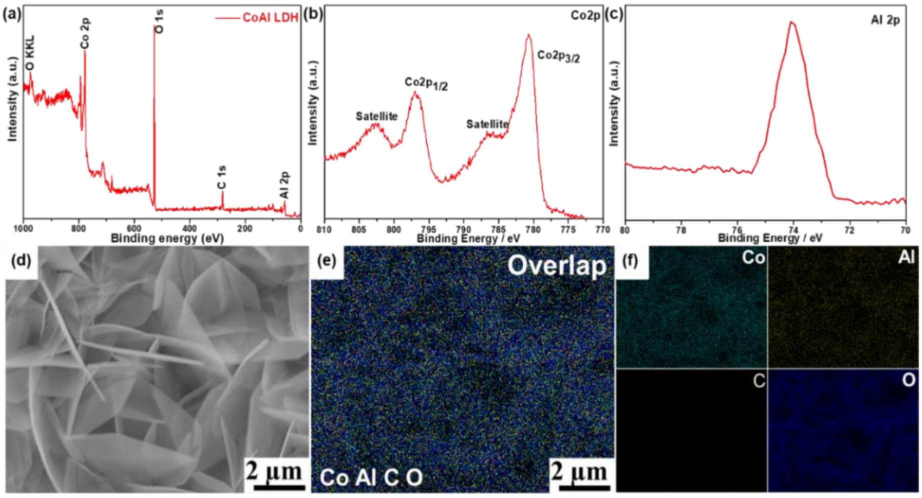

Figure 4.2. (a) The XPS full spectra, (b) Co2p spectrum and (c) N1s spectrum of CoAl LDH. (d-f) FESEM image of CoAl LDH corresponding to the EDX elemental mapping images of Co, Al, C, and O showing uniform distribution of the elements.

We further characterized the chemical composition and elemental distribution of the CoAl LDH by XPS and EDX. As shown in Figure 4.2a, Co 2p, Al 2p, C 1s, and O 1s peaks appear in the survey spectrum of CoAl LDH, suggesting stacked CO_3^{2-}-LDH in CoAl-LDH. The Co 2p and Al 2p spectrum (Figure 4.2b,c) are also consistent with previously reported [16-17]. EDX mapping analysis (Figure 4.2d-f) displayed a homogeneous distribution of the element (Co, Al, C, O) in the CoAl LDH nanofilm, which also implied the CoAl LDH nanosheets were well distributed on the substrate surfaces.

4.3.2 Growth process and mechanism of CoAl LDH on the Ti substrate

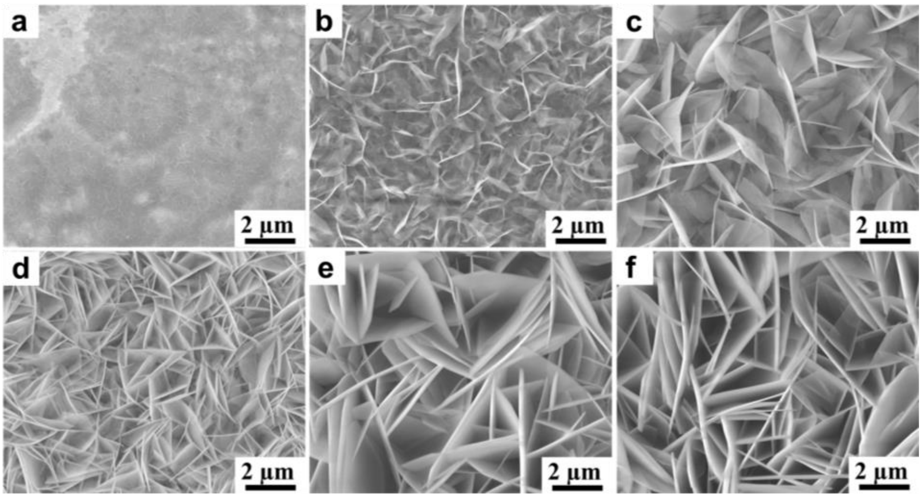

Figure 4.3. SEM images of the products obtained on Ti substrate at various hydrothermal reaction times: (a) 0.5 h, (b) 1 h, (c) 2 h, (d) 3 h, (e) 4 h, (f) 6 h.

To better understand the factors controlling the crystalline orientation of CoAl LDH nanosheet film, the growth process was followed by SEM. As shown in Figure 4.3, the SEM images of the products were obtained on the substrate at various reaction times. Before the hydrothermal reaction, it can be seen from Figure 4.1b,c that the surface of the pretreated Ti substrate is out-of-flatness. The defect site on the Ti surface can offer the hetero-nucleation site for the growing of nanoparticle. After 0.5 h, a film with small particles of CoAl-LDH nuclei was observed on the Ti surface (Figure 4.3a), and the number and size of the LDH nuclei slowly increased from 1 to 2 h (Figure 4.3b,c). From this point, the growth of the LDH accelerated and a dense film of LDH nanosheets with their (00*l*) planes perpendicular to the surface of the Ti formed gradually (Figure 4.3d). Hereafter, the LDH platelets grew rapidly with time (Figure 4.3e and f). These results reveal that the formation process of CoAl LDH nanosheets on the Ti substrate included both crystal nucleation and growth, and the nucleation is the rate-determining step.

Preferential orientation during LDHs crystal growth on solid surfaces has been observed on a variety of substrate materials, including PAO/Al, graphene oxide, polystyrene, nickel, and glass substrates [10, 20-23]. Herein, “evolution selection” which has used to explain the preferred orientation of LDH film with the ab face of the crystallites perpendicular to the substrate, which has also been supported by earlier reported [20, 24]. In the early growth stages, crystal seeds would grow in all possible directions. But for an anisotropic CoAl LDH crystallite, growth in the c-direction is significantly slower than that in the ab-direction, which resulted in the direction with the fastest growth rate makes a different angle to the normal to the surface for each crystal. When two crystals meet, the less steeply growing crystal is prevented from further growth by the more steeply growing crystal, which continues to grow. Repetition of this process ensures that crystals with their fastest growth direction normal to the substrate eventually envelop all the other crystals and finally dominate the film. Ultimately, the film becomes dominated by crystallites growing with their ab-planes perpendicular to the substrate.

4.3.3 The study of magnetic field on hydrothermal growth of CoAl LDH

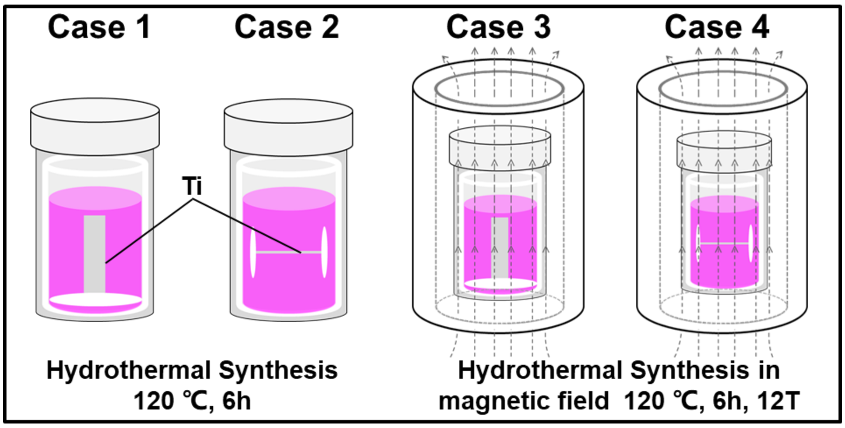

Figure 4.4. The schematic view of the experimental apparatus for hydrothermal synthesis (case 1, 2) and hydrothermal synthesis under a strong magnetic field (case 3, 4).

The present experimental apparatus of the hydrothermal synthesis is shown schematically in Figure 4.4. A Ti plate was immersed into aqueous solution, and the plane of the Ti plate was set in parallel (the specimen labelled as Case 1) and perpendicular (the specimen labelled as Case 2) to the direction of gravity, respectively. For comparison, a strong magnetic field of 12 T was applied to the hydrothermal growth process. The plane of the Ti plate was set in parallel (the specimen labelled as Case 3) and perpendicular (the specimen labelled as Case 4) to the direction of gravity with applying a strong magnetic field.

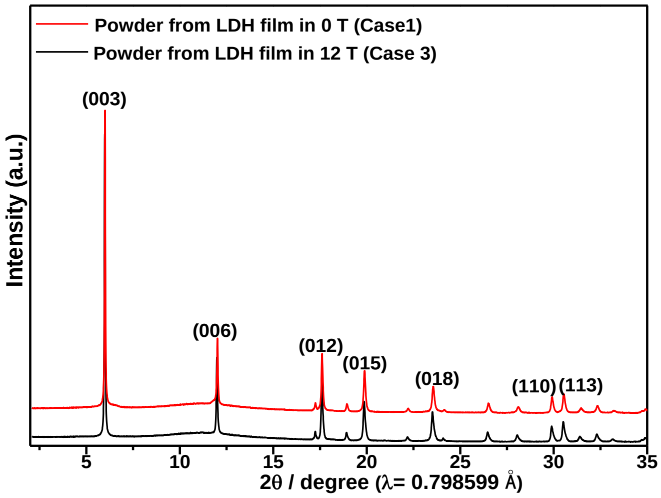

Figure 4.5. SXRD patterns of the powder obtained from CoAl LDH film in 0 T (Case 1) and 12 T (Case 3).

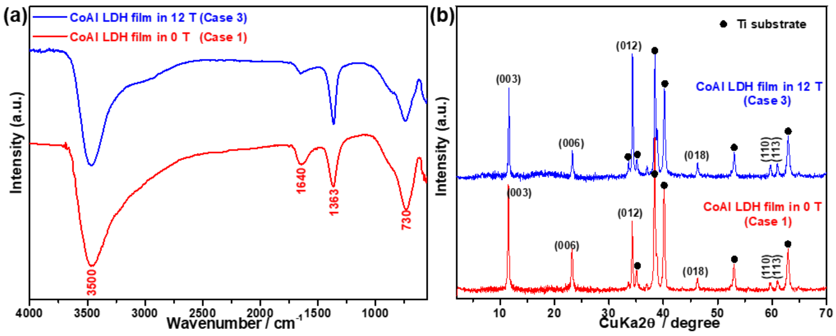

Figure 4.6. (a) FT-IR spectra and (b) XRD patterns of CoAl LDH film obtained in 0 T (Case 1) and 12 T (Case 3).

To verify the effect of the strong magnetic field on the crystal phase of the CoAl LDH, the SXRD measurements were first performed. As shown in Figure 4.5, the SXRD patterns of CoAl LDH obtained in Case 3 can be very well indexed to CoAl LDH obtained in Case 1, including the intensity and position of each diffraction peak. It indicated the strong magnetic field could not change the CoAl LDH crystal phase during the hydrothermal growth process. In other words, the CoAl LDH crystal structure can also well keep balance between the positively charged plates and interlayer anions under an external strong magnetic field. Figure 4.6a illustrates the FT-IR spectra of CoAl LDH films obtained in 0 T and 12 T. The water molecules in the interlayer region connected to both the metal hydroxide layers and interlayer anions through extensive hydrogen bonding [25-27]. And some studies confirmed that these hydrogen bonds were continuously breaking and reforming and that the water molecules were in a continuous state of flux [28]. Hence the precise nature of the interlayer region is extremely complex. Usually, the amount of interlayer water in the LDHs is determined by factors such as the nature of the interlayer anions, the water vapour pressure and temperature [29-30]. For the CoAl LDH sample obtained in 12 T, very interesting is the observation that the decreases in the intensity of the absorption peak of the H-O-H bending vibration at 1640 cm^{-1}, which are probably attributed to the interlayer water molecules contents decrease. Presumably, the strong magnetic field may weak the integrated hydrogen bonding network among the hydroxyl slabs, the interlayer anions and water molecules. As a result, it can lead to the water molecules to not stably insert between the layers of a LDH. Unfortunately, this process could not be observed in any other way. Figure 4.6b illustrates the XRD patterns of CoAl LDH films obtained in 0 T and 12 T. It is noteworthy that the relative intensities of the peaks corresponding to the (012)/(003) and (012)/(006) planes become larger for the CoAl LDH film obtained in Case 3, indicating that a preferred orientation of (012) plane in the CoAl LDH nanofilm obtained with the assistance of magnetic field. Hence, it is expected that the application of external magnetic fields during hydrothermal synthesis can induce orientated growth of the LDH crystals along the easy magnetic axis.

Based on the measured XRD data, the degree of CoAl LDH nanosheets orientation was evaluated by the Lotgering orientation factor (f), as shown in equation (1). For the specimen synthesized in Case 1, the degree of crystalline CoAl LDH is approximates to 0.21. By comparison, as to the specimens synthesized in Case 3, the orientation factor f is 0.46, which is much larger than that of the specimens prepared without magnetic field. It indicated that under the assistance of a strong magnetic field, the preferred growth orientation is along the (0kl) direction (bc plane). These results revealed that the application of a strong magnetic field could induce different oriented polycrystalline structures, which will be further discussed below.

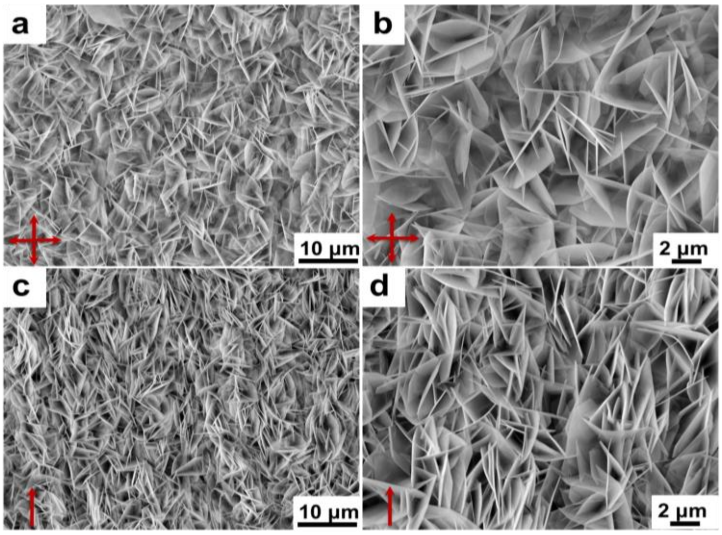

Figure 4.7. SEM images of (a, b) CoAl LDH film obtained in 0 T (Case 1) and (c, d) CoAl LDH film obtained in 12 T (Case 3).

Figure 4.7 shows the microstructures of the CoAl LDH nanosheet films synthesized in Case 1 and Case 3. It can be seen that the films consist of thin nanosheets, which are the typical morphology of CoAl LDH. In addition, the thickness of CoAl LDH nanosheets prepared in 12 T is consist with that of CoAl LDH nanosheets prepared in 0 T. However, the applied strong magnetic field has an obvious effect on the development of oriented CoAl LDH nanofilm. For the CoAl LDH synthesized in Case 1 (Figure 4.7a,b), the nanofilm is composed of tightly packed nanosheets with ab plane vertically arranged on the substrate in large amounts, and the ab plane vertically arranged in arbitrary directions. As to the CoAl LDH synthesized in Case 3 (Figure 4.7c,d), it is worthy to note that although the nanofilm has the similar morphology with the Case 1, the nanosheets become more closely packed and align along the bc plane in accord with the magnetic field direction. This result shows that the development of the CoAl LDH/Ti orientation could be influenced by a strong magnetic field which is also consistent with the above XRD results.

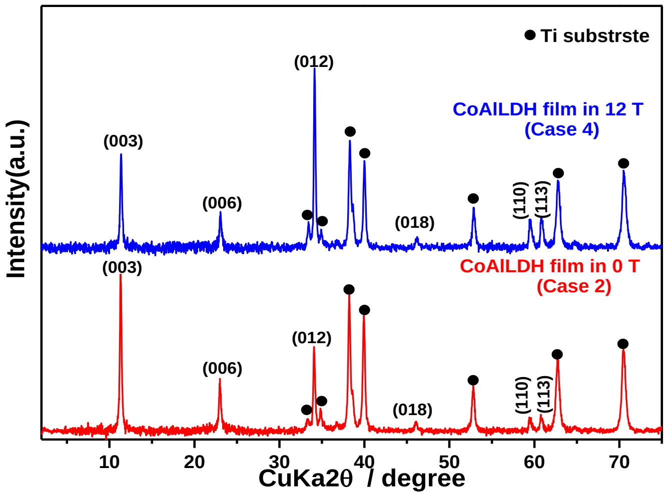

Figure 4.8. XRD patterns of CoAl LDH film obtained in 0 T (Case 2) and 12 T (Case 4).

We further studied the effect of the strong magnetic field on the orientation of CoAl LDH nanosheets synthesized in Case 2 and Case 4. Figure 4.8 shows XRD patterns of the specimens prepared in 0 T and 12 T, respectively. The XRD patterns of two specimens match well with the CoAl LDH precipitation (Figure 4.1f), indicating the strong magnetic field has no effect on the crystal phase of the product. Notably, the relative intensities of the peaks relevant to the (003)/(012) and (006)/(012) planes become obviously decrease for the specimen prepared with a strong magnetic field, indicating that under the assistance of magnetic field, the preferred growth orientation is along the (0*kl*) plane. For the specimens synthesized in Case 2, the degree of crystalline CoAl LDH is approximates to 0.15. By comparison, as to the specimens synthesized in Case 4, the Lotgering orientation factor f is 0.37, which is much larger than that of the specimens synthesized in Case 2. This result indicates that the development of the CoAl LDH orientation can be controlled by utilizing a strong magnetic field and that the preferred growth orientation is along the (0*kl*) direction (bc plane).

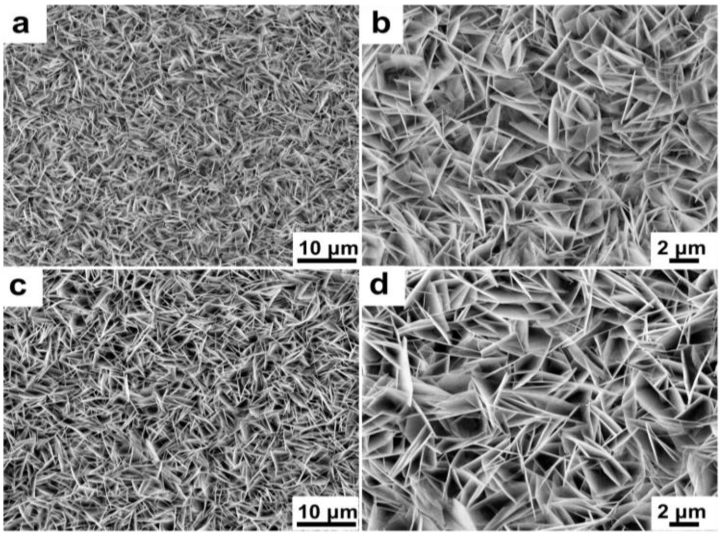

Figure 4.9. SEM images of (a, b) CoAl LDH film obtained in 0 T (Case 2) and (c, d) CoAl LDH film obtained in 12 T (Case 4).

As shown in Figure 4.9, the SEM images of CoAl LDH nanofilms synthesized in Case 2 and Case 4. One can see that both specimens consist of nanofilms constructed of thin nanosheets. Furthermore, the applied strong magnetic field has little effect on the nanosheet size of hydrothermally synthesized CoAl LDH, but some change is observed in the morphology. As to the CoAl LDH synthesized in Case 2 (Figure 4.9a,b), the nanofilm was consist of tightly packed nanosheets with ab plane nearly vertically arranged on the substrate and ab plane arranged in arbitrary directions. For the CoAl LDH synthesized in Case 4 (Figure 4.9c,d), it is worthy to note that although the nanofilm has the similar morphology with the Case 2, the CoAl LDH nanofilm consist of closely packed nanosheets with forming the porous structure and the ab plane more nearly vertical arranged on the substrate. This result shows that the development of the CoAl LDH/Ti orientation could be influenced by a strong magnetic field which is also consistent with the XRD results (Figure 4.8).

4.3.4 The study of oriented CoAl LDH by slip casting in magnetic field

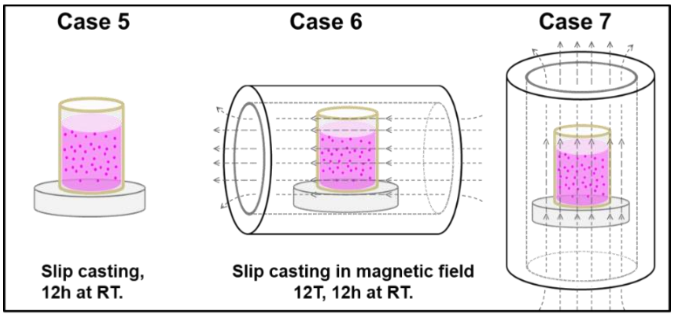

Figure 4.10. The schematic view of experimental apparatus for slip casting in 0 T (Case 5) and slip casting under a strong magnetic field of 12 T (Case 6,7).

For the CoAl LDH nanosheet films prepared by hydrothermal method, the in-situ growth of nanosheets on a Ti substrate was inhibited the individual crystal rotation to some extent in the magnetic field. Then, a slip-casting process under a magnetic field was used to study the crystal orientation of CoAl LDH. The present experimental apparatus of the slip casting is shown schematically in Figure 4.10. A strong magnetic field of 12 T was applied to the suspension during slip casting at room temperature. The direction of the magnetic field was perpendicular (the specimen labelled as Case 6) and parallel (the specimen labelled as Case 7) to the direction of gravity, respectively. For comparison, one specimen labelled as Case 5 was prepared without applying a magnetic field.

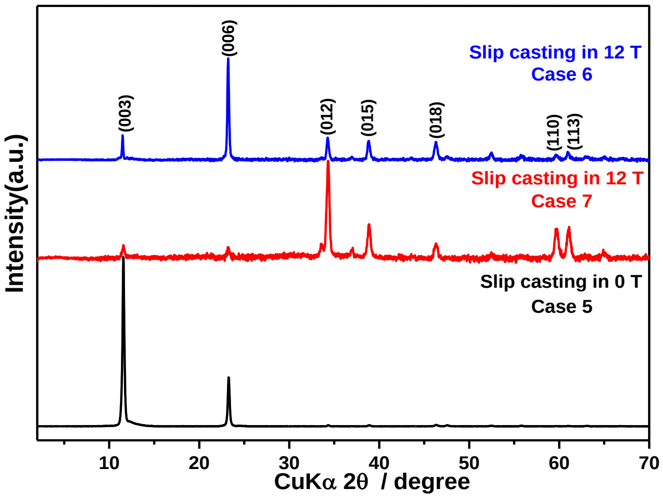

Figure 4.11. XRD patterns of CoAl LDH samples obtained from the slip casting method with and without a 12 T magnetic field.

Figure 4.11 shows the XRD patterns of the CoAl LDH are compacted by slip casting with and without an applied magnetic field. It has a pronounced difference in the degree of crystal orientation in an XRD analysis, which was detected between the specimens treated with and without an applied magnetic field during slip casting. As shown in Case 5, it is clearly observed that only the (00*l*) peaks of the CoAl LDH have the very high diffraction intensities, suggesting that the CoAl LDH possesses c-axis preferred orientation. As shown in Case 6, with the assistance of an external magnetic field, the relative intensities of the peaks corresponding to the (0*kl*) /(00*l*) planes become much stronger, indicating that the development of the CoAl LDH orientation can be induced by a strong magnetic field. When the CoAl LDH prepared in Case 7, the intensity of the (012) peak is increased remarkably compared with the Case 5 without exposure to the magnetic field, and the intensities of (003) and (006) peaks almost diminished. Such a difference resulted from a preferred orientation of LDH crystallites possess b,c-axes crystals align in the magnetic field direction.

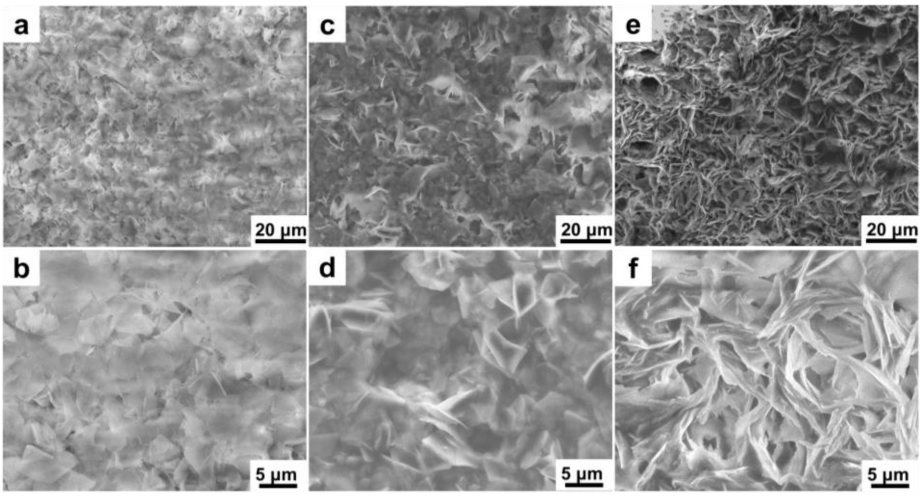

Figure 4.12. SEM micrograph of CoAl LDH powder prepared by slip casting: (a,b) specimen without applying a magnetic field (Case 5), (c,d) specimen in12 T (Case 6), and (e,f) specimen in12 T (Case 7).

Figure 4.12 shows the microstructure of the top surface of the CoAl LDH nanosheets prepared by slip casting with and without applying a magnetic field. As shown in Figure 4.12a,b, the CoAl LDH nanosheets are horizontally arranged on the substrate surface without exposure to the magnetic field. As shown in Figure 4.12c,d, the CoAl LDH nanosheets are randomly distributed in the specimen; namely, the surface morphology was out of flatness. On the other hand, in Figure 4.12e,f, the top surface of the CoAl LDH nanosheets show the closely packed nanosheets with vertically arranged on the substrate. The SEM morphologies have also confirmed the XRD results given in Figure 4.11. The results of XRD and SEM indicated the imposed a strong magnetic field contributes greatly to crystal alignment in the CoAl LDH nanosheets prepared by slip casting.

4.4 Conclusion

In summary, we have successfully prepared 2-D CoAl LDH material made of nanosheets by a hydrothermal process. To fabricate CoAl LDH nanosheets with highly aligned crystals, we introduced the method of hydrothermal growth and slip casting with the assistance of an external magnetic field. The following results were obtained:

1. The CoAl LDH nanosheet films were synthesized by a hydrothermal process combined with a strong magnetic field. For the CoAl LDH, the addition of a strong magnetic field has no change the crystal phase, but the obvious reduced the amount of interlayer water molecules in CoAl LDH. The preferred growth orientation of CoAl LDH nanosheets was obtained with the assistance of an external magnetic field.

2. The CoAl LDH nanosheets with highly aligned crystals are achieved by performing a slip casting with the assistance of an external magnetic field. It indicates that the use of a magnetic field is very effective for developing an oriented CoAl LDH nanosheets.

3. The supplemental strong magnetic field provides a novel strategy for developing an oriented microstructure. It's believed that applying an external strong magnetic field in hydrothermal reaction and slip casting could promote the development of layered double hydroxides with prospective application.

Reference

1. Tang, Y.; Chen, Q.; Chen, R., Magnetic field induced controllable self-assembly of maghemite nanocrystals: From 3D arrays to 1D nanochains. *Applied Surface Science* **2015,** *347*, 202-207.
2. Shao, M.; Wei, M.; Evans, D.G.; Duan, X., Magnetic-field-assisted assembly of CoFe layered double hydroxide ultrathin films with enhanced electrochemical behavior and magnetic anisotropy. *Chemical Communications* **2011,** *47* (11), 3171-3173.
3. Sahoo, Y.; Cheon, M.; Wang, S.; Luo, H.; Furlani, E.P.; Prasad, P.N., Field-Directed Self-Assembly of Magnetic Nanoparticles. *The Journal of Physical Chemistry B* **2004,** *108* (11), 3380-3383.
4. Suzuki, T.S.; Sakka, Y.; Kitazawa, K., Orientation amplification of alumina by colloidal filtration in a strong magnetic field and sintering. *Advanced Engineering Materials* **2001,** *3* (7), 490-492.
5. Suzuki, T.S.; Uchikoshi, T.; Sakka, Y., Effect of sintering conditions on microstructure orientation in α-SiC prepared by slip casting in a strong magnetic field. *Journal of the European Ceramic Society* **2010,** *30* (14), 2813-2817.

6. Asai, S.; Sassa, K.S.; Tahashi, M., Crystal orientation of non-magnetic materials by imposition of a high magnetic field. *Science and Technology of Advanced Materials* **2003,** *4* (5), 455-460.
7. Li, S.; Sassa, K.; Asai, S., Fabrication of textured Si_3N_4 ceramics by slip casting in a high magnetic field. *Journal of the American Ceramic Society* **2004,** *87* (7), 1384-1387.
8. Pan, G.X.; Xia, X.H.; Luo, J.S.; Cao, F.; Yang, Z.H.; Fan, H.J., Preparation of CoAl layered double hydroxide nanoflake arrays and their high supercapacitance performance. *Applied Clay Science* **2014,** *102*, 28-32.
9. Zhang, L.; Zhang, X.; Shen, L.; Gao, B.; Hao, L.; Lu, X.; Zhang, F.; Ding, B.; Yuan, C., Enhanced high-current capacitive behavior of graphene/CoAl-layered double hydroxide composites as electrode material for supercapacitors. *Journal of Power Sources* **2012,** *199*, 395-401.
10. Yang, G.; Takei, T.; Yanagida, S.; Kumada, N., Enhanced Supercapacitor Performance Based on CoAl Layered Double Hydroxide-Polyaniline Hybrid Electrodes Manufactured Using Hydrothermal-Electrodeposition Technology. *Molecules* **2019,** *24* (5), 976.
11. Li, F.; Duan, X., Applications of layered double hydroxides. *Layered double hydroxides*, Springer: 2006; pp 193-223.
12. Del Hoyo, C., Layered double hydroxides and human health: an overview. *Applied Clay Science* **2007,** *36* (1-3), 103-121.
13. He, J.; Wei, M.; Li, B.; Kang, Y.; Evans, D.G.; Duan, X., Preparation of layered double hydroxides. *Layered double hydroxides*, Springer: 2006; pp 89-119.
14. Suzuki, T.S.; Uchikoshi, T.; Sakka, Y., Effect of sintering additive on crystallographic orientation in AlN prepared by slip casting in a strong magnetic field. *Journal of the European Ceramic Society* **2009,** *29* (12), 2627-2633.
15. Kloprogge, J.T.; Hickey, L.; Frost, R.L., FT-Raman and FT-IR spectroscopic study of synthetic Mg/Zn/Al-hydrotalcites. *Journal of Raman Spectroscopy* **2004,** *35* (11), 967-974.
16. Xiao, Y.; Su, D.; Wang, X.; Wu, S.; Zhou, L.; Sun, Z.; Wang, Z.; Fang, S.; Li, F., Ultrahigh energy density and stable supercapacitor with 2D NiCoAl Layered double hydroxide. *Electrochimica Acta* **2017,** *253*, 324-332.
17. Fan, G.; Wang, H.; Xiang, X.; Li, F., Co-Al mixed metal oxides/carbon nanotubes nanocomposite prepared via a precursor route and enhanced catalytic property. *Journal of Solid State Chemistry* **2013,** *197*, 14-22.
18. Fan, G.; Wang, H.; Xiang, X.; Li, F., Co-Al mixed metal oxides/carbon nanotubes nanocomposite prepared via a precursor route and enhanced catalytic property. *Journal of Solid State Chemistry* **2013,** *197*, 14-22.

19. Xiao, Y.; Su, D.; Wang, X.; Wu, S.; Zhou, L.; Sun, Z.; Wang, Z.; Fang, S.; Li, F., Ultrahigh energy density and stable supercapacitor with 2D NiCoAl Layered double hydroxide. *Electrochimica Acta* **2017,** *253*, 324-332.
20. Guo, X.; Xu, S.; Zhao, L.; Lu, W.; Zhang, F.; Evans, D.G.; Duan, X., One-step hydrothermal crystallization of a layered double hydroxide/alumina bilayer film on aluminum and its corrosion resistance properties. *Langmuir* **2009,** *25* (17), 9894-9897.
21. Guo, X.; Zhang, F.; Xu, S.; Evans, D.G.; Duan, X., Preparation of layered double hydroxide films with different orientations on the opposite sides of a glass substrate by in situ hydrothermal crystallization. *Chemical Communications* **2009,** (44), 6836-6838.
22. Huang, S.; Zhu, G.N.; Zhang, C.; Tjiu, W.W.; Xia, Y.Y.; Liu, T., Immobilization of Co-Al layered double hydroxides on graphene oxide nanosheets: growth mechanism and supercapacitor studies. *ACS applied materials & interfaces* **2012,** *4* (4), 2242-2249.
23. Lü, Z.; Zhang, F.; Lei, X.; Yang, L.; Evans, D.G.; Duan, X., Microstructure-controlled synthesis of oriented layered double hydroxide thin films: Effect of varying the preparation conditions and a kinetic and mechanistic study of film formation. *Chemical Engineering Science* **2007,** *62* (21), 6069-6075.
24. Van der Drift, A., Evolutionary selection, a principle governing growth orientation in vapour-deposited layers. *Philips Res. Rep* **1967,** *22* (3), 267.
25. Khan, A. I.; O'Hare, D., Intercalation chemistry of layered double hydroxides: recent developments and applications. Journal of Materials Chemistry **2002**, *12* (11), 3191-3198.
26. Miyata, S., The Syntheses of Hydrotalcite-Like Compounds and Their Structures and Physico-Chemical Properties-I: the Systems Mg^{2+}-Al^{3+}-NO^{3-}, Mg^{2+}-Al^{3+}-Cl^{-}, Mg^{2+}-Al^{3+}-ClO^{4-}, Ni^{2+}-Al^{3+}-Cl^{-} and Zn^{2+}-Al^{3+}-Cl^{-}. *Clays and Clay Minerals* **1975**, *23* (5), 369-375.
27. Pesic, L.; Salipurovic, S.; Markovic, V.; Vucelic, D.; Kagunya, W.; Jones, W., Thermal characteristics of a synthetic hydrotalcite-like material. *Journal of Materials Chemistry* **1992**, *2* (10), 1069-1073.
28. Marcelin, G.; Stockhausen, N.; Post, J.; Schutz, A., Dynamics and ordering of intercalated water in layered metal hydroxides. *The Journal of Physical Chemistry* **1989**, *93* (11), 4646-4650.
29. Brindley, G.; Kikkawa, S., A crystal-chemical study of Mg, Al and Ni, N hydroxy-perchlorates and hydroxycarbonates. *American Mineralogist* **1979**, *64* (7-8), 836-843.
30. Brindley, G.; Kikkawa, S., Thermal behavior of hydrotalcite and of anion-exchanged forms of hydrotalcite. *Clays and Clay Minerals* **1980**, *28* (2), 87-91.

Chapter 5 High-Performance Energy Storage Based on Hexagonal Tungsten Oxide-Polyaniline Hybrid Electrodes via Hydrothermal-Electrodeposition Route

5.1 Introduction

With the worsening depletion of energy resources and global warming, the required development of sustainable and renewable clean energy technology has urgent demand for energy storage devices. Supercapacitors (SCs), as an effective energy storage device, have gained enormous attention due to their high power density and power output, fast charge-discharge capability, and long life time [1-2]. Based on their energy storage mechanism, SCs can be classified into electrical double layer capacitors (EDLCs) and pseudocapacitors (or faradaic capacitors), which have the potential to achieve higher specific capacitance and higher energy storage compared to EDLCs [3-4]. The electrode material is the source of the electrochemical properties in SCs [5]. At this stage, there are two main categories of faradaic electrode materials: transition metal oxides/metal chalcogenides and conductive polymers [6].

Due to their mechanical stability, nanometer-size, electron transport, and pseudocapacitive properties, conductive polymer/transition metal oxide composites have, in recent years, attracted worldwide attention. Conducting polymers as electrode materials have drawn great interest for energy storage [5]. Among the various conducting polymers, polyaniline (PANI) has been considered as one of the most promising pseudocapacitor materials, because of its high specific capacitance, excellent electrical conductivity, easy preparation and low cost [7-8]. However, PANI suffers from poor cycling stability, because the PANI structure suffers from a large degree of volumetric swelling and shrinking, which is caused by the repeated insertion/ de-insertion of electrolyte ions during the doping/dedoping process [9-10]. To overcome this shortcoming, PANI modified with transition metal oxide has aroused considerable interest due to the synergistic effects of each component. Owing to its large specific surface area, electrochemical stability and eco-friendly nature, tungsten oxide (WO_3) has, in recent years, received increasing attention as a promising SC electrode material [11-13]. Nevertheless, the insufficient capacitance of WO_3 still remains a major obstacle for pseudocapacitor applications. Much work so far has focused on WO_3/PANI composites, with the aim of improving the specific capacitance and cycling stability. Zou et al. prepared a WO_3/PANI electrode by the electrochemical co-deposition, and it showed a capacitance of 168 F/g at 1.28 mA/cm^2 [14]. Even so, the capacity degradation of about 40% within one thousand cycles meant that this composite could not meet with the requirements for practical application. Samu et al. electrochemically synthesized WO_3/PANI hybrid nanostructure films by a two-step electrochemical protocol, and the best capacitance obtained was 200 mF/cm^2 at a charging-discharging current of 0.4 mA [15]. However, its capacitance performance and cycling stability were also not ideal. Wei et al. prepared PANI/WO_3 nanocomposite films by electrodeposition of PANI onto WO_3 films for electrochromic application [16]. Unfortunately, this composite did not show good capacitive properties. The electrochemical preparation strategy has advantage on achieving higher filling ratio in the nanostructured material [17]. Nonetheless, the electrosynthesis of WO_3 was generally found to be limited in the formation of a high loading thin film on flat substrates, which occurred as a result of the weak substrate-deposit interaction, undesired gas evolution, high resistance, and insufficient mass transport to the working electrode surface [18-19]. Moreover, an important requirement for one step co-deposition is the alignment of the potential windows for the deposition of PANI and metal oxide, which is a grand challenge in the universality of the synthesis [20]. It is commonly known that the electrochemical performance is closely associated with the nanostructure and morphology of active materials. For instance, the nanostructured porous materials may facilitate ionic motion, improve the rate capability, and increase the utilization of electrode materials. The hydrothermal reaction is a facile, cost-effective synthetic route to fabricate WO_3 with a variety of nanostructure morphologies. Among the various crystal structures of WO_3, the hexagonal tungsten oxide (h-WO_3) is the most desirable and promising material for a pseudocapacitive electrode. The multiple voids of h-WO_3, such as the hexagonal window, trigonal cavity, and four-coordinated square window, are beneficial for the insertion of a large number of guest ions, which could effectively increase the storage capacity [21]. Here, the hydrothermal synthesis of h-WO_3 also avoids the use of binders, which can even damage the nanostructures, and this strategy is also advantageous to produce porous nanostructures. In contrast with previously published articles, we fabricated a binder-free h-WO_3 electrode with a well-designed nanostructure, which revealed a large specific surface, fast ionic diffusion, and excellent mechanical stability by means of a hydrothermal method. The WO_3-PANI electrode was prepared by directly growing nanowires on the substrate followed by electrodepositing PANI on the nanoarchitectured WO_3.

Herein, we discuss the design and fabrication of novel inner/outer layer structural WO_3-PANI hybrid films via a hydrothermal-electrodeposition route and used them as electrodes for high-performance pseudocapacitors that address both the capacitance and cycling stability issues. The advantage of the inner/outer layer structure lies in the presence of the void spaces in the porous h-WO_3 interior to accommodate the volumetric expansion of PANI during long-term cycling, thus preserving the structural integrity of the outer PANI while maximizing the electrolyte ion diffusion and reversible redox process. Electrochemical measurements confirmed that this unique structure has excellent specific capacitance, good rate performance, and stable cycling performance. The fabricated WO_3-PANI-based all-solid-state symmetric supercapacitor exhibited remarkable flexibility and good electrochemical performances, and thus is potentially useful in flexible energy storage devices.

5.2 Materials and Methods

5.2.1 Synthesis of WO_3 nanowire thin films on Ti substrate

All chemical reagents used in the experiment were analytical grade. The WO_3 was synthesized by a simple hydrothermal method. In a typical synthesis process, $Na_2WO_4 \cdot 2H_2O$ (6.25 mmol) was put into 50 mL deionized water under 20 min magnetic stirring. Subsequently, a 2 M HCl aqueous solution was dropwise added into the solution to generate a white precipitate solution and stirred by use of a magnetic stirrer until the solution became transparent (adjusting the pH to 1.2). Then, $H_2C_2O_4$ (17.5 mmol) was added into the above mixture and diluted to 125 mL. Then, $(NH_4)_2SO_4$ (47.7 mmol) was added into the above mixture. The mixed solution was stirred for 30 min and then transferred (30 mL) to an autoclave with a Teflon lining (50 mL). A clean titanium (Ti) plate (50 mm × 10 mm × 0.1 mm) was immersed in the reaction solution. The autoclave was sealed and heated at 180 °C for 16 h, subsequently cooled to room temperature. Finally, the sample was collected from the solution and washed with distilled water several times. The sample was then dried at 50 °C for 6 h. The mass loading of WO_3 on the Ti substrate was measured with an analytical microbalance, and the mass loading was about 3.2 mg/cm^2.

5.2.2 Synthesis of WO_3-PANI hybrid nanostructured films

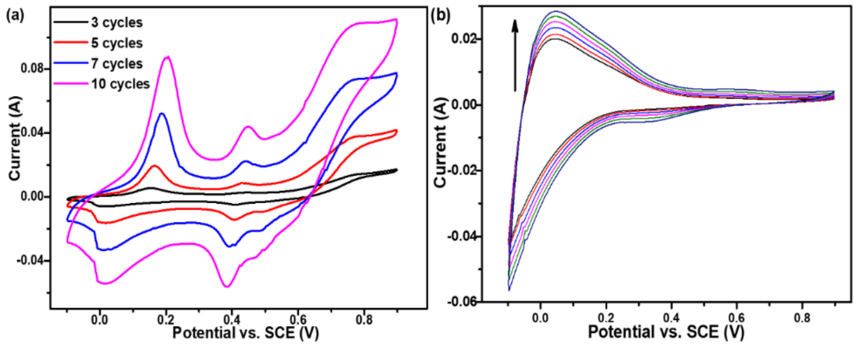

Figure 5.1. Electropolymerization synthesis of PANI onto (a) bare Ti surface and (b) WO_3 sample supported on the Ti substrate at a scan rate of 20 mV/s in a solution of 0.5 M aniline in 0.5 M H_2SO_4.

Hybridization with polymer PANI was carried out by cyclic voltammetry (CV) technique in an aqueous medium (0.15 M aniline + 0.5 M H_2SO_4) (Figure 5.1a). CV experiments were performed to deposit PANI on the surface of the WO_3 within the potential between -0.1 and 0.9 V versus SCE in a three-electrode electrochemical cell, with WO_3 grown on Ti plate as the working electrode, a saturated calomel electrode (SCE) as the reference electrode, and a Pt plate as the counter electrode (Figure 5.1b). The total mass of the PANI coating can be controlled by changing the number of CV scan cycles. After deposition, these as-prepared WO_3-PANI electrodes were carefully washed with distilled water several times to remove the solvent and dried at 50 °C for 6 h. Finally, the mass loading of PANI was measured by the weight difference before and after electrodeposition.

5.2.3 Fabrication of all-solid-state symmetric supercapacitors

The polyvinyl alcohol/H_2SO_4 (PVA/H_2SO_4) electrolyte was prepared as follows: 5 g of PVA powder (molecular weight: 65 000-70 000 g/mol) was put into 50 mL of 1.0 M H_2SO_4 solution. The mixture solution was conducted at 85 °C during constant stirring until a jelly-like solution formed. Subsequently, two Ti substrate/WO_3-PANI electrodes were immersed into the PVA/H_2SO_4 electrolyte for 5 min to allow the electrolyte to diffuse into the nanoporous structure. Finally, after vaporizing the excess water of the WO_3-PANI electrodes, the two identical WO_3-PANI electrodes were pressed together to conduct the electrochemical measurement.

5.2.4. Structural characterization, theoretical calculation, and electrochemical measurement

The morphologies of the products were characterized by field emission scanning electron microscopy (FESEM, JSM-6500F, JEOL, Ltd.) equipped with EDX analyzer. The molecular structure and crystal phase of the products were examined by Fourier transform infrared spectrometer (FTIR, FTIR4100, JASCO Corp.) and X-ray diffraction obtained on an X-ray diffractometer with monochromated Cu Kα radiation (XRD, RINT-2100, Rigaku Corp.). Synchrotron X-ray diffraction (SXRD) test in this study was carried out at SPring-8, BL02B2. The chemical composition of the products was examined using X-ray photoelectron spectroscopy (XPS, AXIS Ultra DLD, Kratos Analytical Ltd.). The band structure and density of states (DOS) curves of the WO_3 crystals were calculated by use of the Vienna Ab Initio Simulation Package (VASP 5.3) [22-23]. The DOS curves for PANI molecules were calculated by DV-Xα simulation [24].

The electrochemical measurements were carried out by use of an HZ 7000 electrochemical workstation (Hokuto Denko) in a three-electrode mode with 1 M H_2SO_4 as the electrolyte. A Pt plate was used as the counter electrode and a SCE as the reference electrode. The WO_3, PANI, and WO_3-PANI samples supported on Ti substrates were used as the working electrodes. CV and galvanostatic charge-discharge (GCD) curves were measured between -0.38 to 0.7 V. Electrochemical impedance spectroscopy (EIS) measurements were performed at a frequency range from 0.01 Hz to 100 kHz with an AC amplitude of 5 mV at 0 V. The calculation equations of the electrochemical performance of as-prepared samples were illustrated in the Supporting Information.

The gravimetric specific capacitance values (C_g) were calculated from the GCD curves according to equation (1):

$$C_g = \frac{2i\int Vdt}{m(V_h^2 - V_l^2)} \tag{1}$$

where i is the discharge current; $\int Vdt$ is the integral current area; m is the mass of active material; V_h and V_l represent the high and low potential values.

Furthermore, according to equation (1), the areal specific capacitance (C_a) derived from GCD curves can be calculated using the following equation (2):

$$C_a = \frac{2i\int Vdt}{S(V_h^2 - V_l^2)} \tag{2}$$

where S is the apparent area of active material.

The energy density and power density were calculated using equations (3) and (4), respectively: [25-26]

$$E = \frac{C_a V^2}{2\times 3.6} \tag{3}$$

$$P = \frac{E\times 3600}{\Delta t} \tag{4}$$

where E is the specific energy density; P is the specific power density; C_a represents the areal specific capacitance; V is the potential window; Δt is the discharge time.

5.3 Results and Discussion

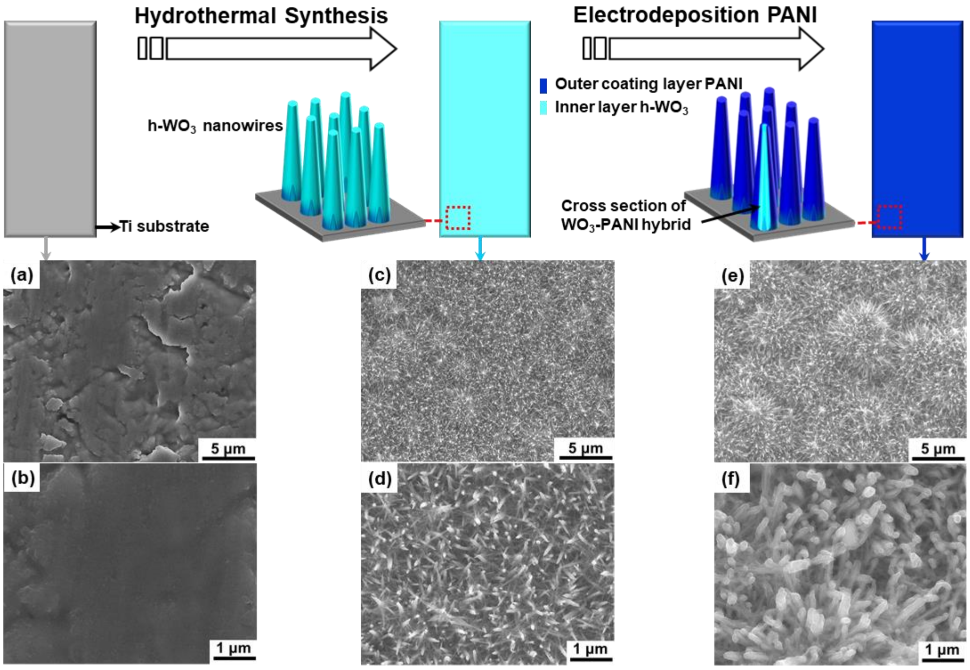

Figure 5.2. Schematic illustration of the two-step preparation of WO_3-PANI hybrid electrode and FESEM images of (a,b) the Ti substrate surface, (c,d) after covering with WO_3, and (e,f) after electropolymerization of aniline.

5.3.1 Structural study

The two-step fabrication process of the inner/outer coating structured WO_3-PANI hybrid electrode is illustrated in Figure 5.2. Firstly, after the homogeneous hydrothermal process, the WO_3 nanowires can grow directly on the Ti substrate as a binder-free electrode. The FESEM reveals that WO_3 nanowires are well distributed across the surface, forming a porous structure (Figure 5.2c,d). Secondly, the conductive PANI-coated WO_3 could be obtained through electropolymerization of aniline monomers. The electropolymerization process of aniline are presented in Figure 5.1. As illustrated in Figure 5.2e,f, the nanowires become larger in diameter after the PANI layer was deposited, without altering the underlying structure of the WO_3. Moreover, the morphologies of WO_3-PANI obtained at different CV scan cycles were further observed by FESEM (Figure 5.3). With increasing number of CV cycles, as presented in Figure 5.3b-f, it was demonstrated that the thickness of the PANI layer on the WO_3 nanowire surface increased gradually, and the mass of the PANI coating layer increased accordingly. Hence, the CV technique was appropriate to prepare WO_3 nanowires wrapped with a PANI coating layer.

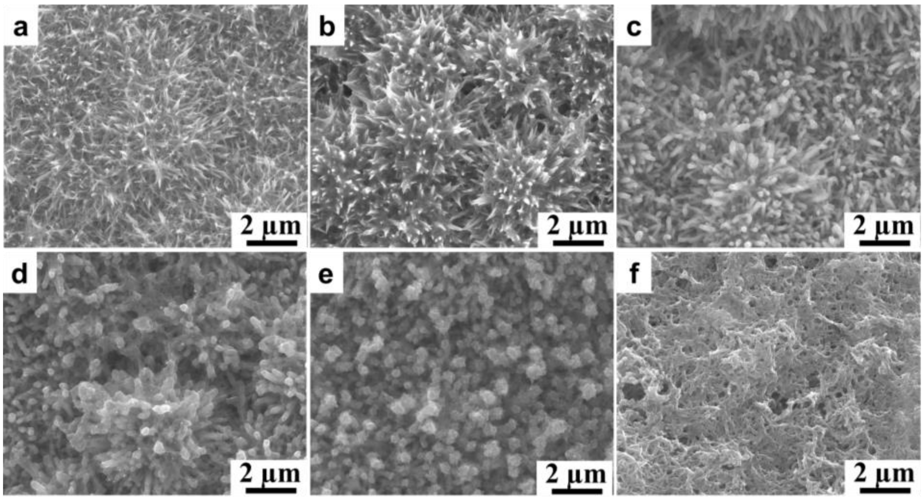

Figure 5.3. FESEM images of (a-f) the WO_3-PANI obtained by CV scan for various cycles: (a) 0 cycles, (b) 5 cycles, (c)10 cycles, (d) 15 cycles, (e) 20 cycles, (f) 30 cycles at a scan rate of 20 mV/s.

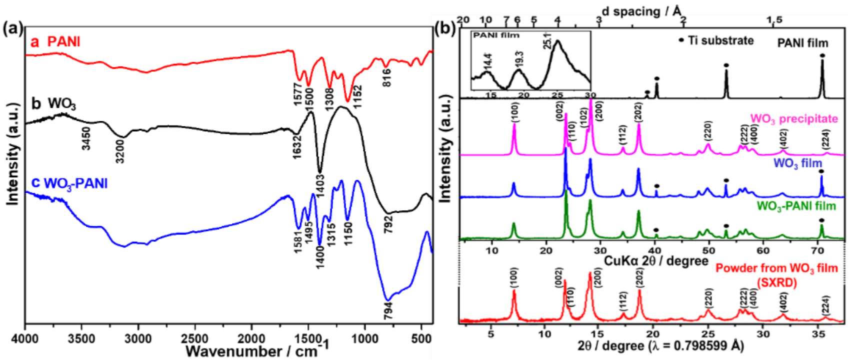

Figure 5.4. (a) FT-IR spectra of PANI, WO_3, and WO_3-PANI films. (b) XRD patterns of PANI film, WO_3 precipitate, WO_3 film, WO_3-PANI film, and SXRD patterns of the powder obtained from WO_3 film.

The molecular structure and crystal phase of PANI, WO_3, and WO_3-PANI were investigated by FT-IR spectroscopy and XRD. As detailed in Figure 5.4a, the FT-IR spectrum of the PANI is consistent with previously reported results [27]. Regarding the spectrum for the WO_3 in Figure 5.4a, the broad band in the 3400-3500 cm^{-1} range and peak at 1632 cm^{-1} can be explained as the O-H stretching and bending modes, respectively, due to the presence of coordinated water molecules in hydrated WO_3. The strong broad bands in the 800 to 600 cm^{-1} range are ascribed to the stretching mode of W-O-W and O-W-O bonds [28-29]. The bands at 3200 and 1403 cm^{-1} can be assigned as the stretching mode of N-H, associated with NH_4^+ cations [30]. No other ionic species (e.g. SO_4^{2-}) was detected in the spectrum, which indicated that the ammonium sulfate additive was wholly removed by washing with distilled water. The present results differ from those reported in previous literature [31-32]. In fact, in contrast with what was previously viewed, we deem that ammonium ions are needed in the hexagonal channels to maintain the WO_3 structure during the hydrothermal synthesis. Our views are also somewhat similar to those of Kovács et al.[33], in which it was found that Na$^+$ ions situated in the hexagonal channels helped to stabilize the metastable structure of WO_3. After the WO_3 modification with PANI, the intensity of the WO_3 peaks decreased, and several new characteristic peaks appeared at 1581, 1495, 1315 and 1150 cm^{-1}; these peaks are associated with PANI, which demonstrates the combination of PANI with the WO_3.

The crystallographic phases of the as-synthesized samples were further confirmed by XRD (Figure 5.4b). The XRD patterns of the WO_3 precipitate and WO_3 film, except the one marked with black dot mark star coming from the Ti substrate, can be well matched with a typical hexagonal phase of WO_3 (JCPDS card: 85-2460) [34-35]. Furthermore, the diffraction peaks of the WO_3 film were sharp and intense, indicative of its well-crystallized character. Compared with the WO_3 precipitate sample, the (002) peak intensity for the WO_3 film was larger. Such a difference may result from the crystal growth of WO_3 nanowires preferentially grown along the c-axis orientation. The film sample was also characterized by SXRD. By calculating the interplanar spacing of the diffraction spectrum for WO_3, the results indicated that the diffraction peaks of the WO_3 precipitate and powder were well matched. This result further confirmed that WO_3 crystallites were able to grow well on the substrate surface. The presence of PANI in the WO_3-PANI was also evaluated by XRD. The pure PANI shows three very weak and broad peaks reflections at 2θ = 14.4°, 19.3° and 25.1°, which revealed that PANI is only partially crystalline [36-37]. The pattern of the WO_3-PANI film showed well-matched peaks to those of WO_3 film, except that the peak intensities were clearly decreased, which can be attributed to the surface of the WO_3 being covered with PANI. Based on this result, the XRD diffraction peaks of WO_3-PANI film were found to be unchanged, being nearly identical with those for the WO_3 film.

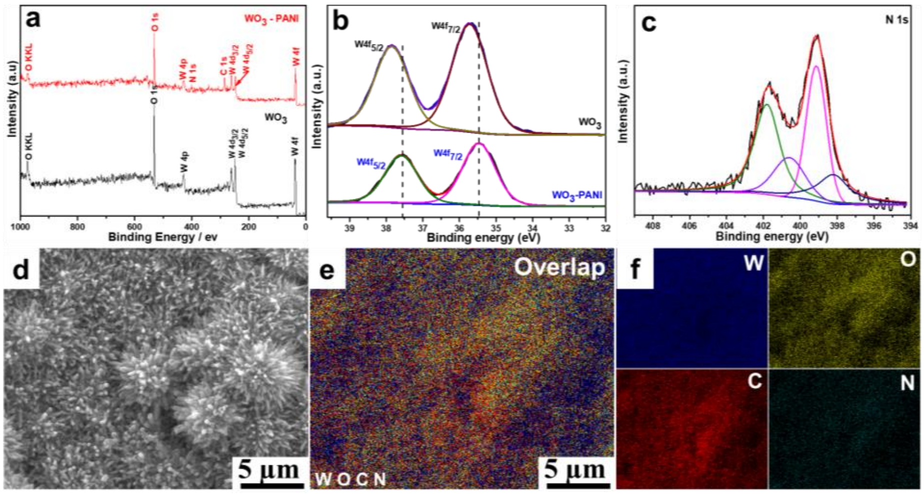

Figure 5.5. (a) XPS full spectra and (b) W 4f spectra of WO_3 and WO_3-PANI. (c) N 1s spectrum of WO_3-PANI. (d-f) FESEM image of WO_3-PANI corresponding to the EDX elemental mapping images of W, O, C, and N showing uniform distribution of the elements.

The surface elemental composition and valence states of the pristine WO_3 and WO_3-PANI samples were examined by XPS, and the element distributions were examined by EDX. As shown in Figure 5.5a, the full XPS spectrum of WO_3 indicates the presence of W and O, while the presence of the C 1s and N 1s peaks in the WO_3-PANI spectra imply that the WO_3 was successfully hybridized with PANI. As shown in Figure 5.5b, the W 4f line of WO_3 can be deconvoluted into two peaks at 37.84 eV and 35.72 eV, corresponding to W $4f_{5/2}$ and W $4f_{7/2}$ (resulting from spin-orbit splitting) that belong to the W^{6+} state in WO_3 [38-39]. After PANI was deposited, the W 4f peaks of the WO_3-PANI hybrid were shifted to lower binding energy (35.45 eV and 37.57 eV). The shift in the binding energies of the W 4f peak positions reveal the interactions between the WO_3 and PANI layers. The N 1s spectrum of the WO_3-PANI hybrid in Figure 5.5c clearly shows two peaks. The first peak at 401.79 eV can be attributed uniquely to N in the NH_4^+ ion, which further confirms the correlation between the NH_4^+ ion and the structure of h-WO_3 [40]. This result is also in accord with the FTIR analysis. The second peak can be deconvoluted into three peaks at different binding energies: 398.21 eV (-N=), 399.15 eV (-NH-) and 400.62 eV (-NH^+-), which is consistent with previous reports [41-42]. As shown in Figure 5.5d-f, the EDX analysis displays homogeneously distributed elements, W, O, C, and N, which implies that the WO_3-PANI was well distributed across the Ti surface. Furthermore, the superposition image in Figure 5.5e reveals that C and N elements were evenly decorated on the nanowires, providing visual evidence that the PANI was uniformly coated, resulting in a uniform WO_3-PANI inner/outer coating nanostructures.

5.3.2 Growth process and mechanism of WO_3 nanowire films on Ti surface

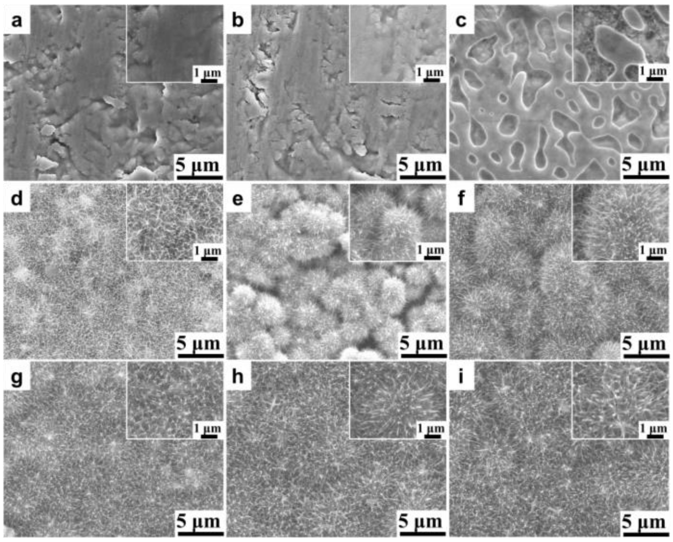

Figure 5.6. FESEM images of the products obtained on Ti substrate at various hydrothermal reaction times: (a) 0 h, (b) 2 h, (c) 4 h, (d) 6 h, (e) 8 h, (f) 10 h, (g) 14 h, (h) 16 h, (i) 18 h.

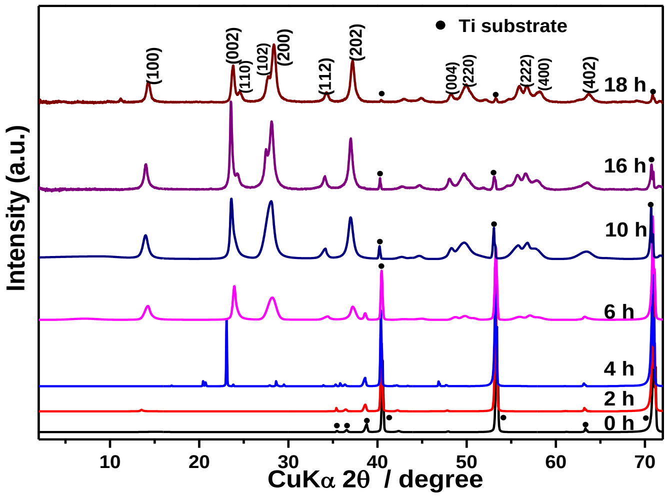

Figure 5.7. XRD patterns of the products obtained on Ti substrate at various hydrothermal reaction times: 0 h, 2 h, 3 h, 4 h, 6 h, 10 h, 14 h, 16 h, 18 h.

To analysis the growth mechanism of the WO_3 nanowires, the Ti substrate was removed from the autoclave after varying hydrothermal reaction times. Before the hydrothermal reaction, it can be seen from Figure 5.6a that the surface of the pretreated Ti substrate was uneven due to polishing with sandpaper; this was the morphology of the bare Ti substrate surface prior to coating. From Figure 5.6b-c, it can be observed that massive nanoparticles were deposited and tended to form a thin layer on the substrate surface, which was uniformly covered by the layer of thin film. From Figure 5.6d-e, it can be seen that there was a large generation of intermediate microspheres growing on the thin film layer, and it is not difficult to find that these microsphere agglomerates are formed of large numbers of nanowires. From Figure 5.6f-g, with increasing reaction time, the diameter of the microspheres became larger, and the nanowire structure became clear. With the time increasing to 16 h, the microspheres were connected to each other because of the growth of the fibrous nanoparticles, resulting in the fact that the intermediate microspheres have seemingly disappeared into the new fiber membrane as shown in Figures 5.6h and 5.6i.

Figure 5.7 shows the XRD patterns of the products grown on Ti plate at varying hydrothermal reaction times. It was found that there was no obvious WO_3 characteristic diffraction peak from 0 h to 4 h. With increasing reaction time from 6 h to 10 h, the peaks of WO_3 appeared, and the diffraction peaks of the Ti substrate were further weakened. Further prolonging the time from 16 h to 18 h, the diffraction peaks of WO_3 became sharper and stronger, while the peaks of Ti nearly disappeared. The diffraction peaks were well-indexed to the h-WO_3 structure (JCPDS card: 85-2460). The results of the SEM images and XRD patterns of the hydrothermal products at various reaction times support each other.

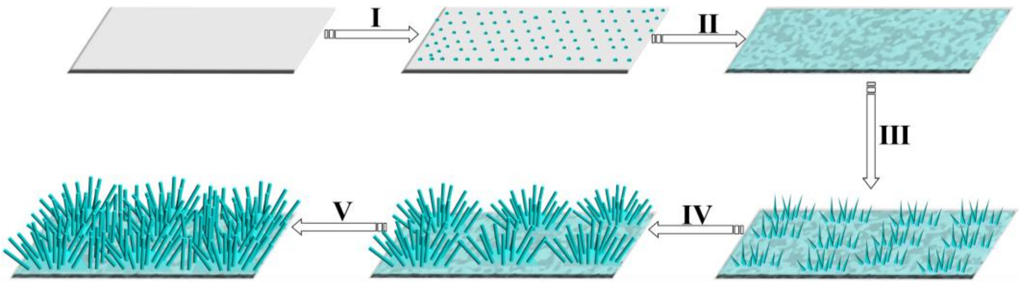

Figure 5.8. Schematic illustration of growth mechanism of WO_3 nanowire film.

Combined with the FESEM images and XRD patterns (Figures 5.6 and 5.7) analyses of the WO_3 obtained at the different hydrothermal reaction times, the growth mechanism of WO_3 nanostructures is shown in Figure 5.8. The formation process of the WO_3 films on the Ti substrate included both crystal nucleation and growth. It is well known that, compared to homogeneous nucleation in solution, heterogeneous nucleation (e.g., onto a metal surface) is usually more favorable. In the initial stage, uneven surfaces could provide bonding sites for the hetero-nucleation of crystallites (stage I). When the hydrothermal time is prolonged, small crystallites will undergo self-aggregation, and then the substrate surface can gradually be covered by a seed layer thin film (stage II). With further increase of the hydrothermal time, the WO_3 nanowires initially formed with the nuclei enter a fast growth (stage III-IV). Both the length and diameter of these nanowires became larger with increasing hydrothermal reaction time. As illustrated in Figure 5.6e, the growth of the seed layer film is not very uniform, so the aggregated nucleus can easily form a sphere. For each sphere, the size and number of nuclei varied to some extent. In the final stage, when the size of the nanowire sphere rose to a degree, fast growth occurred between the microspheres, causing the gap between the microspheres to disappear. The WO_3 nanowires grew outwards from the substrate because of spatial competition (stage V), and the morphologies of the nanowires were not significantly changed when further prolonging the hydrothermal reaction time.

5.3.3 Electrochemical performance

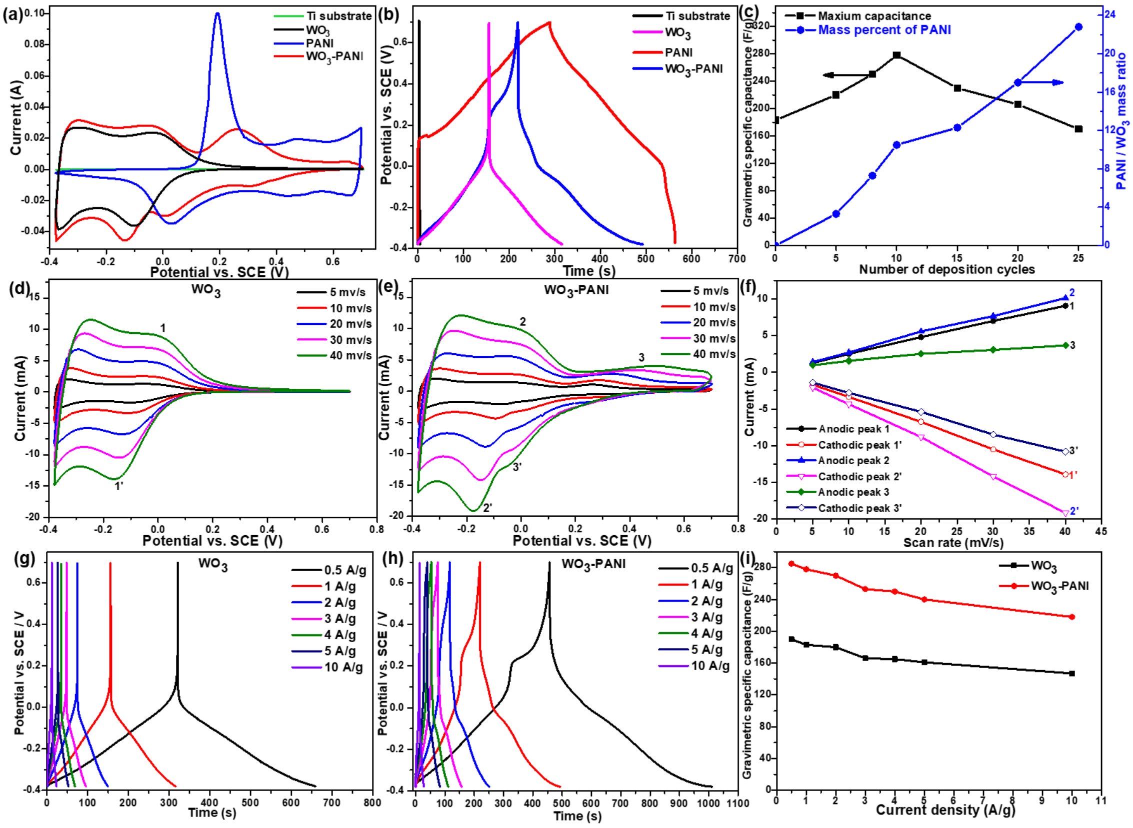

Figure 5.9. Electrochemical performance of the Ti substrate, WO_3, PANI, and WO_3-PANI hybrid. (a) CV curves at a scan rate of 10 mV/s. (b) GCD curves at a current density of 1 A/g; (c) The gravimetric specific capacitance (obtained from GCD measurement) and the mass ratio of PANI/WO_3 versus the number of deposition cycles; (d,e) CV curves at different scan rates; (f) The linear dependence of anodic and cathodic peak currents versus scan rate; (g,h) GCD curves at different current densities. (i) The gravimetric specific capacitance versus current density.

The electrochemical studies for the as-prepared electrodes were conducted in a three-electrode system in 1 M H_2SO_4 aqueous electrolyte. Figure 5.9a shows the CV curves of Ti substrate, PANI, WO_3, and WO_3-PANI. The CV curve of the Ti substrate indicates that the substrate contributed little to the total capacitance of the electrode. Regarding the PANI electrode, the CV curve possesses three redox couples, which can be explained by reaction equation (1). There are two couples of redox peaks situated at 0.22/0.07 V and 0.7/0.66 V, corresponding to the transformation of the leucoemeraldine-emeraldine form and emeraldine-pernigraniline form. Another pair of redox peaks located at 0.45/0.42 V correspond to the overoxidation products or degradation of PANI [43-44]. It should be noted that only the emeraldine base can achieve highly conductive by protonic acid doping, as shown in equation (2). The CV curve of the WO_3 electrode possesses one redox couple with peaks located at -0.01/-0.10 V, corresponding to the intercalation/deintercalation of protons, respectively [45]. It can be expressed as equation (3).

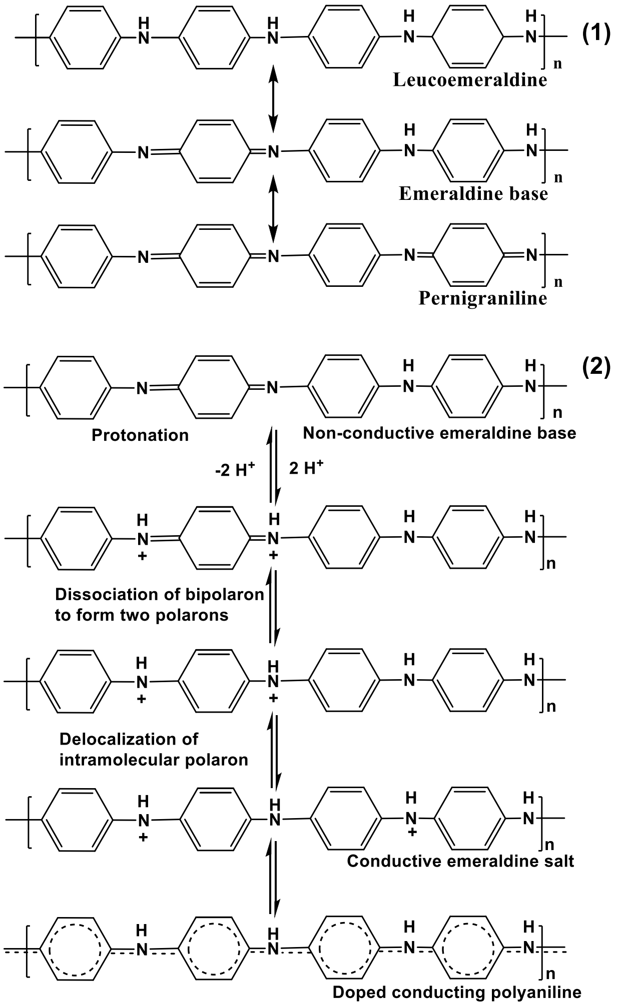

$$WO_3 + xH^+ + xe^- \longleftrightarrow H_xWO_3 \qquad (3)$$

For the WO_3-PANI electrode, the CV curve possesses typical characteristic redox peaks of WO_3 (-0.01/-0.10 V) and PANI (0.26/0.01 V), which reveals that the hybrid electrode possesses characteristics of both components. With the increase in the concentration of the sulfuric acid electrolyte (0.5 to 5 M), the anodic and cathodic peaks of WO_3 and WO_3-PANI were shifted to higher and lower potentials, indicating that high H^+ ion concentration can accelerate the redox reaction (Figure 5.10). The hybrid electrode is beneficial for the fact that the pseudocapacitive contribution to the overall capacitance can be expected in the whole potential window. Compared with WO_3 and PANI electrodes, an increase in the CV area of the hybrid electrode is observed and the potential responses window can be greatly extended to 1.08 V, indicating that the hybrid electrode has the potential to achieve higher capacitance and energy density.

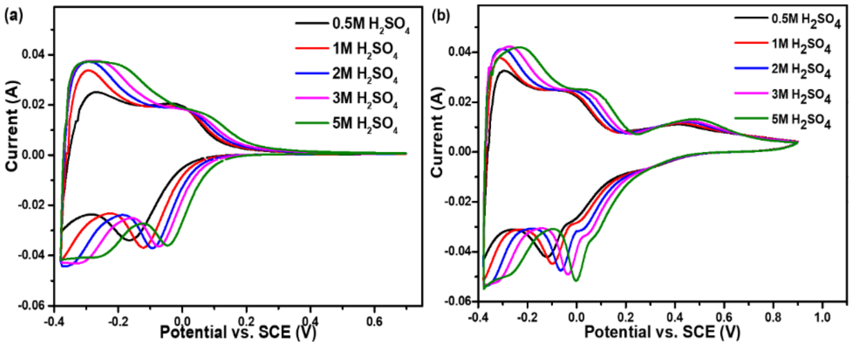

Figure 5.10. CV curves of the WO_3 and WO_3-PANI for various H_2SO_4 concentrations at a scan rate of 10 mV/s.

Figure 5.9b shows the GCD curves of the as-prepared electrodes at a current density of 1 A/g. The gravimetric specific capacitance of the pristine PANI electrode was calculated to be 350 F/g, which proves that PANI has a very high gravimetric specific capacitance at the initial cycle. For the PANI electrode, its excellent pseudocapacitive charge storage was implemented by reversible redox processes. During the charging process (oxidation reaction), PANI became a polycation, and then electrolyte anions (SO_4^{2-}) were intercalated into the PANI backbone for electroneutrality with the release of electrons. Conversely, the discharging process was associated with a reduction reaction. The process for PANI charge-discharge in the sulfuric acid electrolyte (p-doping) can be explained by equation (4). The gravimetric specific capacitance of WO_3-PANI obtained by 10 deposition cycles was calculated to be 278 F/g, which is higher than that of the pristine WO_3 (183 F/g). Figure 5.9c shows the gravimetric specific capacitance and the mass ratio of PANI/WO_3 versus the number of deposition cycles. With increasing the number of deposition cycles, the gravimetric specific capacitance of WO_3-PANI increased at first to a maximum (278 F/g) and then decreased upon further prolonged deposition. This result indicates that the enhanced gravimetric specific capacitance of the WO_3-PANI hybrid depends heavily on the loading mass ratio of PANI and WO_3, as well as the connecting mode (van der Waals and hydrogen bonding interactions) between the inner WO_3 and outer PANI layers. Moreover, with increasing deposition mass of PANI, the porous structure of the WO_3 was gradually blocked, which may also hinder the electrolyte ion diffusion into the inner WO_3, thus impeding the reaction with WO_3 and decreasing the capacitance. Thus, a thin PANI layer is desirable. Specifically, we selected 10 electrodeposition cycles (PANI: WO_3 mass ratio of 0.1:1), the WO_3-PANI hybrid, as the optimum electrode for further evaluation of electrochemical performances.

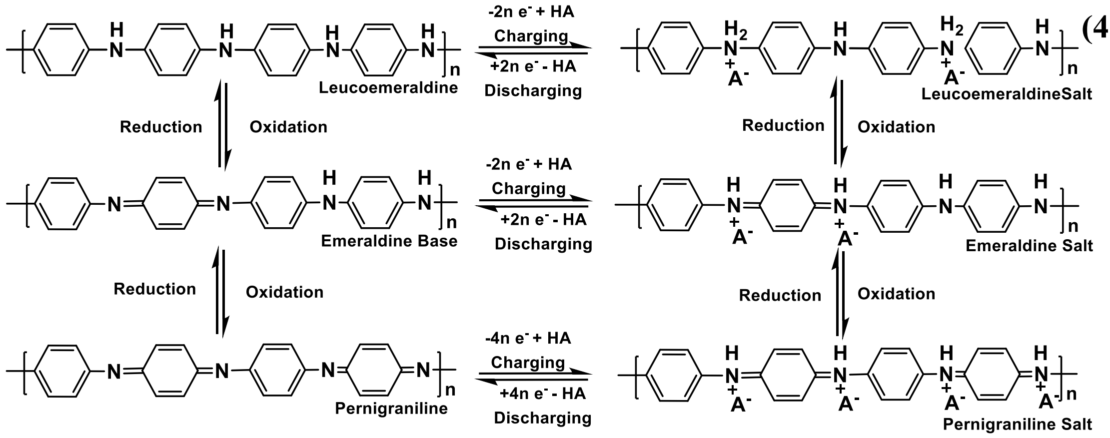

(4)

If we simply assume that there is no interaction between WO_3 and PANI in the hybrid material, the C_g of WO_3-PANI should be the sum of the C_g of WO_3 and PANI. For the WO_3-PANI (PANI: WO_3 mass ratio of 0.1: 1), the C_g can be calculated by the following equation (5).

$$C_{WO_3-PANI} = C_{WO_3}\frac{1}{(1+0.1)} + C_{PANI}\frac{0.1}{(1+0.1)} \qquad (5)$$

Based on the GCD measurements in Figure 5.9b, the practical gravimetric specific capacitance of WO_3 and PANI were 183 and 350 F/g. After calculation by equation (5), the theoretical gravimetric specific capacitance of WO_3-PANI in the hybrid was 198.2 F/g, which is obviously lower than the practical gravimetric specific capacitance of 278 F/g. The results indicate that the synergistic effect plays an important role in increasing the gravimetric specific capacitance. Through theoretical calculation, the enhanced capacitance performance of WO_3-PANI was not only ascribed to the high capacitance of PANI but also the synergistic effect of PANI and WO_3 (see Supporting Information for details). The mass loading for the hybrid electrode showed an average value of 3.52 mg/cm^2. Based on the above analysis, it can be seen that the gravimetric specific capacitance of WO_3-PANI was not linear as a function of PANI mass percent.

Rate capability is one of the crucial factors in the design of SCs. Herein, CV and GCD measurements were conducted to explore the rate capability of the as-prepared electrodes. Figure 5.9d, e shows CV curves of the WO_3 and WO_3-PANI electrodes with varying scan rates. At higher scan rates, the redox peaks retained well-defined shapes, which displayed the good electrochemical reversibility of the WO_3 and WO_3-PANI electrodes. It is also seen in Figure 5.9f that, for the WO_3 and WO_3-PANI electrodes, the nearly linear relationship of the plot of anodic and cathodic peaks (1/1′, 2/2′ and 3/3′) currents versus the scan rate indicates that the redox reaction is surface controlled, which also revealed the pseudocapacitive behavior of both electrodes [46]. Figure 5.9g, h presents GCD curves of WO_3 and WO_3-PANI electrodes at various current densities. With increasing current density, the charging-discharging time gradually decreased. The gravimetric specific capacitances of the WO_3 and the WO_3-PANI hybrid were 190 and 285 F/g at 0.5 A/g. The WO_3 and WO_3-PANI hybrid still presented values of 147 and 220 F/g at 10 A/g, and the corresponding capacitance retention ratios were 77.4 and 77.2%, respectively, indicating that the hybrid electrode has both high gravimetric capacitance and good rate performance. The above data, combining CV with GCD studies, demonstrate the favorable electrochemical reversibility and rate capability behavior of the WO_3-PANI hybrid electrode.

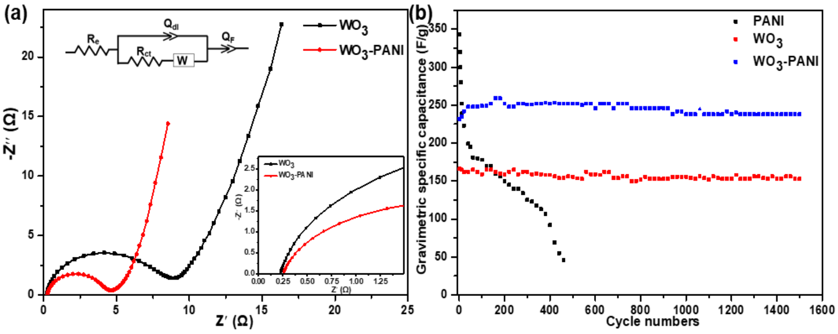

Figure 5.11. (a) Nyquist plots of the WO_3 and WO_3-PANI. (b) Cycling performance of the PANI, WO_3, and WO_3-PANI at a current density of 3 A/g, respectively.

EIS measurements were performed to evaluate the electron transfer and ion diffusion in the electrode/electrolyte system. The Nyquist plots of the WO_3 and WO_3-PANI electrodes (Figure 5.11a), which consisted of a semicircle in high frequency and an inclined straight line in low-frequency, were analyzed using the equivalent circuit given in the inset of Figure 5.11. R_e is the equivalent series resistance, including the ionic resistance of the electrolyte, the intrinsic resistance of the substrate and electroactive material, and contact resistance at the interface between electrolyte and electrode [47]. R_{ct} is the charge-transfer resistance, which is caused by the faradaic reaction and double-layer capacitance on the grain surface [48]. To account for the porous nature of the electrodes, the constant phase element (CPE) is used in the equivalent circuit. The impedance of CPE is defined as $Q = \frac{1}{T(jw)^n}$ with $-1 \leq n \leq 1$, where T, w and n are the frequency-independent constant, angular frequency and a correction factor. If $n = -1$, the CPE is an inductor and if $n = 0$, CPE is a pure resistor and if $n = 1$, CPE is a pure capacitor. Q_{dl} and Q_F represent the constant phase elements, which are mainly attributed to the double-layer capacitance and pseudocapacitance, respectively [49]. W is the Warburg resistance, which is caused by H^+ ion diffusion/transport within the porous structure of the electrodes [50].

Table 5.1. R_e, R_{ct}, W, and n parameters of electrodes obtained from the Nyquist plot fitting.

Electrode	R_e (Ω)	R_{ct} (Ω)	W (Ω/s$^{1/2}$)	n_{dl}	n_F
WO_3	0.224	4.08	3.25	0.93	0.98
WO_3-PANI	0.256	7.83	1.14	0.92	0.98

A summary of the WO_3 and WO_3-PANI best fitting values of the equivalent circuit parameters is presented in Table 5.1. In the high-frequency range, the intercept on the real axis and diameter of semicircle represent the equivalent series resistance (R_e) and interfacial charge-transfer resistance (R_{ct}). The straight slope in the low-frequency range, which is caused by the Warburg impedance (W), is related to the diffusion resistance of the H^+ ions in the electrode pores. Furthermore, the slope of the straight line is obvious larger than 45° in the very low-frequency range (≤ 100 mHZ), which deviates from the idealized porous electrode model. This deviation behavior of WO_3-PANI hybrid exhibits more pronounced than the WO_3. Such behavior is associated with the frequency dispersion caused by the deficiency in the porous electrode structure, which has also reported by Cooper [51]. As shown in the inset of Figure 5.11a, the R_e values of WO_3-PANI (0.25 Ω) was slightly larger than that of WO_3 (0.23 Ω), revealing that PANI imposes little resistance to the hybrid electrode. The R_{ct} values of WO_3-PANI (4.1 Ω) was lower than WO_3 (7.8 Ω), proving the lower activation energy for H^+ diffusion that resulted from PANI deposition. The slope of the straight line for WO_3-PANI is more than WO_3, indicating that the hybrid electrode had a lower diffusion resistance, corresponding to an increased capacity, compared to WO_3. Related to the porous surface of electrodes, a constant phase element was used in the equivalent circuit. The value of n obtained from the Nyquist plot fitting was between 0.9 and 1, indicating the ideal capacitive behavior of the hybrid electrode.

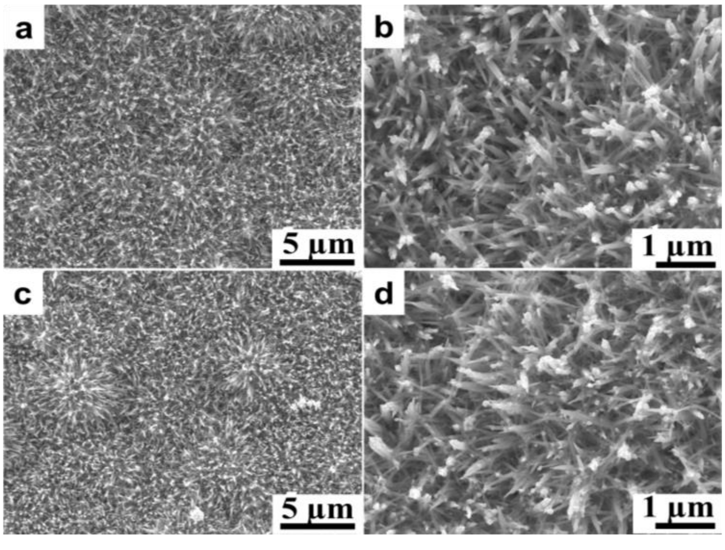

Figure 5.12. FESEM images of (a, b) WO_3 and (c, d) WO_3-PANI obtained after 1500 cycles.

To further evaluate the cycling performance of the hybrid electrode, GCD measurements were carried out on PANI, WO$_3$, and WO$_3$-PANI at a current density of 3 A/g, as shown in Figure 5.11 b. The initial gravimetric specific capacitances for WO$_3$ and WO$_3$-PANI were 166 and 259 F/g, respectively. However, the WO$_3$ and WO$_3$-PANI still presented 153 and 238 F/g after 1500 cycles, corresponding to capacitance retentions of 92.2% and 91.9%, respectively. Pure PANI suffered from a much faster capacitance fade (343 F/g at 3 A/g, 13.4% retention after 500 cycles), which evidenced its very poor cycle life. The fast degradation of gravimetric specific capacitance is caused by volumetric swelling, shrinkage, and structure cracking of PANI during the charge-discharge process, which was caused by insertion/extraction of dopants into and out of the PANI backbone. Such high gravimetric specific capacitance and excellent cycling stability of the WO$_3$-PANI electrodes are attributed to the pseudocapacitive behavior and electrical conductivity of PANI as well as the synergistic effect between the WO$_3$ and PANI layer. In order to gain a deeper understanding of the long-term stability, the morphologies of the WO$_3$ and WO$_3$-PANI electrodes after long-term cycles were examined by FESEM. As shown in Figure 5.12, after 1500 cycles, the WO$_3$ and WO$_3$-PANI nanowires were also homogeneously anchored on the substrate surface and their nanostructure morphologies were well preserved, indicating that the inner WO$_3$ layer was able to greatly enhance the mechanical stability of the WO$_3$-PANI hybrid electrode. All of the above results indicate that the inner WO$_3$ layer effectively accommodated the large volumetric expansion of the outer PANI layer during the redox process, even in long-term and repeating GCD processes.

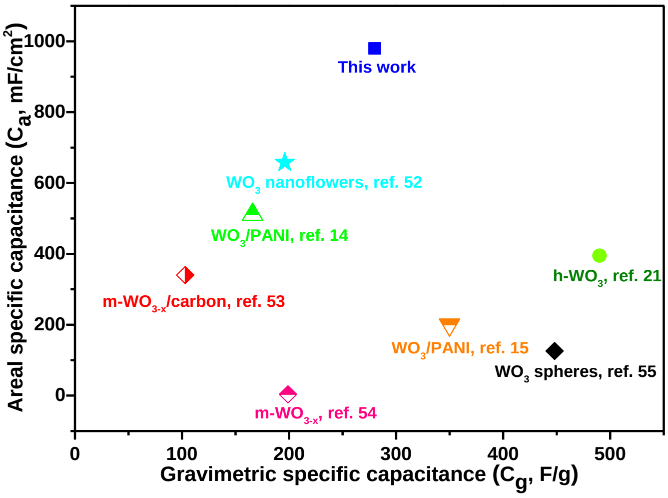

Figure 5.13. Balance relationship between C_a and C_g for different WO$_3$-based materials [14-15, 21, 52-55].

The areal specific capacitance (C_a, F/cm^2), also reported by Gogotsi [56], may be a more reliable performance metric compared to the gravimetric specific capacitance (C_g, F/g) for thin-film electrochemical capacitors. Here, we use the C_g and C_a to obtain a comprehensive assessment of the nanofilm electrodes. Figure 5.13 presents a comparison among several WO$_3$-

based materials emphasizing the relationship between C_a and C_g. An ultrahigh C_a of 980 mF/cm^2 and a large C_g of 278 F/g at a current density of 1 A/g were observed for the WO_3-PANI hybrid, which indicates the excellent combined properties compared with other pure WO_3 and WO_3-PANI materials. Most of the previously reported work of WO_3 and WO_3/conductive polymers as pseudocapacitor materials used C_a or C_g as the standard for performance evaluation, as shown in Table 5.2. The outstanding C_a of the hybrid electrode also exhibits the significant advantages of hydrothermal-electrodeposition to achieve high mass loadings of active material, which are the highest values among the pure WO_3 and WO_3/conductive polymer materials reported, to the best of our knowledge.

Table 5.2. Comparison of various WO_3 and WO_3/conductive polymer electrodes in recent years as pesudocapacitors

Material	**Preparation method**	**Potential window versus SHE (V)**	**Scan Rate (mV/s)**	**Capacitance**	**Current density**	**Capacitance**	**Ref.**
h-WO_3-PANI	Hydrothermal electrodeposition	-0.14-0.94	5-40	340-246 F/g	0.5-10 A/g	285-220 F/g 997-770 mF/cm^2	
NFL-WO_3	Electrodeposition	-0.3-0.2	10-100	196-138 F/g 652-458 mF/cm^2	6-14 mA/cm^2	206-148 F/g 684-490 mF/cm^2	52
h-WO_3	Hydrothermal reaction	-0.4-0.4	5-100	495-396 F/g 396-317 F/cm^2	n. a.	n. a.	21
WO_{3-x} /Carbon	evaporation-induced self-assembly	0.0-1.0	1-20	81 F/g 0.193 mF/cm^2	n. a.	n. a.	53
m-WO_{3-x}	Template-assisted synthesis	0.14-1.04	n. a.	n. a.	1-20 mA/cm^2	199-142 F/g 0.36-0.26 mF/cm^2	54
WO_3	Hydrothermal reaction	0.2-0.8	5-100	539-251 F/g 151-42.4 mF/cm^2	0.5-10 A/g	485-260 F/g 136.3-73 mF/cm^2	55
WO_3-PEDOT	Electrodeposition	0.0-1.0	n. a.	n. a.	0.1-10 mA/cm^2	205-80 mF/cm^2	57
CF-WO_3-PPY	Electropolymerization	-0.8-0.2	n. a.	n. a.	0.67-6.67 mA/cm^2	253-152 mF/cm^2	58
WO_3-PANI	Chemical bath deposition method	0.0-1.0	50	10 mF/cm^2	0.02 mA/cm^2	4.1 mF/cm^2	59

$W_{18}O_{49}$-PANI	Solvothermal-electrodeposition	-0.3-1.0	n. a.	n. a.	0.25-0.2 mA/cm^2	10-9 mF/cm^2	60
WO_3-PANI	Electrodeposition	-0.3-1.0	n. a.	n. a.	0.4 mA/cm^2	350 F/g 200 mF/cm^2	15
WO_3-PANI	Electrodeposition	-0.26-0.94	n. a.	n. a.	0.5-5 A/g	168-120 F/g 517-341 mF/cm^2	14
WO_3-PANI	Electropolymerization	-0.3-1.0	5-100	25-9 mF/cm^2	0.008-0.16 mA/cm^2	12-4 mF/cm^2	16

5.3.4 Symmetric supercapacitor performance

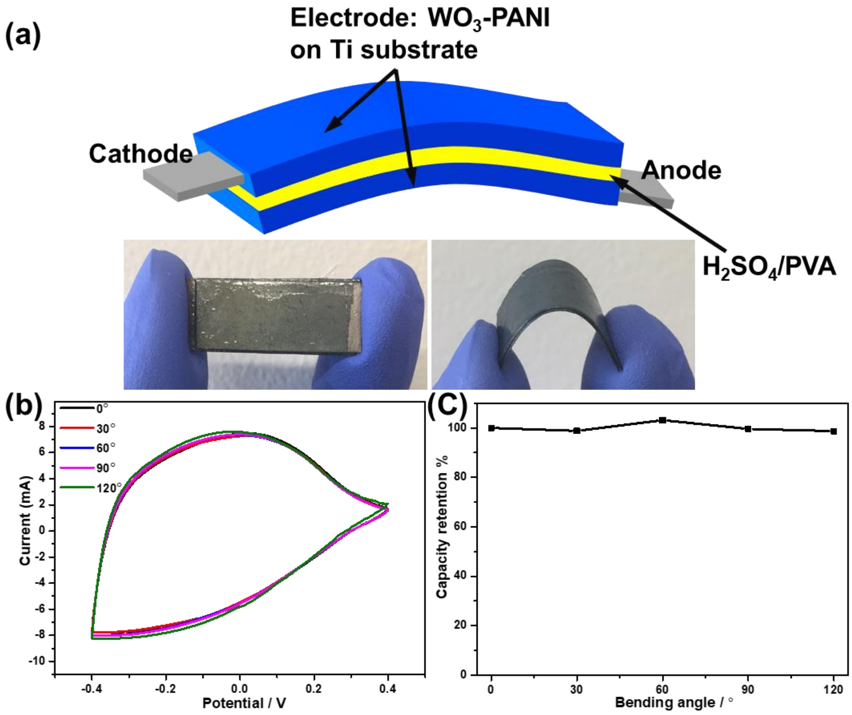

Figure 5.14. (a) Schematic diagram of the fabricated SSC device; photographs of the device in normal and bent states. (b) CV curves of the fabricated SSC at different bending angles with a scan rate of 40 mV/s. (c) Capacity retention of SSC at different bending angles.

A solid-state symmetric supercapacitor (SSC) was assembled using two freestanding WO_3-PANI hybrid electrodes as the positive and negative electrodes, in which H_2SO_4/PVA gel served as the electrolyte and separator. Figure 5.14a shows a schematic diagram of the solid-state SSC, and the inset photographs show the flexible device in normal and bent states. Figure 14b shows the CV curves of the SSC at different bending angles, and the shapes of the CV curves remained nearly the same for different bending angles from 0° to 120°. The capacity decay is almost no observed, as illustrated in Figure 5.14c, indicating the superior mechanical flexibility of the fabricated SSC device.

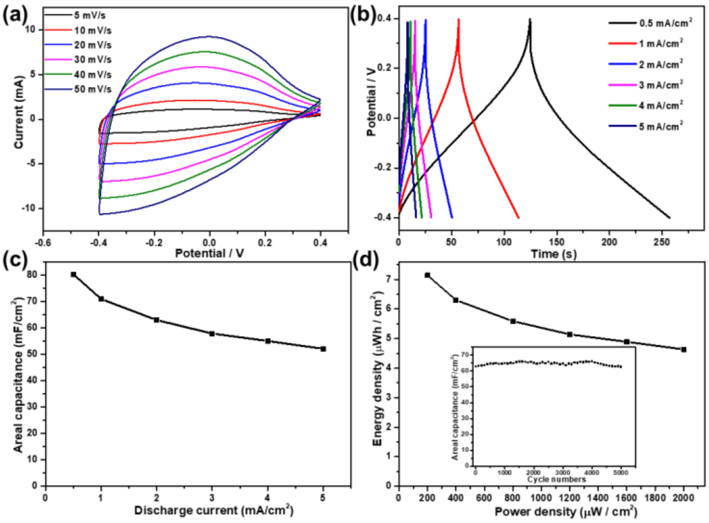

Figure 5.15. (a) CV curves of the fabricated SSC at different scan rates. (b) GCD curves of the fabricated SSC at different current densities. (c) Areal capacitance versus current density for the fabricated SSC. (d) Ragone plot for the fabricated SSC (inset shows the areal capacitance up to 5000 cycles at a current density of 2 mA/cm^2).

Figure 5.15a displays the CV curves of the fabricated SSC, which exhibited a nearly rectangular shape measured at various scan rates without obvious cathode or anode peaks. The absence of redox peaks attributed to the SSC is charged and discharged at a pseudo-constant rate over the entire voltammetric cycles [34,61]. The CV curves retained well-defined shapes, even at higher scan rates, indicating good electrochemical reversibility of the SSC device. Figure 5.15b shows the GCD curves of the fabricated SSC at various current densities. As shown in Figure 5.15c, the areal capacitances of the device were calculated to be 80.3, 70.9, 62.9, 57.8, 55, 52 mF/cm^2 at discharge current densities of 0.5, 1, 2, 3, 4 and 5 mA/cm^2, respectively. At a high current density of 5 mA/cm^2, the areal capacitance retained 65% for the device, which revealed its good rate capability. The energy density and power density have also been used to evaluate the fabricated SSC, as shown in Figure 5.15d. The maximum energy density of 7.14 μWh/cm^2 was achieved at a power density of 200 μW/cm^2, while the highest power density was 2000 μW/cm^2 at an energy density of 4.62 μWh/cm^2. The inset in Figure 5.15d shows the cycling performance of the fabricated SSC. The device exhibited very stable cycling performance with only 0.6% capacitance loss of its initial capacitance after 5 000 cycles. As shown in Figure 5.16, there is no visible difference in GCD curves after the long-term process. These results indicate that our WO_3-PANI//WO_3-PANI SSC device is a promising candidate for applications in flexible energy storage systems.

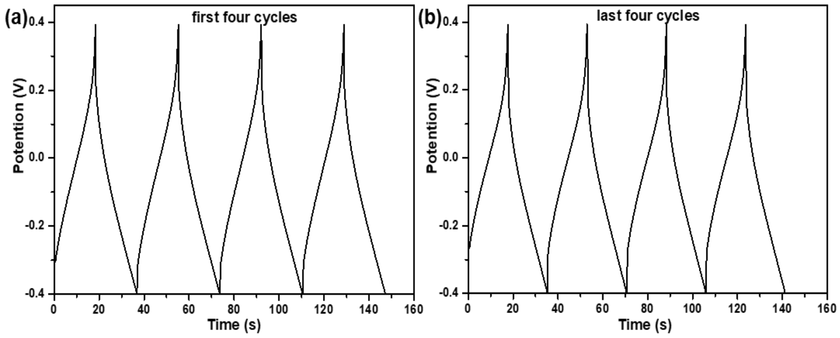

Figure 5.16. GCD curves of the first four and last four cycles.

5.3.5 The study of the band structure and synergistic mechanism

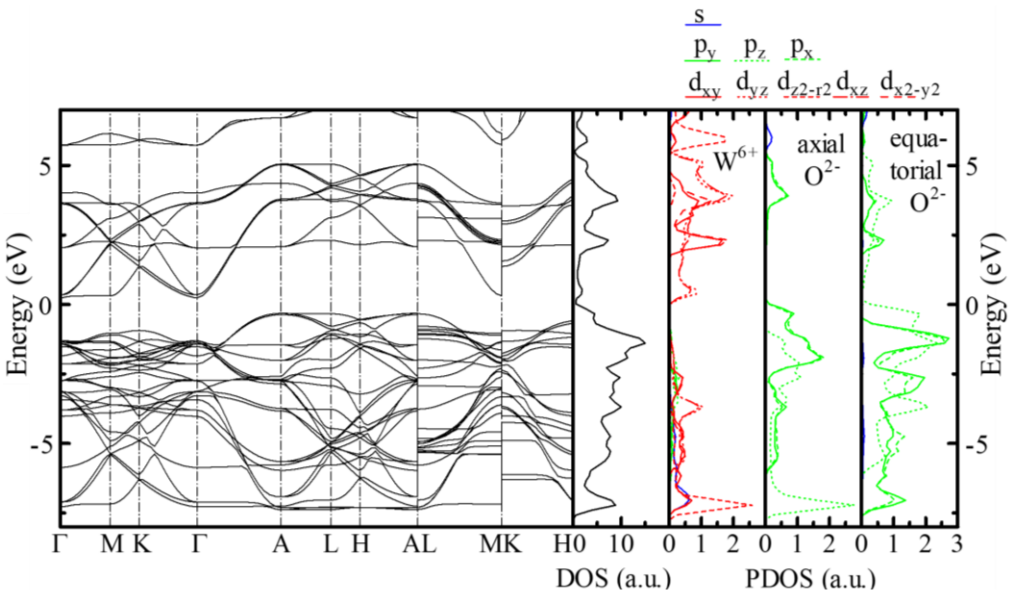

Figure 5.17. Band structure, DOS, and partial DOS curves of hexagonal WO_3.

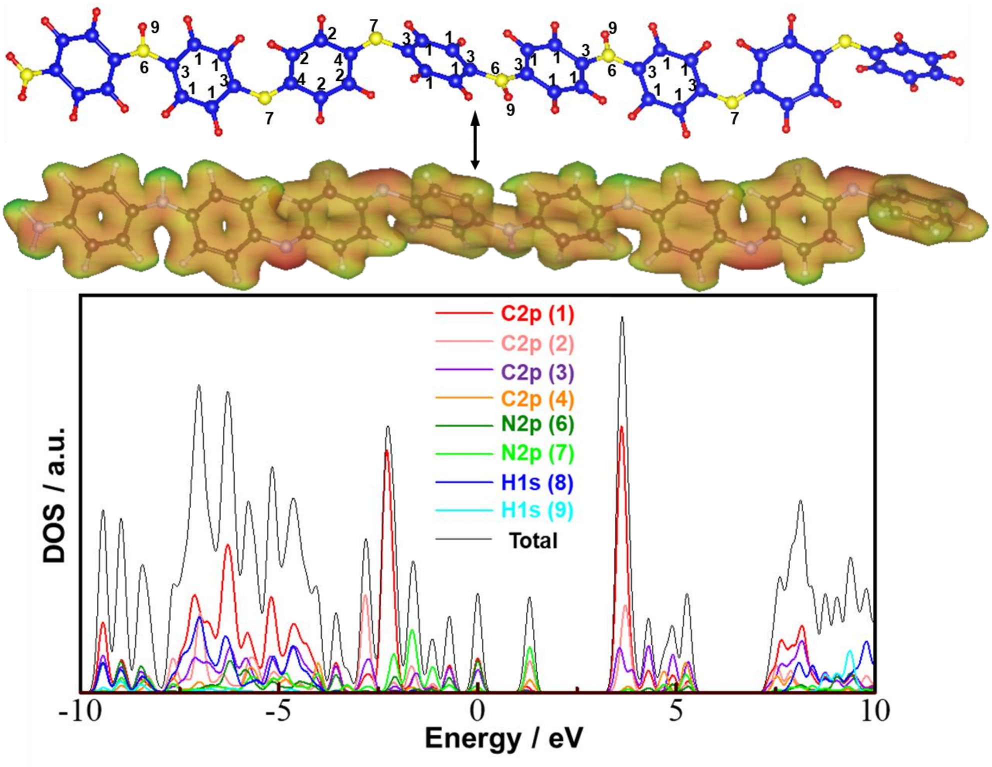

Figure 5.18. Charge density model and DOS of PANI molecules.

However, a fundamental understanding of the synergistic effect of each component about ionic transport regarding the PANI layer on WO_3 and the space between WO_3 nanowires is still missing. In most works [14-16,57-60], the enhanced capacitance performance of WO_3/conductive polymer composite was simply ascribed to the high conductivity of the conductive polymer and the synergistic effect of the WO_3 and conductive polymer. Little is known, however, about the further investigation of the synergistic effects of the WO_3/conductive polymer hybrid. Here, we propose a novel viewpoint from the perspective of the band structure. The band structure confirms that the WO_3 is an indirect semiconductor and the valence band maximum (VBM) seems to be at the A and L points in the reciprocal lattice (Figure 5.17). From the density of states (DOS) curves, the VBM is mainly composed of P_x and P_y orbital in equatorial oxygen atoms. The d_{xz} and d_{yz} orbitals in W form the conduction band minimum (CBM). These orbitals may not be delocalized, and the electrode reaction may be dominated by electron conduction. The d orbitals in the ab plane, d_{xy}, and $d_{x^2-y^2}$ emerge at higher energy. These band structures and electron states imply that electrons may be conducted along the (001) and (101) directions during the potential sweep in the CV measurement. This result shows that PANI may grow on both c and ab surfaces, as shown in Figure 5.2f. From these considerations, PANI possibly provides two important factors for the electrochemical activity. In addition to the high specific capacitance of PANI, conductivity is also an essential factor for the enhanced electrochemical activity. Usually, WO_3 is a semiconductor, and the conductivity is lower than that of PANI. In the case of pure PANI, the electron should be conducted within the PANI polymer chains. During the redox reaction, the conformation of PANI should be changed between benzene and quinone rings. Such a conformation change may suffer some deterioration by the interweaving of stacked polymer chains. For the hybrid film, as WO_3 nanowires provide a large specific surface area, they can make PANI chains much more stretchable (see the charge density model of PANI molecules in Figure 5.18), and the chain spacing increases, thereby reducing the interaction between PANI chains. This can promote inter-molecular and inner-molecular delocalization in PANI and enhance the conductivity, which can also facilitate the charge transport in the multiple voids of the structural WO_3 nanowires. Further, as shown in equation (2), the redox process in the WO_3 interior is accompanied by a concomitant intercalation/deintercalation of H^+ into/out of the film. While the H^+ ions released from the WO_3 interior can enter the PANI layer, the H^+ concentration in the PANI layer will increase gradually, which in turn results in an enhancement of PANI electroactivity. These factors provide a significant advantage for the electrochemical activity without deterioration.

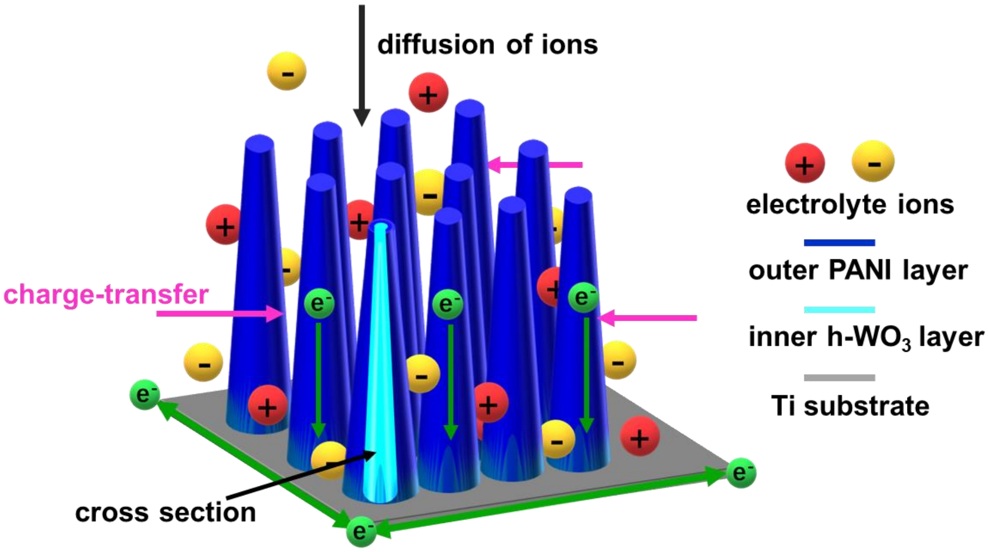

Figure 5.19. Schematic illustration of electrolyte diffusion paths in WO_3-PANI hybrid nanostructures.

Based on the above results, the high specific capacitance and excellent cycling stability of the WO_3-PANI hybrid electrode should be related to its ingenious nanostructure design and the synergistic effect between the inner WO_3 and outer PANI layers. The presented design possesses several distinct advantages for fabricated high-performance SC electrodes: (1) The WO_3 nanowires directly grow on the Ti substrate without any additive, serving as the current collector, which reveal a low contact resistance and superior mechanical stability. The pores between WO_3 nanowires facilitate the fast transport of electrolyte ions and ensure higher utilization of the active materials. (2) Conductive PANI is not only coated on the surface of the WO_3 nanowires but also covers the void spaces and acts as an interconnected bridge between the WO_3 nanowires to facilitate electron transport. As shown in Figure 5.19, the inner/outer coating structural WO_3-PANI hybrid result to facilitate both the ionic transport of H^+ and the electrochemical availability efficiency of PANI. (3) The inter-nanowire spacings of WO_3 are large enough to buffer the large volumetric swelling/shrinkage of PANI during the long-term GCD cycling, which is essential to realize an improved cycle life. The hybrid design that couples WO_3 with PANI can effectively offset the disadvantages of PANI. (4) PANI can significantly enhance the capacitance of the hybrid electrodes, which can be attributed to two aspects: high specific capacitance and superb electronic properties. For the increased capacitance, the contribution of PANI is not only attributed to its high specific capacitance but also related to the extension of the potential window. Also, the superb electronic property of the outer PANI layer leads to the lower charge transfer resistance of the WO_3-PANI electrode in the electrolyte. This can promote the electrolyte ion diffusion, leading to fast doping/de-doping and high utilization of the active materials, which also can increase the specific capacitance. Thus, the WO_3-PANI hybrid electrode presents excellent electrochemical performance.

5.4 Conclusion

In this work, the inner/outer coating structural hexagonal WO_3-PANI was successfully synthesized through the hydrothermal-electrodeposition route. The hexagonal WO_3 nanowires are well grown on Ti surface and the inner WO_3 is decorated by outer PANI layer, resulting in WO_3-PANI hybrid nanostructures. Through studying the growth process of WO_3 on the Ti substrate, a formation mechanism of WO_3 was proposed. The hybrid architecture of the WO_3-PANI electrode exhibited significantly enhanced specific capacitance, good rate capability, and superior cycling performance. The resultant WO_3-PANI hybrid achieved outstanding electrochemical performance, owing to the elaborately designed nanostructure and the synergistic effects of WO_3 and PANI. The fabricated all-solid-state device also exhibited remarkable flexibility and good electrochemical performances. We also proposed a possible mechanism of the synergistic effect based on a new perspective. The hydrothermal synthesis and electrodeposition methods for fabricating WO_3-PANI as a binder-free electrode are straightforward and controllable. The novel design strategy presented here may also have a potential application for the direct design and fabrication of other metal oxides and conductive polymers hybrid electrodes, for obtaining high-performance electrochemical energy storage.

Reference

1. Lu, X.; Wang, G.; Zhai, T.; Yu, M.; Xie, S.; Ling, Y.; Liang, C.; Tong, Y.; Li, Y., Stabilized TiN nanowire arrays for high-performance and flexible supercapacitors. *Nano letters* **2012,** *12* (10), 5376-5381.
2. Peng, L.; Peng, X.; Liu, B.; Wu, C.; Xie, Y.; Yu, G., Ultrathin two-dimensional MnO_2/graphene hybrid nanostructures for high-performance, flexible planar supercapacitors. *Nano letters* **2013,** *13* (5), 2151-2157.
3. González, A.; Goikolea, E.; Barrena, J.A., Review on supercapacitors: technologies and materials. *Renewable and Sustainable Energy Reviews* **2016,** *58*, 1189-1206.
4. He, Y.B.; Li, G.R.; Wang, Z.L.; Su, C.Y.; Tong, Y.X., Single-crystal ZnO nanorod/amorphous and nanoporous metal oxide shell composites: Controllable electrochemical synthesis and enhanced supercapacitor performances. *Energy & Environmental Science* **2011,** *4* (4), 1288-1292.
5. Wang, G.; Zhang, L.; Zhang, J., A review of electrode materials for electrochemical supercapacitors. *Chemical Society Reviews* **2012,** *41* (2), 797-828.
6. Zhang, Y.; Feng, H.; Wu, X.; Wang, L.; Zhang, A.; Xia, T.; Dong, H.; Li, X.; Zhang, L., Progress of electrochemical capacitor electrode materials: A review. *International journal of hydrogen energy* **2009,** *34* (11), 4889-4899.
7. Bhadra, S.; Khastgir, D.; Singha, N.K.; Lee, J.H., Progress in preparation, processing and applications of polyaniline. *Progress in polymer science* **2009,** *34* (8), 783-810.
8. MacDiarmid, A.G., "Synthetic metals": A novel role for organic polymers (Nobel lecture). *Angewandte Chemie International Edition* **2001,** *40* (14), 2581-2590.
9. Meng, C.; Liu, C.; Chen, L.; Hu, C.; Fan, S., Highly flexible and all-solid-state paperlike polymer supercapacitors. *Nano letters* **2010,** *10* (10), 4025-4031.
10. Xia, C.; Chen, W.; Wang, X.; Hedhili, M.N.; Wei, N.; Alshareef, H.N., Highly stable supercapacitors with conducting polymer core-shell electrodes for energy storage applications. *Advanced Energy Materials* **2015,** *5* (8), 1401805.
11. Xiao, X.; Ding, T.; Yuan, L.; Shen, Y.; Zhong, Q.; Zhang, X.; Cao, Y.; Hu, B.; Zhai, T.; Gong, L., WO_{3-x}/MoO_{3-x} Core/Shell Nanowires on Carbon Fabric as an Anode for All-Solid-State Asymmetric Supercapacitors. *Advanced Energy Materials* **2012,** *2* (11), 1328-1332.
12. Zheng, H.; Ou, J.Z.; Strano, M.S.; Kaner, R.B.; Mitchell, A.; Kalantar-zadeh, K., Nanostructured tungsten oxide-properties, synthesis, and applications. *Advanced Functional Materials* **2011,** *21* (12), 2175-2196.

13. Zhou, Z.; Kong, B.; Yu, C.; Shi, X.; Wang, M.; Liu, W.; Sun, Y.; Zhang, Y.; Yang, H.; Yang, S., Tungsten oxide nanorods: an efficient nanoplatform for tumor CT imaging and photothermal therapy. *Scientific reports* **2014,** *4,* 3653.
14. Zou, B.X.; Liang, Y.; Liu, X.X.; Diamond, D.; Lau, K.T., Electrodeposition and pseudocapacitive properties of tungsten oxide/polyaniline composite. *Journal of Power Sources* **2011,** *196* (10), 4842-4848.
15. Samu, G.F.; Pencz, K.; Janáky, C.; Rajeshwar, K., On the electrochemical synthesis and charge storage properties of WO_3/polyaniline hybrid nanostructures. *Journal of Solid State Electrochemistry* **2015,** *19* (9), 2741-2751.
16. Wei, H.; Yan, X.; Wu, S.; Luo, Z.; Wei, S.; Guo, Z., Electropolymerized polyaniline stabilized tungsten oxide nanocomposite films: electrochromic behavior and electrochemical energy storage. *The Journal of Physical Chemistry C* **2012,** *116* (47), 25052-25064.
17. Janáky, C.; Rajeshwar, K., The role of (photo) electrochemistry in the rational design of hybrid conducting polymer/semiconductor assemblies: From fundamental concepts to practical applications. *Progress in Polymer Science* **2015,** *43*, 96-135.
18. Budevski, E.; Staikov, G.; Lorenz, W., Electrocrystallization: Nucleation and growth phenomena. *Electrochimica Acta* **2000,** *45* (15-16), 2559-2574.
19. Datta, M.; Landolt, D., Fundamental aspects and applications of electrochemical microfabrication. *Electrochimica acta* **2000,** *45* (15-16), 2535-2558.
20. Yan, Z.; Sun, H.; Chen, X.; Liu, H.; Zhao, Y.; Li, H.; Xie, W.; Cheng, F.; Chen, J., Anion insertion enhanced electrodeposition of robust metal hydroxide/oxide electrodes for oxygen evolution. *Nature communications* **2018,** *9* (1), 2373.
21. Chen, Z.; Peng, Y.; Liu, F.; Le, Z.; Zhu, J.; Shen, G.; Zhang, D.; Wen, M.; Xiao, S.; Liu, C.P., Hierarchical nanostructured WO_3 with biomimetic proton channels and mixed ionic-electronic conductivity for electrochemical energy storage. *Nano letters* **2015,** *15* (10), 6802-6808.
22. Kresse, G.; Furthmüller, J., Efficient iterative schemes for ab initio total-energy calculations using a plane-wave basis set. *Physical review B* **1996,** *54* (16), 11169.
23. Kresse, G.; Joubert, D., From ultrasoft pseudopotentials to the projector augmented-wave method. *Physical Review B* **1999,** *59* (3), 1758.
24. Adachi, H.; Tsukuda, M.; Satoko, C., Discrete variational Xα cluster calculations. I. Application to metal clusters. *Journal of the Physical Society of Japan* **1978,** *45* (3), 875-883.

25. Li, Q.; Wang, Z.L.; Li, G.R.; Guo, R.; Ding, L.X.; Tong, Y.X., Design and synthesis of MnO_2/Mn/MnO_2 sandwich-structured nanotube arrays with high supercapacitive performance for electrochemical energy storage. *Nano letters* **2012,** *12* (7), 3803-3807.
26. Zhang, J.; Jiang, J.; Li, H.; Zhao, X., A high-performance asymmetric supercapacitor fabricated with graphene-based electrodes. *Energy & Environmental Science* **2011,** *4* (10), 4009-4015.
27. Trchová, M.; Stejskal, J., Polyaniline: The infrared spectroscopy of conducting polymer nanotubes. *Pure and Applied Chemistry* **2011,** *83* (10), 1803-1817.
28. Salmaoui, S.; Sediri, F., Large-scale synthesis and electrochemical properties of hydrated tungsten trioxide-based hierarchical microstructures. *Journal of Alloys and Compounds* **2016,** *661*, 82-91.
29. Salmaoui, S.; Sediri, F.; Gharbi, N.; Perruchot, C.; Jouini, M., Hexagonal hydrated tungsten oxide nanomaterials: hydrothermal synthesis and electrochemical properties. *Electrochimica Acta* **2013,** *108*, 634-643.
30. Zhu, X.; Elomaa, M.; Sundholm, F.; Lochmüller, C.H., Infrared and thermogravimetric studies of thermal degradation of polystyrene in the presence of ammonium sulfate. *Polymer Degradation and Stability* **1998,** *62* (3), 487-494.
31. Phuruangrat, A.; Ham, D.J.; Hong, S.J.; Thongtem, S.; Lee, J.S., Synthesis of hexagonal WO_3 nanowires by microwave-assisted hydrothermal method and their electrocatalytic activities for hydrogen evolution reaction. *Journal of Materials Chemistry* **2010,** *20* (9), 1683-1690.
32. Rougier, A.; Portemer, F.; Quede, A.; El Marssi, M., Characterization of pulsed laser deposited WO_3 thin films for electrochromic devices. *Applied Surface Science* **1999,** *153* (1), 1-9.
33. Kovács, T.N.; Pokol, G.; Gáber, F.; Nagy, D.; Igricz, T.; Lukács, I.E.; Fogarassy, Z.; Balázsi, K.; Szilágyi, I.M., Preparation of iron tungstate ($FeWO_4$) nanosheets by hydrothermal method. *Materials Research Bulletin* **2017,** *95*, 563-569.
34. Gao, L.; Wang, X.; Xie, Z.; Song, W.; Wang, L.; Wu, X.; Qu, F.; Chen, D.; Shen, G., High-performance energy-storage devices based on WO_3 nanowire arrays/carbon cloth integrated electrodes. *Journal of Materials Chemistry A* **2013,** *1* (24), 7167-7173.
35. Wang, J.; Khoo, E.; Lee, P.S.; Ma, J., Controlled synthesis of WO_3 nanorods and their electrochromic properties in H_2SO_4 electrolyte. *The Journal of Physical Chemistry C* **2009,** *113* (22), 9655-9658.
36. Khalid, M.; Acuna, J.J.; Tumelero, M.A.; Fischer, J.A.; Zoldan, V.C.; Pasa, A.A., Sulfonated porphyrin doped polyaniline nanotubes and nanofibers: synthesis and characterization. *Journal of Materials Chemistry* **2012,** *22* (22), 11340-11346.

37. Zilberman, M.; Titelman, G.; Siegmann, A.; Haba, Y.; Narkis, M.; Alperstein, D., Conductive blends of thermally dodecylbenzene sulfonic acid-doped polyaniline with thermoplastic polymers. *Journal of applied polymer science* **1997,** *66* (2), 243-253.
38. Bhosale, N.Y.; Mali, S.S.; Hong, C.K.; Kadam, A.V., Hydrothermal synthesis of WO_3 nanoflowers on etched ITO and their electrochromic properties. *Electrochimica Acta* **2017,** *246*, 1112-1120.
39. Zhang, T.; Zhu, Z.; Chen, H.; Bai, Y.; Xiao, S.; Zheng, X.; Xue, Q.; Yang, S., Iron-doping-enhanced photoelectrochemical water splitting performance of nanostructured WO_3: a combined experimental and theoretical study. *Nanoscale* **2015,** *7* (7), 2933-2940.
40. Chen, J.P.; Yang, R.T., Selective Catalytic Reduction of NO with NH_3 on $SO^{-2}{}_4/TiO_2$ Superacid Catalyst. *Journal of Catalysis* **1993,** *139* (1), 277-288.
41. Kowalski, G.; Pielichowski, J.; Grzesik, M., Characteristics of polyaniline cobalt supported catalysts for epoxidation reactions. *The Scientific World Journal* **2014,** *2014*.
42. Zeng, X.R.; Ko, T.M., Structures and properties of chemically reduced polyanilines. *Polymer* **1998,** *39* (5), 1187-1195.
43. Petrovski, A.; Paunović, P.; Avolio, R.; Errico, M. E.; Cocca, M.; Gentile, G.; Grozdanov, A.; Avella, M.; Barton, J.; Dimitrov, A., Synthesis and characterization of nanocomposites based on PANI and carbon nanostructures prepared by electropolymerization. *Materials Chemistry and Physics* **2017,** *185*, 83-90.
44. Van Hoang, H.; Holze, R., Electrochemical synthesis of polyaniline/montmorillonite nanocomposites and their characterization. *Chemistry of materials* **2006,** *18* (7), 1976-1980.
45. Kulesza, P.J.; Faulkner, L.R., Electrocatalysis at a novel electrode coating of nonstoichiometric tungsten (VI, V) oxide aggregates. *Journal of the American Chemical Society* **1988,** *110* (15), 4905-4913.
46. Augustyn, V.; Simon, P.; Dunn, B., Pseudocapacitive oxide materials for high-rate electrochemical energy storage. *Energy & Environmental Science* **2014,** *7* (5), 1597-1614.
47. Liu, C.; Yu, Z.; Neff, D.; Zhamu, A.; Jang, B.Z., Graphene-based supercapacitor with an ultrahigh energy density. *Nano letters* **2010,** *10* (12), 4863-4868.
48. Xu, J.; Ding, T.; Wang, J.; Zhang, J.; Wang, S.; Chen, C.; Fang, Y.; Wu, Z.; Huo, K.; Dai, J., Tungsten oxide nanofibers self-assembled mesoscopic microspheres as high-performance electrodes for supercapacitor. *Electrochimica Acta* **2015,** *174*, 728-734.
49. Zhou, Y.K.; He, B.L.; Zhou, W.J.; Li, H.L., Preparation and electrochemistry of SWNT/PANI composite films for electrochemical capacitors. *Journal of the Electrochemical Society* **2004,** *151* (7), A1052-A1057.

50. Yang, X.; Zhu, J.; Qiu, L.; Li, D., Bioinspired effective prevention of restacking in multilayered graphene films: towards the next generation of high-performance supercapacitors. *Advanced Materials* **2011,** *23* (25), 2833-2838.
51. Cooper, S.J.; Bertei, A.; Finegan, D.P.; Brandon, N.P., Simulated impedance of diffusion in porous media. *Electrochimica Acta* **2017,** *251*, 681-689.
52. Qiu, M.; Sun, P.; Shen, L.; Wang, K.; Song, S.; Yu, X.; Tan, S.; Zhao, C.; Mai, W., WO_3 nanoflowers with excellent pseudo-capacitive performance and the capacitance contribution analysis. *Journal of Materials Chemistry A* **2016,** *4* (19), 7266-7273.
53. Jo, C.; Hwang, J.; Song, H.; Dao, A.H.; Kim, Y.T.; Lee, S.H.; Hong, S.W.; Yoon, S.; Lee, J., Block-Copolymer-Assisted One-Pot Synthesis of Ordered Mesoporous WO_{3-x}/Carbon Nanocomposites as High-Rate-Performance Electrodes for Pseudocapacitors. *Advanced Functional Materials* **2013,** *23* (30), 3747-3754.
54. Yoon, S.; Kang, E.; Kim, J.K.; Lee, C.W.; Lee, J., Development of high-performance supercapacitor electrodes using novel ordered mesoporous tungsten oxide materials with high electrical conductivity. *Chemical Communications* **2011,** *47* (3), 1021-1023.
55. Zheng, F.; Gong, H.; Li, Z.; Yang, W.; Xu, J.; Hu, P.; Li, Y.; Gong, Y.; Zhen, Q., Tertiary structure of cactus-like WO_3 spheres self-assembled on Cu foil for supercapacitive electrode materials. *Journal of Alloys and Compounds* **2017,** *712*, 345-354.
56. Gogotsi, Y.; Simon, P., True performance metrics in electrochemical energy storage. *Science* **2011,** *334* (6058), 917-918.
57. Szymanska, D.; Rutkowska, I.A.; Adamczyk, L.; Zoladek, S.; Kulesza, P.J., Effective charge propagation and storage in hybrid films of tungsten oxide and poly(3,4-ethylenedioxythiophene). *Journal of Solid State Electrochemistry* **2010,** *14* (11), 2049-2056.
58. Wang, F.; Zhan, X.; Cheng, Z.; Wang, Z.; Wang, Q.; Xu, K.; Safdar, M.; He, J., Tungsten oxide@ polypyrrole core-shell nanowire arrays as novel negative electrodes for asymmetric supercapacitors. *Small* **2015,** *11* (6), 749-755.
59. Nwanya, A.C.; Jafta, C.J.; Ejikeme, P.M.; Ugwuoke, P.E.; Reddy, M.; Osuji, R.U.; Ozoemena, K.I.; Ezema, F.I., Electrochromic and electrochemical capacitive properties of tungsten oxide and its polyaniline nanocomposite films obtained by chemical bath deposition method. *Electrochimica Acta* **2014,** *128*, 218-225.
60. Tian, Y.; Cong, S.; Su, W.; Chen, H.; Li, Q.; Geng, F.; Zhao, Z., Synergy of $W_{18}O_{49}$ and polyaniline for smart supercapacitor electrode integrated with energy level indicating functionality. *Nano letters* **2014,** *14* (4), 2150-2156.
61. Lang, X.; Hirata, A.; Fujita, T.; Chen, M., Nanoporous metal/oxide hybrid electrodes for electrochemical supercapacitors. *Nature nanotechnology* **2011,** *6* (4), 232.

Chapter 6 Summary and Prospects

6.1 Summary

Progress towards the development of advanced supercapacitor technologies is closely associated with the continuous evolution of electrode materials. Early studies in electrode materials have focused on carbon-based electrodes of electric double-layer capacitors due to their low cost, large surface area, and good electric conductivity. However, these carbon-based materials usually suffer from low specific capacitance and energy density. Hence, researchers have shifted their attention from pure carbon materials to pseudocapacitor electrode materials (such as transition metal oxides/hydroxides and conductive polymers). To achieve high electrochemical performance, large electrolyte-accessible surface areas and high conductivity are, among others, two major prerequisites for the electrode materials used in the supercapacitors. To develop new electrode materials with high electrochemical performance, two important research directions in supercapacitor electrode exploration are nanostructured porous materials and composite materials. Usually, the nanostructured porous materials can facilitate ionic motion, improve the rate capability, and increase the utilization of active materials. Unfortunately, transition metal oxides/hydroxides are mostly low electric conductivity, and as a result, it is challenging to build effective supercapacitors based on pure metal oxides/hydroxides electrodes. To solve this problem, we designed a new strategy for achieving high performance supercapacitors and overcoming the low electric conductivity problems of transition metal oxides/hydroxides by hybridization metal oxides/hydroxides with conductive polymers, and a synergistic effect is achieved in this approach.

In this thesis, the nanostructured porous materials and composite materials based on metal oxides/hydroxides with conducting polymers have been elaborately designed and synthesized to realize enhanced electrochemical performance.

The transition metal hydroxide, including layered double hydroxides (LDHs), are ideal electrode materials for pseudocapacitors owing to their high redox activity, structural controllability and environmentally friendly nature. In the first phase, a series of layered double hydroxides (LDHs) CoAl LDH, NiAl LDH, and NiFe LDH nanosheet films with porous structures were successfully synthesized by hydrothermal methods. The LDHs nanosheet films were grown perpendicularly on the substrate and examined them as binder-free electrodes for pseudocapacitors. SEM micrographs showed that the thicknesses of LDHs layered nanosheets were ~100, ~ 40 and ~85 nm for CoAl, NiAl and NiFe LDHs samples. Although the samples have hydrotalcite structure, due to their different morphology and composition, the electrochemical properties of the LDHs have significant differences. The CoAl LDH exhibited the highest capacitance and good cycling stability among the three types of LDHs. The good cycling stability was possibly related with the stable plate-like nanosheets structure, which made it promising candidates for practical application as supercapacitor electrode materials.

Nevertheless, the relatively poor cycling life and low electric conductivity of the LDHs limited their supercapacitor applications. In the second phase, after studying the CoAl LDH in the first phase, we successfully used in hydrothermal-electrodeposition method to prepare a novel inner/outer layer structural CoAl LDH-PANI nanocomposite in which the CoAl LDH nanofilms were well grown on Ni surface and the inner CoAl LDH was decorated by outer PANI layer. The hydrothermal-electrodeposition method for synthesis of LDH-PANI growth on Ni substrate was straightforward and controllable. The hybrid architecture CoAl LDH-PANI exhibited greatly enhanced specific capacitance and cycling stability (528 F/g at a current density of 10 A/g, 142.7% retention after 6000 cycles) and was superior to the non-decorated CoAl LDH (425 F/g at a current density of 10 A/g, 83.3% retention after 6000 cycles). We revealed the degradation behavior of PANI in 1 M KOH/KCl electrolyte, and the active degradation products also further increased the total specific capacitance of the composite. The enhanced electrochemical performance of the nanocomposite could be attributed to its well-designed nanostructure and the synergistic effects of each component. By analyzing the band structure and density of states of CoAl LDH and PANI, we proposed the possible mechanism of synergistic effect in a new perspective. We deemed that our research would be valuable in improving knowledge about LDHs/conducting polymer hybrid.

The application of a magnetic field for advanced materials have attracted considerable attention owing to their potential application in improving the optical, mechanical, chemical, electronic properties, and so on. The controlled development of the crystal orientation in nanomaterial was very useful for improving its properties. In the third phase, the preparation of oriented CoAl LDH nanosheets was achieved by hydrothermal grow and slip casting with the assistance of an external magnetic field. The induction effect of applied high magnetic field on the morphology and composition of CoAl LDH was first investigated. It was found that the application of a high magnetic field has no effect on the crystal phase, but the obvious effects of the oriented growth and arrangement of the CoAl LDH microcrystals along the easy magnetic axis. The supplemental high magnetic field presented here was expected that it has a potential application to get the desired morphologies of nanostructures with excellent performance.

The transition metal oxides, such as tungsten oxide (WO_3), have received increasing attention as a promising supercapacitor electrode material owing to its large specific surface area, electrochemical stability and eco-friendly nature. Nevertheless, the insufficient capacitance of WO_3 still remained a major obstacle for supercapacitor applications. In the final phase, the inner/outer coating structural hexagonal WO_3-PANI was successfully synthesized through the hydrothermal-electrodeposition route. The hexagonal WO_3 nanowires were well grown on Ti surface and the inner WO_3 was decorated by outer PANI layer, resulting in WO_3-PANI hybrid nanostructures. Through studying the growth process of WO_3 on the Ti substrate surface, a formation mechanism of WO_3 was proposed. The hydrothermal-electrodeposition method for synthesis of LDH-PANI growth on Ni substrate was straightforward and controllable. The resulting WO_3-PANI hybrid electrode exhibited a significantly enhanced gravimetric specific capacitance (278 F/g at a current density of 1 A/g) with an outstanding areal specific capacitance of 979 mF/cm^2, good rate performance (77.2% capacitance retention from 0.5 to 10 A/g), and stable cycling performance (91.9% capacitance retention over 1500 cycles). The outstanding electrochemical properties of the WO_3-PANI electrode were ascribed to its ingenious nanostructure design and the synergistic effects of each component. A flexible all-solid-state symmetric supercapacitor was assembled with the WO_3-PANI electrodes using PVA/H_2SO_4 electrolyte. The device displayed a high areal capacitance of 62.9 mF/cm^2 (99.4% capacitance retention over 5000 cycles) and remarkable flexibility, suggesting potential application in flexible energy storage devices. Based on analysis and study the band structure of WO_3 and the electrochemical properties of the PANI-coated WO_3 hybrid electrode, a possible mechanism for the synergistic effect was proposed in a new perspective. The novel design strategy presented in this thesis may also have a potential application for the direct design and fabrication of other metal oxides/hydroxides and conductive polymers hybrid electrodes, for obtaining high-performance electrochemical energy storage.

6.2 Prospects

Supercapacitor are playing an important role in energy storage and conversion systems. However, it is still a great challenge to develop supercapacitors with an energy density close to that of current rechargeable batteries, as well as a high power density and long cycle life.

To achieve the goals, the future research of supercapacitors mainly includes the following aspects. (1) Developing new electrolytes with more wide voltage window and working temperatures; (2) Discovering new electrode materials (involve developing nanostructured materials and composite materials); (3) Developing new type asymmetric/hybrid supercapacitors.

We are expected that much more research will be carried out towards the development of novel electrode materials and new cell configurations due to the rapidly growing demands on supercapacitors.

List of Publications

1. **Yang, G.**; Takei, T.; Yanagida, S.; Kumada, N., Synthesis and Electrochemical Properties of CoAl, NiAl, CoFe and NiFe Layered Double Hydroxide Films. *J. Ion Exch*. **2018**, 29 (3), 131-135.

2. **Yang, G.**; Takei, T.; Yanagida, S.; Kumada, N., Enhanced Supercapacitor Performance Based on CoAl Layered Double Hydroxide-Polyaniline Hybrid Electrodes Manufactured Using Hydrothermal-Electrodeposition Technology. *Molecules* **2019**, 24 (5), 976.

3. **Yang, G.**; Takei, T.; Yanagida, S.; Kumada, N., Hexagonal Tungsten Oxide-Polyaniline Hybrid Electrodes for High-Performance Energy Storage. *Appl. Surf. Sci.* (Accepted, 2019,09)

List of Awards

1. 7th Japan Association for Chemical Innovation/Green and Sustainable Chemistry (JACI/GSC) Symposium Best Poster Presentation Award, Japan Association for Chemical Innovation, Japan (2018).

2. Encouragement Award, Faculty of Engineering, University of Yamanashi, Kofu, Japan (2019).

List of Presentations

International Conference

1. “Synthesis and Electrochemical Properties of Layered Double Hydroxide Film Composed of Period-Four Transition Metals and Its Hybrid with Conductive Polymer” ***Guoshen YANG***, *Takahiro TAKEI, Sayaka YANAGIDA, Nobuhiro KUMADA*. 15th Conference & Exhibition of the European Ceramic Society (ECerS 2017). Budapest, Hungary. (July 9-13, 2017)

2. “Synthesis of Metal Hydroxide-Conductive Polymer Hybrid Films and Application to Supercapacitor”
   Guoshen YANG, *Takahiro TAKEI, Sayaka YANAGIDA, Nobuhiro KUMADA*. 6th International Seminar on Green Energy Conversion, Nagano, Japan. (September 13-15, 2017)
3. “Synthesis and Electrochemical Properties of CoAl, NiAl, CoFe and NiFe Layered Double Hydroxide Films”
   Guoshen YANG, *Takahiro TAKEI, Sayaka YANAGIDA, Nobuhiro KUMADA*. 7th International Conference on Ion Exchange 2018, Yogyakarta, Indonesia. (September 10-13, 2018)

4. “Synthesis of Tungsten Oxide-Polyaniline Hybrid Film and Its High Performance Energy Storage”
   Guoshen YANG, *Takahiro TAKEI, Sayaka YANAGIDA, Nobuhiro KUMADA*. 7th International Seminar on Green Energy Conversion, Kofu, Japan. (August 22-23, 2018)

5. “Study on Synthesis of Metal Oxide/Hydroxide-Conductive Polymer Hybrid Film and Its Electrochemical Properties”
   Guoshen YANG, *Takahiro TAKEI, Sayaka YANAGIDA, Nobuhiro KUMADA*. 8th International Conference on Nanoscience and Technology, ChinaNANO 2019, Beijing, China. (August 17-19, 2019)

Domestic Conference

6. “Synthesis and Electrochemical Properties of Metal Hydroxide-Conductive Polymer Hybrid Films”
   Guoshen YANG, *Takahiro TAKEI, Sayaka YANAGIDA, Nobuhiro KUMADA*. The Ceramic Society of Japan Annual Meeting 2017, Tokyo, Japan. (March 17-19, 2017)

7. “Synthesis and Electrochemical Properties of Layered Double Hydroxide Film Composed of Period-Four Transition Metals and Its Hybrid with Conductive Polymer”
   Guoshen YANG, *Takahiro TAKEI, Sayaka YANAGIDA, Nobuhiro KUMADA*. 6th Japan Association for Chemical Innovation/Green and Sustainable Chemistry (JACI/GSC) Symposium, Tokyo, Japan. (July 3-4, 2017)

8. “Synthesis of Transition Metal Hydroxide-Conductive Polymer Hybrid and Its Electrochemical properties”

Guoshen YANG, *Takahiro TAKEI, Sayaka YANAGIDA, Nobuhiro KUMADA*. The Ceramic Society of Japan, The 30th Fall Meeting, Kobe, Japan. (September 19-21, 2017)

9. "Synthesis of Novel CoAl LDH-PANI Hybrid Films and Their High Supercapacitance Performance"
   Guoshen YANG, *Takahiro TAKEI, Sayaka YANAGIDA, Nobuhiro KUMADA*. The 56th Symposium on Ceramics, Tsukuba, Japan. (January 11-12, 2018)

10. "Controllable Synthesis of Novel CoAl LDH-PANI Nanosheets and Their Electrochemical Properties"
    Guoshen YANG, *Takahiro TAKEI, Sayaka YANAGIDA, Nobuhiro KUMADA*. The Ceramic Society of Japan, 2018 Annual Meeting, Sendai, Japan. (March 15-17, 2018)

11. "Electrochemical Properties of Transition Metal Hydroxide-Conductive Polymer Hybrid and Its Orientation in Magnetic Field"
    Guoshen YANG, *Takahiro TAKEI, Sayaka YANAGIDA, Nobuhiro KUMADA*. 7th Japan Association for Chemical Innovation/Green and Sustainable Chemistry (JACI/GSC) Symposium, Kobe, Japan. (June 14-15, 2018)

12. High-Performance Energy Storage Based on Hexagonal Tungsten Oxide-Polyaniline Hybrid Electrodes.
    Guoshen YANG, *Takahiro TAKEI, Sayaka YANAGIDA, Nobuhiro KUMADA*. 8th Japan Association for Chemical Innovation/Green and Sustainable Chemistry (JACI/GSC) Symposium, Tokyo, Japan. (June 24-25, 2019)

Acknowledgement

I would never have been able to complete my dissertation without the guidance of my advisor, help from group members and support from my family.

My deepest gratitude goes first and foremost to Professor Takahiro Takei, my advisor, for his constant encouragement and guidance. His extensive knowledge, insightful vision and creative thinking inspired me to pursue not only my Ph.D. but also a future career in scientific research. He has walked me through all the stages of the writing of this thesis. Without his consistent and illuminating instruction, this thesis could not have reached its present form.

Secondly, I would like to present my greatly appreciate to Prof. Kumada Nobuhiro for his valuable suggestions, enlightening ideas, considerate care and help in all aspects of my research and daily life. I am also very thankful to assistant Prof. Sayaka Yanagida for her valuable discussion, constructive suggestions and timely help. I want to present my gratitude to all the teachers in Crystal Center Science and Technology.

I would like to sincerely thank Prof. Tohru Suzuki and Prof. Tetsuo Uchikoshi, the director of Fine Particle Processing Group, National Institute for Materials Science (NIMS). I cherish and appreciate the internship opportunities provided by NIMS during my Ph.D. and the chance to meet and communicate with excellent researchers from different fields.

I also own my gratitude to all my friends at the University of Yamanashi, especially those in the Center for Crystal Science and Technology. Their accompany and friendship make my life less stressful and full of happiness during my doctoral studies.

Finally, I would like to acknowledge my parents, my sister and brother for their love, encouragements and understanding throughout my doctoral studies.